UNIVERSITY OF OKLAHOMA
GRADUATE COLLEGE

SEDIMENTOLOGY, CHEMOFACIES, AND STRATIGRAPHIC ARCHITECTURE OF THE LOWER CRETACEOUS BURRO CANYON FORMATION, NINEMILE HILL, UNAWEEP CANYON, COLORADO

A THESIS
SUBMITTED TO THE GRADUATE FACULTY
in partial fulfillment of the requirements for the
Degree of
MASTER OF SCIENCE

By
HANNAH MORGAN
Norman, Oklahoma
2021

SEDIMENTOLOGY, CHEMOFACIES, AND STRATIGRAPHIC ARCHITECTURE OF THE LOWER CRETACEOUS BURRO CANYON FORMATION, NINEMILE HILL, UNAWEEP CANYON, COLORADO

A THESIS APPROVED FOR THE

SCHOOL OF GEOSCIENCES

BY THE COMMITTEE CONSISTING OF

Dr. Matthew Pranter, Chair

Dr. R. Douglas Elmore

Dr. Rex Cole

ACKNOWLEDGEMENTS

This research was primarily funded through the Reservoir Characterization and Modeling Laboratory (RCML) at the University of Oklahoma (OU). In addition, the project was funded by the AAPG Foundation Grants-in-Aid Program through the James E. Hook Memorial Grant. I would like to recognize Spectrum Petrographics, Inc. for the thin sections used in my research. I would also like to recognize The EasyCopy Company for the software, EasyCore, used to construct the stratigraphic column.

I would like to thank Eric Eckberg and the Bureau of Land Management for allowing me to conduct research at Ninemile Hill. I would like to acknowledge Dr. Matthew Pranter for his patience, constant guidance, and support throughout my master's program. I would also like to thank Dr. Rex Cole for his assistance in the field and technical guidance on the sedimentology and stratigraphy of the Burro Canyon Formation. I would like to thank Dr. R. Douglas Elmore for his advice and assistance with the petrography and sedimentology of the project. I would like to thank Annette Moran for her constant support throughout my master's program. I would like to posthumously acknowledge Dr. Roger Slatt for help in the acquisition of XRF data. I would like to thank the Integrated Core Characterization Center (IC^3) laboratory at OU, specifically Micaela Langevin, Gary Stowe, Dr. Chandra Rai, and Dr. Carl Sondergeld, for lab access to measure the porosity and permeability of my samples. I would like to thank Dr. Andrew Elwood Madden, Brandon Maples, and Cansu Demirel-Floyd for assistance with the XRD lab and the clay fraction process. I would like to thank Dr. Michael Soreghan for giving insight into the specific limestone units within the Burro Canyon Formation at Ninemile Hill. I would also like to thank Dr. Anton Wroblewski for help identifying the ichnofossils present in outcrop.

I would like to thank Laura Ortiz Sanguino for her help in the field as my field assistant. I would like to thank Javier Tellez Rodriguez for his support and consistent guidance on the Burro Canyon Formation throughout the years. I would like to thank Kelsey Call (Lewis) for giving insight into the Burro Canyon Formation. I would like to thank Laynie Hardisty and David Duarte for guidance on chemofacies clustering using XRF data. I would like to thank both Abidin Berk Caf and David Duarte for help regarding general Python usage and code. I would like to thank Matt Hamilton for assistance in making core plugs. I would like to thank Chelsey Gallagher, Delcio Teixeira, and Cansu Demirel-Floyd for the Zoom study sessions and support in the last couple months. Finally, I would like to thank my friends and fellow RCML students, especially Hope Williams, for their support throughout the years.

TABLE OF CONTENTS

LIST OF TABLES

LIST OF FIGURES

ABSTRACT

Well-exposed outcrops of the Lower Cretaceous Burro Canyon Formation at Ninemile Hill and surrounding areas in western Colorado, provide insight into the depositional characteristics and stratigraphic variability of these fluvial deposits. Comparison of the fluvial heterogeneity to other outcrop studies of the Burro Canyon Formation further defines the spatial and lateral heterogeneity of the fluvial deposits. The sedimentology, chemofacies, and stratigraphic architecture are addressed through a detailed 73-ft (22.3-m) measured section with gamma-ray and x-ray fluorescence profiles and thin-section petrography. Burro Canyon Formation lithofacies consist of ripple-bedded fine-grained sandstone, green mudrock, cross-stratified and planar-bedded medium- to coarse-grained sandstone, slightly conglomeritic cross-stratified medium- to coarse-grained sandstone, and massive-bedded sandstone. Dominant indicator elements (lithologic and depositional environment proxies) are grouped into chemofacies using k-means and hierarchical clustering, identifying carbonate-rich facies, clay-rich facies, and sand-rich facies in outcrop. Genetically related lithofacies define architectural elements that stack to form an amalgamated channel complex that is overlain by a non-amalgamated channel complex. The lower interval is characterized by low-sinuosity to braided, higher net-to-gross ratio fluvial deposits and the upper interval consists of lower net-to-gross ratio floodplain deposits. Lower Burro Canyon deposition was by low-sinuosity to braided-fluvial systems within incised valleys, whereas the upper Burro Canyon was deposited within a floodplain-dominated environment.

INTRODUCTION

The Lower Cretaceous Burro Canyon Formation consists of braided-fluvial deposits and is considered a tight gas reservoir of the Piceance Basin in western Colorado. Fluvial deposits are heterogeneous at different scales— from the bedding and lithofacies scale to the architectural element scale (Clark, 2018; Clark, et al. 2018). The fluvial heterogeneity of the Burro Canyon Formation ultimately affects reservoir heterogeneity and thus plays an important role in influencing reservoir performance and productivity (Lewis et al., 2018; Lewis, 2018; Clark, 2018; Clark et al., 2018). Previous studies have focused on the lithofacies heterogeneity in outcrop and associated fluid flow (Lewis et al., 2018; Lewis, 2018; Clark, 2018; Clark et al., 2018). Outcrop studies of fluvial systems offer high-level detail about the vertical stacking of lithofacies and their reservoir characteristics. The purpose of this study is to characterize the stratigraphic variability of lithofacies, chemofacies (facies based on elemental abundances), and reservoir properties of the fluvial deposits of the Burro Canyon Formation in outcrop in Unaweep Canyon, Colorado as an analog for subsurface fluvial reservoirs.

In the 1940s, studies mainly focused on the Cedar Mountain Formation, the lateral equivalent of the Burro Canyon Formation. Stokes (1944) first described the Cedar Mountain Formation near Green River, Utah. Later, the Burro Canyon Formation nomenclature was attributed to the equivalent sequence in southwestern Colorado, separated from the Cedar Mountain Formation by the Colorado River (Stokes and Phoenix, 1948). In the early 1960s, Young analyzed the Dakota Group and the Cedar Mountain Formation on the Colorado Plateau and interpreted the environment of deposition to be mainly terrestrial deposits (Young, 1960). In the 1970s, Young correlated the basal Cretaceous strata of Utah into Colorado, resulting in the first detailed work on the sedimentology and stratigraphy of these units in the region (Young, 1970). Young (1970) then redefined the depositional environment of the Cedar Mountain Formation to include floodplain deposits. In a more detailed lithological analysis, Young (1973) described the lithofacies of the Cedar Mountain Formation to consist of conglomerate, conglomeratic braided-channel sandstones, and green to gray mudrock. Each sandstone body was described as widely traceable, massive, and consisting of innumerable small lens-like bodies (Young, 1973). By 1975, a better picture of the environment of deposition formed as Young postulated that the lowermost basal sandstones were deposited within paleovalleys that thinned along old interfluves of the Jurassic Morrison Formation (Young, 1975).

By the mid-70s, the lower Burro Canyon Formation was considered a possible petroleum reservoir; however, the Lower Cretaceous strata of the Piceance, Uinta, and Sand Wash basins continued to produce only minor accumulations of oil and gas (Young, 1975). Young (1975) suggested that the low yield was because of the terrestrial nature of the facies.

Since Young's studies on the Lower Cretaceous strata in the 70s, most of the detailed work published on the sedimentology, stratigraphy, and depositional environment focused on the lateral equivalent of the Burro Canyon Formation, the Cedar Mountain Formation. More recent studies of the Burro Canyon Formation have addressed, in detail, the sedimentological characteristics and stratigraphic variability of the Burro Canyon Formation in outcrop (Cole, 2014; Tellez et al., 2017, 2018a, 2018b, 2019a, 2019b, 2020, Clark, 2018; Clark, et al., 2018; Lewis et al., 2018; Lewis, 2018). These studies were conducted on a series of well-exposed outcrops along the Uncompahgre Uplift and Gunnison River Canyon from northwest of Grand Junction, Colorado to near Delta, Colorado (Figure 1). Cole (2014) laid the foundation of the more-recent studies by defining the lithofacies variations, interpreting the depositional settings and trends, correlating sequence boundaries, and characterizing the sandstone bodies from a reservoir perspective in several outcrops of the Burro Canyon Formation along a 60-mi (96.6-km) transect from the Utah-Colorado border to near Delta, CO. Tellez et al. (2020) defined the sedimentology, fluvial architecture, and sequence stratigraphy of outcrops along the Colorado and Gunnison River. Lewis et al. (2018), Lewis (2018), Clark (2018), and Clark et al. (2018) defined the key lithofacies and stratigraphic architecture (lateral continuity and stacking patterns of the lithofacies) of the Rattlesnake and Escalante Canyon outcrops and created 3-D outcrop models to assess how fluvial heterogeneity controls reservoir performance, static connectivity, and fluid flow (Figure 1).

To expand upon previous research, this study focuses on the sedimentology and stratigraphy of the Burro Canyon Formation in outcrops and roadcuts at Ninemile Hill at the northeastern end of Unaweep Canyon. This study explores the lateral variability of the Burro Canyon Formation and defines the stratigraphic heterogeneity of the fluvial deposits at Ninemile Hill.

This study addresses the following research questions:

1) What is the stratigraphic variability of chemical elements, mineralogy, lithology, lithofacies, chemofacies, and architectural elements?

2) What is the stratigraphic architecture?

3) What does the stratigraphic variability of sedimentary structures and lithofacies suggest regarding paleoflow direction?

4) How does the stratigraphy relate to other Burro Canyon outcrops?

The Lower Cretaceous Burro Canyon Formation in the southwestern Piceance Basin was investigated using outcrop data acquired along the Uncompahgre Uplift in Unaweep Canyon in Mesa County near Grand Junction, Colorado (Figure 1). The outcrop is located on Ninemile Hill along 31 4/10 Rd on a portion of Colorado Highway 141 in Unaweep Canyon (Figure 2). A 73-ft (22.3-m) thick stratigraphic interval of the Burro Canyon Formation was examined using conventional sedimentologic field methods coupled with laboratory analysis to investigate the stratigraphic variability of the mineralogy, chemical elements, and lithology. The field data acquired include paleocurrent measurements, an outcrop gamma-ray log, sedimentological and lithological descriptions, hand samples, and drone imagery. Other types of data include thin-section petrography, porosity and permeability measurements, x-ray fluorescence (XRF), and x-ray diffraction (XRD).

The data from Ninemile Hill were used to build upon previous outcrop-to-subsurface studies to interpret the lateral variability of depositional and reservoir characteristics of the Burro Canyon Formation (Cole, 2014; Lewis et al., 2018; Lewis, 2018; Clark, 2018; Clark et al., 2018; Tellez et al., 2020). Results from this study are useful to better understand Burro Canyon Formation fluvial deposits as subsurface reservoirs and to address the sedimentological and stratigraphic controls on reservoir heterogeneity of similar fluvial reservoirs.

GEOLOGIC SETTING

The Piceance Basin is a highly asymmetrical, northwest-southeast trending basin located in northwestern Colorado (Tweto, 1975; Johnson, 1989). The basin is a Laramide feature that began forming during the Late Cretaceous and was later partitioned in the Eocene (Johnson and Flores, 2003; DeCelles, 2004). It is separated from the Uinta Basin by the Douglas Creek arch and is bounded by the Uncompahgre Uplift to the southwest, the Gunnison Uplift to the south, the Sawatch Uplift to the southeast, the White River Uplift to the east, and the Axial Arch to the north (Johnson, 1989). The Uncompahgre Uplift is a northwest-trending Laramide structure

FIGURE 1: AREA OF STUDY

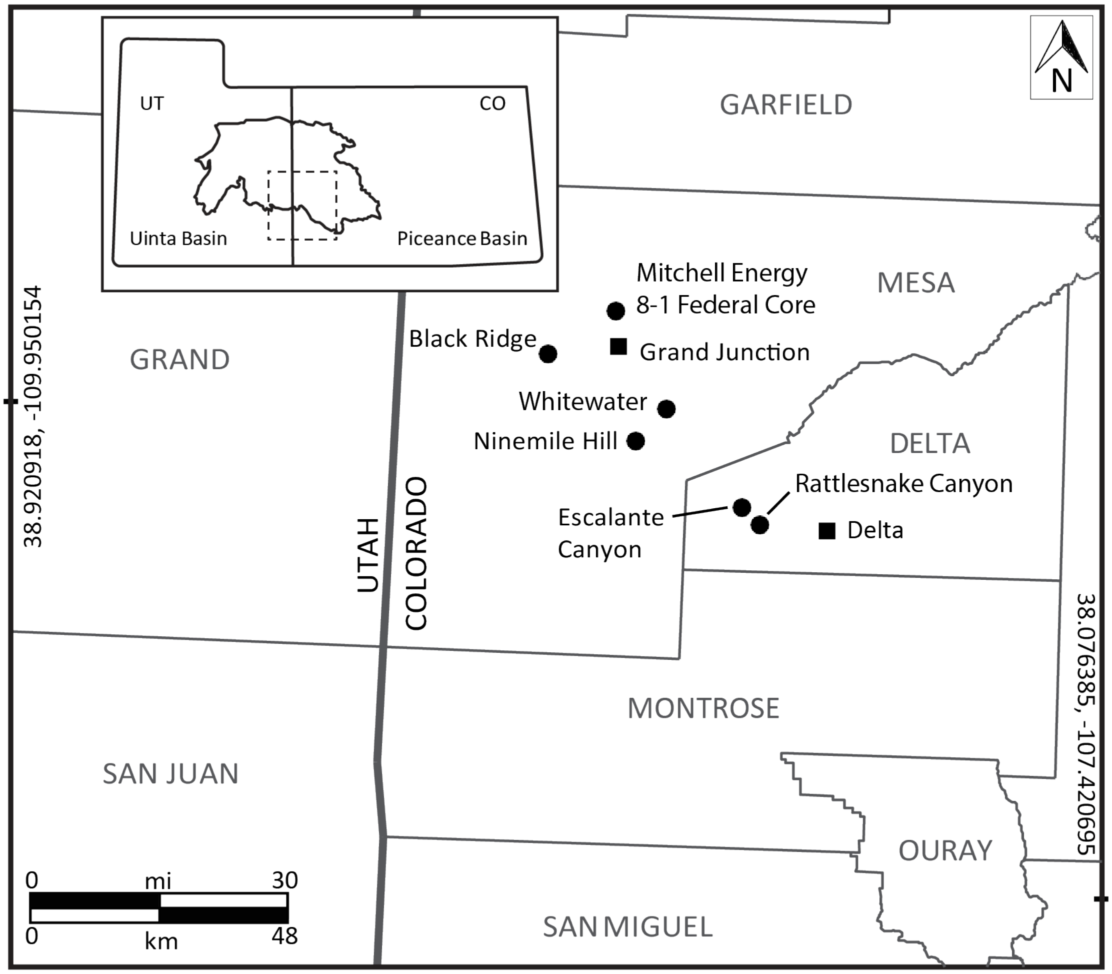

Figure 1. Location map of eastern Utah and western Colorado with inset map of the Uinta and Piceance basins. The study area, Ninemile Hill, is located in Mesa County, Colorado. Other nearby outcrop locations, including the Mitchell Energy 8-1 core location, is shown. Modified from Clark (2018).

FIGURE 2: OUTCROP LOCATION

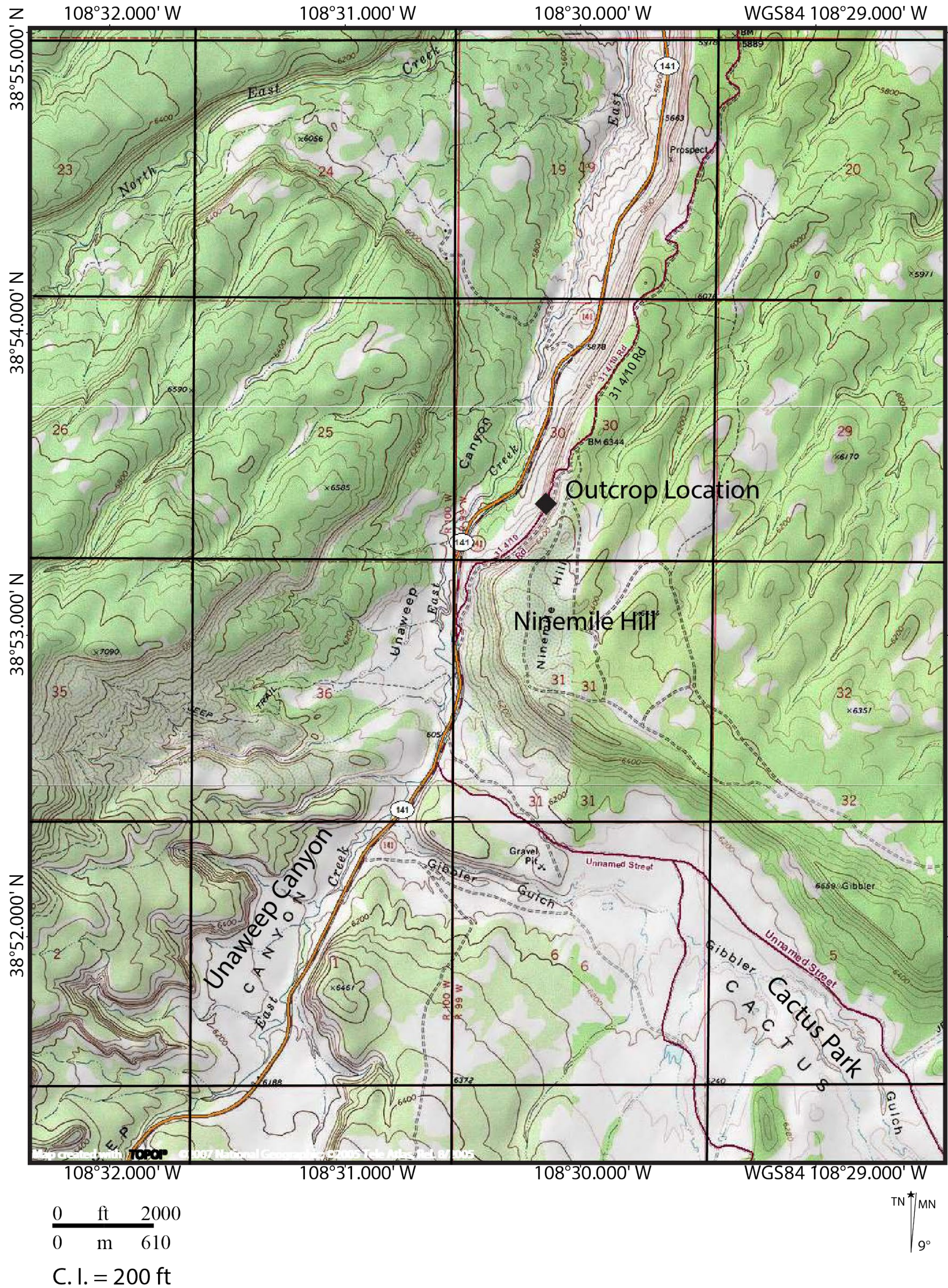

Figure 2. Topographic map of Ninemile Hill showing the general study area and outcrop location. Outcrop location is shown by the black diamond. Measured section was taken along the east side of Unaweep Canyon along 31 4/10 Road located off Colorado Highway 141.

adjacent to the Piceance Basin that is bounded by faulted monoclines to the southwest and northeast (Case, 1991; Williams, 1964; Cashion, 1973).

The Uncompahgre Uplift and Piceance Basin reside in an area that was once originally part of the greater Rocky Mountain Foreland Basin system. The foreland basin was formed by the Sevier Orogeny in present-day western Utah and flexural subsidence to the east in early Aptian time (Young, 1973; DeCelles et al., 1995). Subsequently, multiple pulses of clastic sediment eroded from the Sevier Orogenic belt were transported and deposited in an easterly direction towards the early Mancos Sea (Cretaceous Interior Seaway) as periodic subsidence ensued (Young, 1973). During early Albian time, the early Mancos Sea expanded, resulting in a marine transgression (Young, 1975).

Deposited in the Aptian-Albian ages of the Early Cretaceous, the Burro Canyon Formation unconformably overlies the Late Jurassic Morrison Formation and is unconformably overlain by the late Albian-Cenomanian Dakota Formation (Figure 3). Thus, it is bounded by the K-1 and K-2 unconformities at the base and top, respectively. The Cedar Mountain Formation in the Uinta Basin of Utah is the lateral equivalent of the Burro Canyon Formation in the Piceance Basin and along the Uncompahgre Uplift of Colorado. More specifically, the Ruby Ranch Member and the Poison Strip Sandstone are the probable equivalents (Figure 3) (Kirkland et al., 2007). The Burro Canyon Formation is characterized by fluvial, floodplain, and lacustrine deposits consisting of conglomerate, sandstone, mudrock, minor chert, and limestone (Figure 4) (Stokes and Phoenix, 1948, Craig, 1982). The lower section of the Burro Canyon typically consists of conglomerates and sandstones which were deposited in a northeast-easterly direction through low-sinuosity to braided-river systems within incised valleys leading from the Sevier Orogenic belt (Young, 1975). Although rare, minor carbonaceous deposits, chert, and thin

FIGURE 3: CHRONOSTRATIGRAPHY

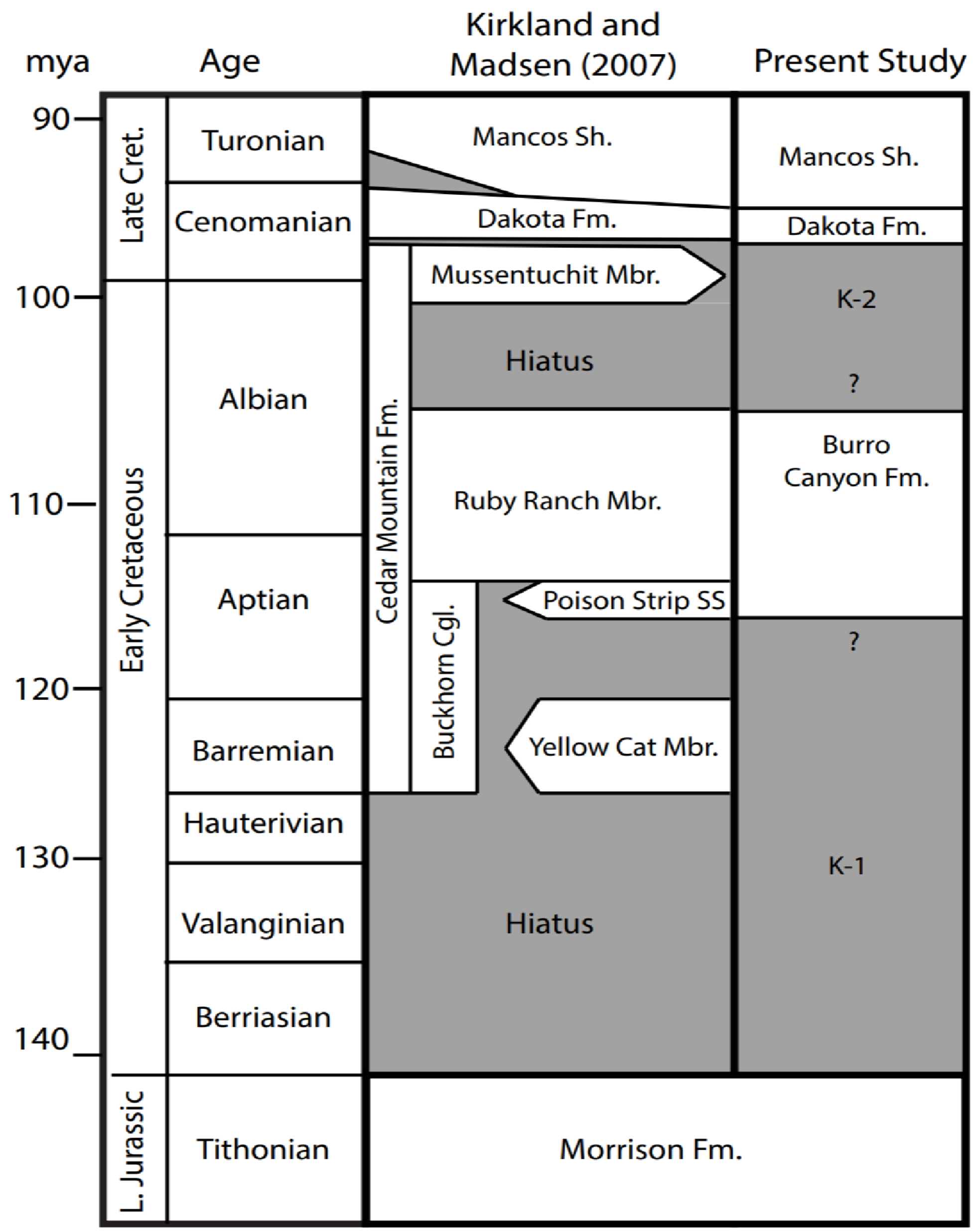

Figure 3. Late Jurassic to Late Cretaceous chronostratigraphy of the Uinta and Piceance basins. Stratigraphic nomenclature used in past studies has varied. In the present study area, the Burro Canyon Formation is bounded by the K-1 and K-2 unconformities and is Aptian-Albian in age. From Clark (2018) and Cole (2017, personal communication).

FIGURE 4: COMPOSITE SECTION

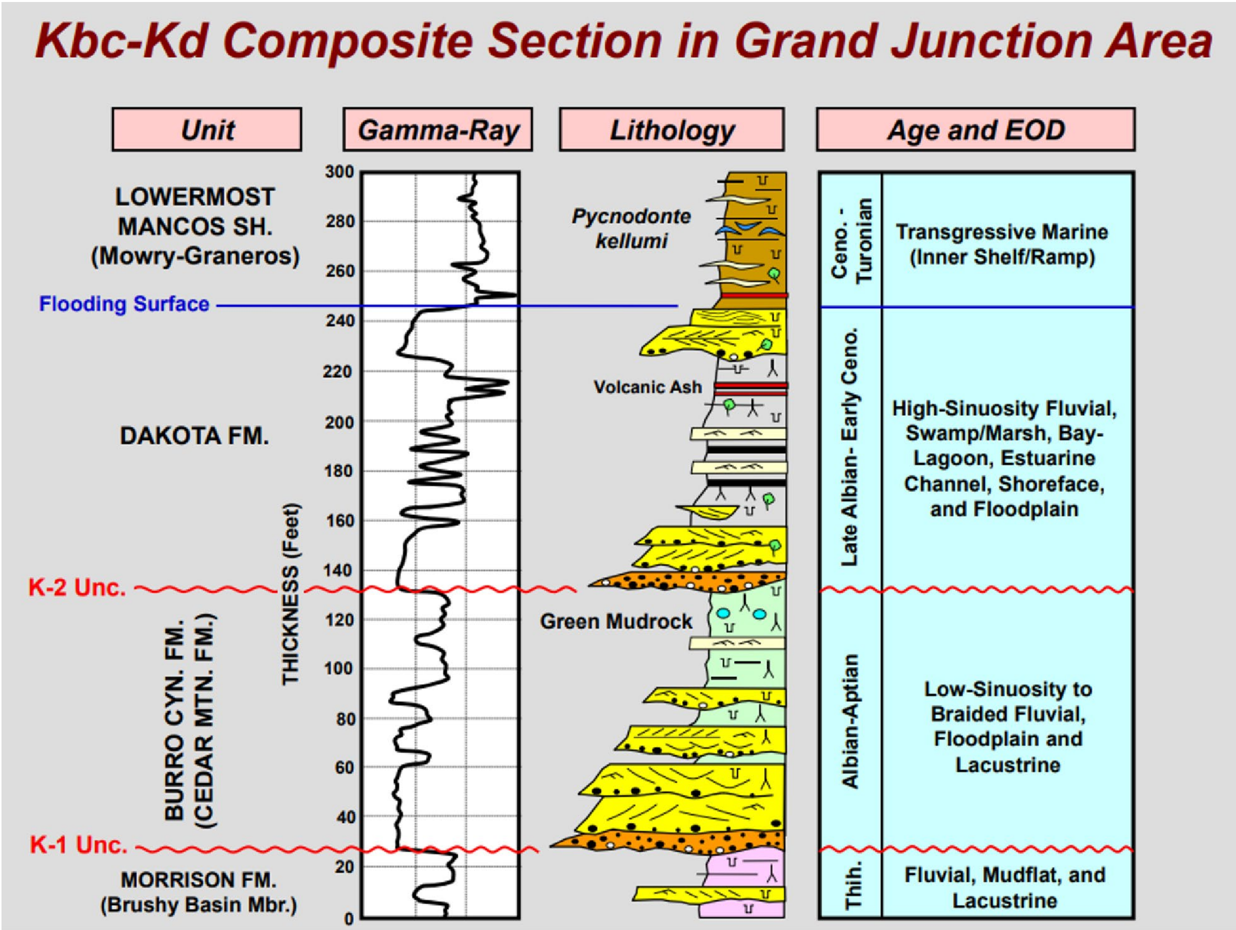

Figure 4. Composite section typical of the Burro Canyon (Kbc)-Dakota (Kd) interval in the Grand Junction area (personal communication from R. Cole, 2014).

limestone beds exist in the Burro Canyon Formation but are more prevalent in the Cedar Mountain Formation in the form of limestone lenses and nodules (Kirkland, et al., 1997; Young, 1973; Craig, 1982). The limestones and cherts are generally restricted to the upper part of the Burro Canyon Formation and are localized deposits (Craig, 1982). The upper interval of the Burro Canyon Formation mainly consists of greenish, calcareous mudrock and finer-grained sandstone which is indicative of a shift from a dominantly braided-fluvial river system to a low-sinuosity fluvial system with floodplain and lacustrine depositional settings (Young, 1960; Cole, 2014). Therefore, two distinct channel complexes are typical of the Burro Canyon Formation: a lower interval characterized by a low-sinuosity, higher net-to-gross, amalgamated braided-fluvial system and an upper interval characterized by a lower net-to-gross, non- to semi-amalgamated braided- to sinuous-fluvial system with associated floodplain and lacustrine deposits. The Burro Canyon Formation is therefore interpreted as consisting of low-sinuosity to braided-fluvial, lacustrine, and floodplain deposits.

METHODS

Conventional Field Methods

To document the sedimentology and stratigraphic variability of the Burro Canyon Formation, a detailed stratigraphic section was measured at the Ninemile Hill location along the east side of 31 4/10 Road off Colorado State Highway 141 in Unaweep Canyon (Figure 2). The section follows a series of relatively fresh and nonweathered roadcuts, which involved some recent blasting. The measured section is 73-ft (22.3-m) thick and bounded unconformably by the Jurassic Morrison Formation at the base and the Cretaceous Dakota Formation at the top. The measured section includes descriptions of lithology, grain size, sedimentary structures, bedding characteristics, such as scour surfaces, and a collection of paleocurrent data. Paleocurrent measurements (N=45) were acquired from cross-stratification using a Brunton compass. Outcrop gamma-ray measurements were acquired and correlated to the lithologic units of the stratigraphic section. The gamma-ray values were acquired at a 1-ft (0.31-m) sample increment using a Super-Spec RS-125 scintillometer (Radiation Solutions, Inc.). Outcrop samples (N=73) were acquired for laboratory analysis at different sampling distances depending on the purpose of the sample (e.g., thin-section petrography, x-ray fluorescence analysis) and the accessibility of sampling due to the steep face of the outcrop. Samples (N=73) were acquired at a one-ft (0.31-m) sample increment for X-ray fluorescence (XRF) analysis and at a 5-ft (1.5-m) sample increment for both petrophysical and thin-section analyses. One-inch-diameter core plugs (N=16) were acquired in the laboratory at an approximately 5-ft (1.5-m) sample increment from outcrop samples taken from the field using a Model G0755 Heavy-Duty Drill (Grizzly Industrial). To address the lateral variability of the fluvial deposits, stratigraphic cross-sections were made through Black Ridge, Ninemile Hill, Whitewater, Escalante Canyon, and Rattlesnake Canyon using previous work from Cole (2014), Lewis et al. (2018), Lewis (2018), Clark (2018), and Clark et al. (2018).

X-ray Powder Diffraction (XRD)

The green mudrock section of the upper Burro Canyon Formation (Figure 4), was analyzed using x-ray powder diffraction (XRD) at the Powder XRD Laboratory at the University of Oklahoma to identify the clay composition of six samples. Five samples were acquired from the Burro Canyon Formation at the Ninemile Hill location, and one sample was acquired from the Escalante Canyon location to investigate the variability of the clay content. Six oriented mounts were prepared and analyzed using the filter-peel method and clay separation with rapid dismembration. First, the samples were gently disaggregated and crushed using a percussion mortar. The samples were then mixed with deionized water, disaggregated using the sonic dismembrator, and centrifuged. The supernatant was then decanted and mounted on standard glass holders using the filter-peel method. The oriented mounts underwent three XRD analyses. The samples were analyzed with 0.02° step size and two second count time using fixed slits (Demirel et al., 2018). After the first analysis on the air-dried mounts, the samples underwent ethylene glycol treatment. After the second analysis, the samples underwent heat treatment at 550°C (1022°F). The mineralogy was determined using a Rigaku Ultima IV diffractometer with a Cu radiation source, a graphite monochromator, and the Bragg-Brentano method (2-70° 2Θ angle interval) (Demirel et al., 2018). The mineral composition was then determined using MDI Jade software and the Reitveld refinement method (Bish and Howard, 1988; Demirel et al., 2018). The mineral identification was based on the position (2Θ), d-spacing (Å), and intensities of the peaks (counts).

Chemofacies Analysis

To determine the chemofacies of the outcrop, elemental data using x-ray fluorescence (XRF) methods were obtained from the samples (N=73) acquired at a 1-ft (0.31-m) sample increment using a handheld Bruker Tracer IV-SDTM XRF spectrometer. Data were obtained for major elements at 15kV, 35 mA for 90 seconds and for trace elements at 40 kV, 17.1 mA for 60 seconds. The XRF raw spectral data were converted to parts per million (ppm) using a calibration standard from Rowe et al. (2012). From the 30 element concentrations obtained, six elements were used for interpretation and chemofacies classification due to their significance as proxies for lithology and depositional environments: silicon (Si), titanium (Ti), zirconium (Zr), aluminum (Al), potassium (K), and calcium (Ca). The elemental data (ppm) were clustered into chemofacies (facies determined by elemental abundances) using unsupervised machine-learning techniques and Python (programming language). Two clustering methods were tested to determine a suitable technique for chemofacies classification (k-means and hierarchical clustering). The chemofacies were clustered using known the six elemental proxies: Si, Al, K, Ti, Zr, and Ca and were related to outcrop-defined lithology (Pearce and Jarvis, 1992).

For chemofacies clustering, a min-max scaler was applied to the XRF data to ensure the data were appropriately scaled. The optimal number of clusters was determined using an elbow plot of the sum of squares within (SSW) the clusters. The XRF data were clustered into chemofacies using both k-means and hierarchical clustering. The chemofacies clusters were plotted with depth, a simplified lithology log, and the elemental data (in ppm) of Si, Al, K, Ti, Zr, and Ca to investigate their relationships and stratigraphic variability. The relationship between chemofacies, porosity, and permeability was analyzed by cross-plotting porosity and permeability and color-coding the datapoints to chemofacies clusters.

Porosity and Permeability

Porosity and permeability were measured at the Integrated Core Characterization Laboratory (IC^3) at the University of Oklahoma from fifteen core plug samples that were acquired at a 5-ft (1.5-m) sample increment. The core plugs were cut using a PICO155 Precision Cutter (Pace Technologies) and polished using a METPREP3 PH-3 Grinding/Polishing System (Allied High Tech Products, Inc.). The bulk volume of the sample was calculated using the standard equation for the volume of a cylinder based on plug height and diameter measurements. Porosity and permeability were measured using an AP-608 Automated Permeameter and Porosimeter (Core Test Systems, Inc.). The AP-608 uses the concepts of Boyle's Law to measure the porosity and permeability of each sample. Several pressure values (800 psi, 1500 psi, 3000 psi) were used to measure porosity and permeability constrained by the values determined by previous work on the Mitchell Energy 8-1 Federal core from Mesa County, Colorado (Figure 1) (Lewis, 2018; Clark, 2018). The stratigraphic variability of the porosity and permeability was analyzed and related to qualitative changes in lithofacies, sorting, grain size, cements, and pore types to investigate the controls on reservoir quality.

Thin-Section Petrography

Fifteen thin sections were created from sandstone and limestone samples acquired at a 5-ft (1.5-m) sample increment and analyzed to further define and constrain the mineralogy, texture, and fabric of the formation. Petrographic examination involved a qualitative visual assessment and some semi-quantitative interpretations (direct grain measurements). Framework-grain composition, size, rounding, and sorting were identified along with cements, textural fabrics, and pore types. The framework-grain composition was determined by petrographic examination. Folk's classification method was used to classify the sandstone samples. These data were then compared to the lithologic description acquired in the field to further modify the stratigraphic column. Average grain size was measured from thin-section examination to determine texture. The framework-grains, sorting, and cements were compared to the porosity and permeability measurements of the corresponding hand samples to qualitatively assess the pore types.

Drone-based Photogrammetry and Stratigraphic Architecture

To determine the local stratigraphic architecture of the Burro Canyon Formation, genetically related lithofacies were grouped into architectural elements using the detailed measured section data and drone imagery. High-resolution outcrop images of the approximately 865-ft (263.7-m) long west-facing exposure were captured using a DJI Phantom 4 drone (small Unmanned Aerial System – sUAS). Drone imagery was used to correlate key stratigraphic surfaces, characterize architectural elements, and evaluate how the deposits vary both laterally and stratigraphically. Stratigraphic architecture (e.g., non-amalgamated to amalgamated channel complexes) was defined from the stacking patterns of the architectural elements using the hierarchical framework established by Patterson et al. (1995, 2010) and Sprague et al. (2002). Within this framework, fluvial stratigraphic elements are hierarchically ordered from the individual bed-scale to composite sequences. The stratigraphic architecture of the outcrop at Ninemile Hill was then compared to other nearby locations (i.e., Rattlesnake and Escalante Canyons) to further interpret the regional context of the depositional environment of the Burro Canyon Formation at Ninemile Hill (Clark, 2018; Lewis, 2018).

RESULTS

Sedimentology

Burro Canyon lithologies at Ninemile Hill consist of 1) sandstone 2) mudrock and 3) limestone (Figure 5). The dominant primary and secondary sediment structures and bedding characteristics consist of planar-bedding, planar-lamination, wavy- and ripple-bedding, wavy-lamination, bioturbation (burrows that have been infilled with sand within mud clasts that have been eroded), graded bedding, cross-stratification (both tabular-tangential and inclined), cross-lamination, massive-bedding, and scour surfaces (channel scour) (Figure 6, Figure 7). Bedding contacts are either defined by basal scour surfaces or planar contacts. The grain size of the sandstone lithologies range from fine- to coarse- grained. The net-to-gross sandstone ratio of the outcrop is approximately 77% based off the proportions of sandstone to non-sandstone lithologies defined in outcrop.

FIGURE 5: MEASURED SECTION

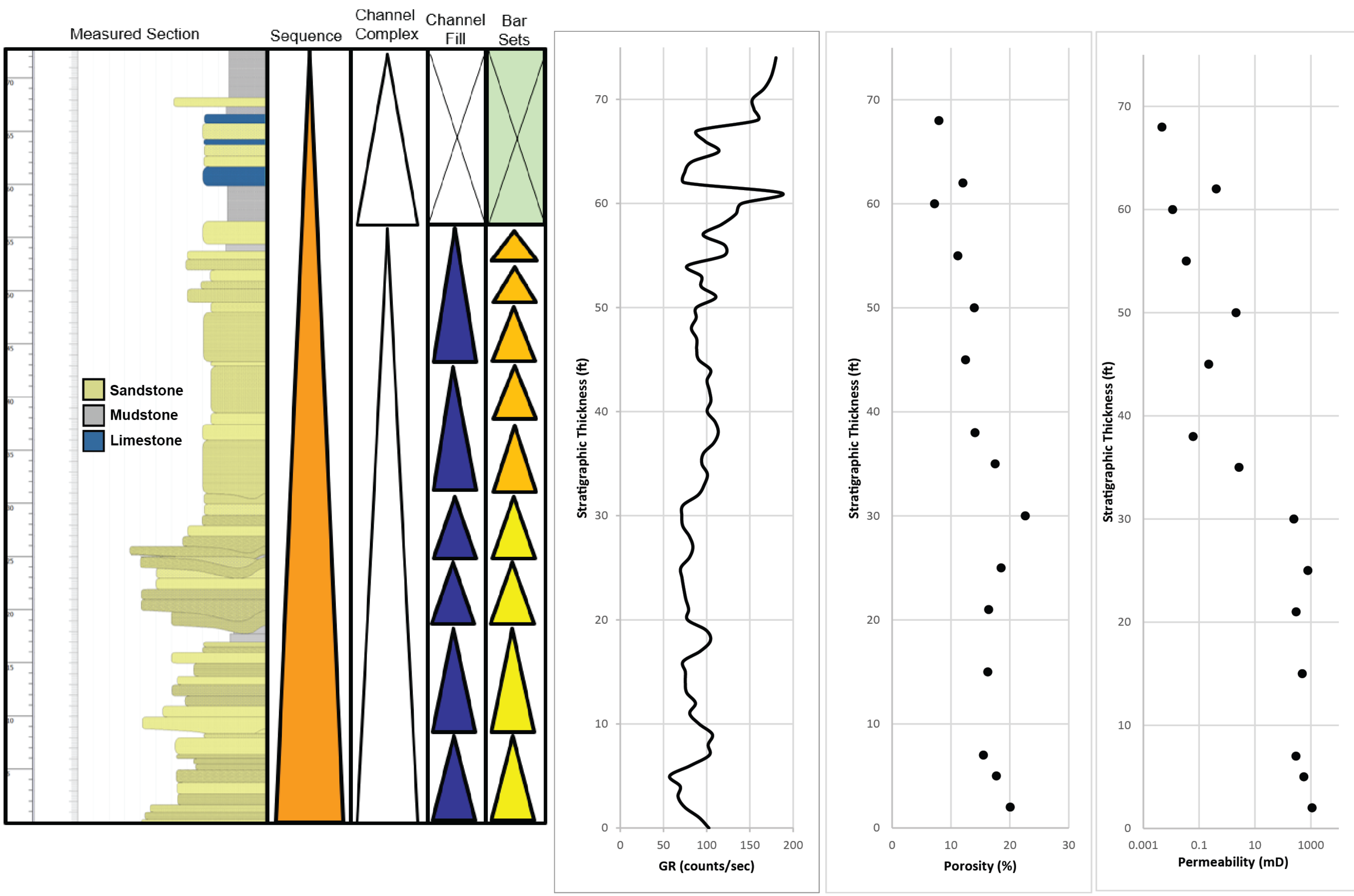

Figure 5. Measured section (left) shows a higher net-to-gross interval at the base of the section that is characterized by cross-stratified, massive-bedded, coarse-grained sandstones with channel scour features. The uppermost section consists of a lower net-to-gross section characterized by mudrock, limestone, and planar- and wavy-bedded fine-grained sandstones. Architectural elements, outcrop gamma ray, porosity, and permeability are shown on the right. Porosity and permeability were measured in approximately 5-ft (1.5-m) increments. Porosity and permeability decrease up-section.

FIGURE 6: SEDIMENTARY STRUCTURES

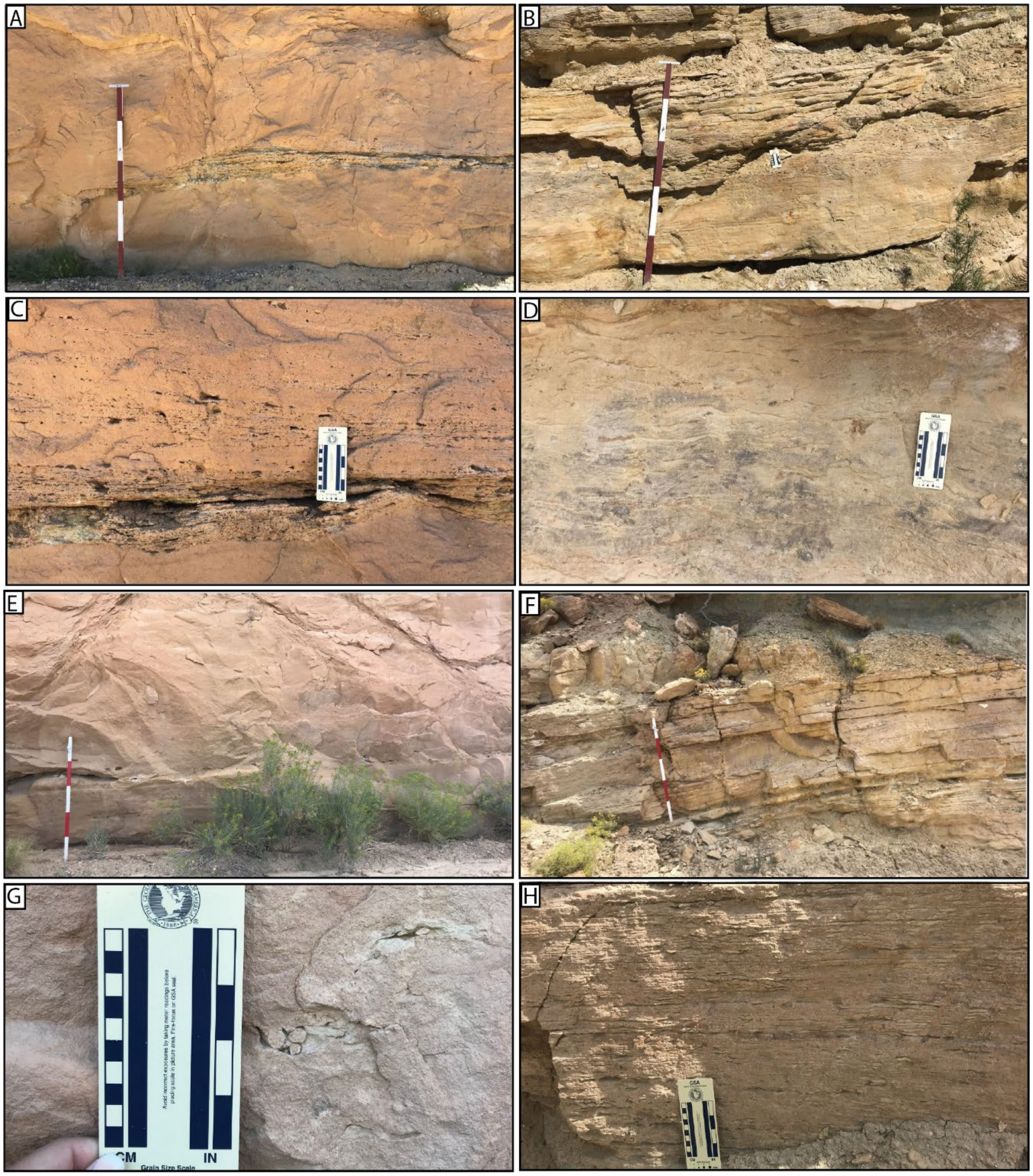

Figure 6. Other sediment structures and characteristics of the Burro Canyon Formation at Ninemile Hill. Basal channel scour is common (A). Wavy-bedding (B) and wavy-laminations (D) exist in the upper Burro Canyon. Planar-bedding (F) and planar-laminations (H) exist throughout both the upper and lower Burro Canyon. Massive-bedding also exists throughout the section but it is possible that the sedimentary structures are not yet visible due to the fresh outcrop face. Interbedded sand, mud lenses, and mud clasts are shown in (C). The mud clasts are commonly eroded out of the outcrop, sometimes exposing burrows infilled by sand (G).

FIGURE 7: CROSS-STRATIFICATION VARIABILITY

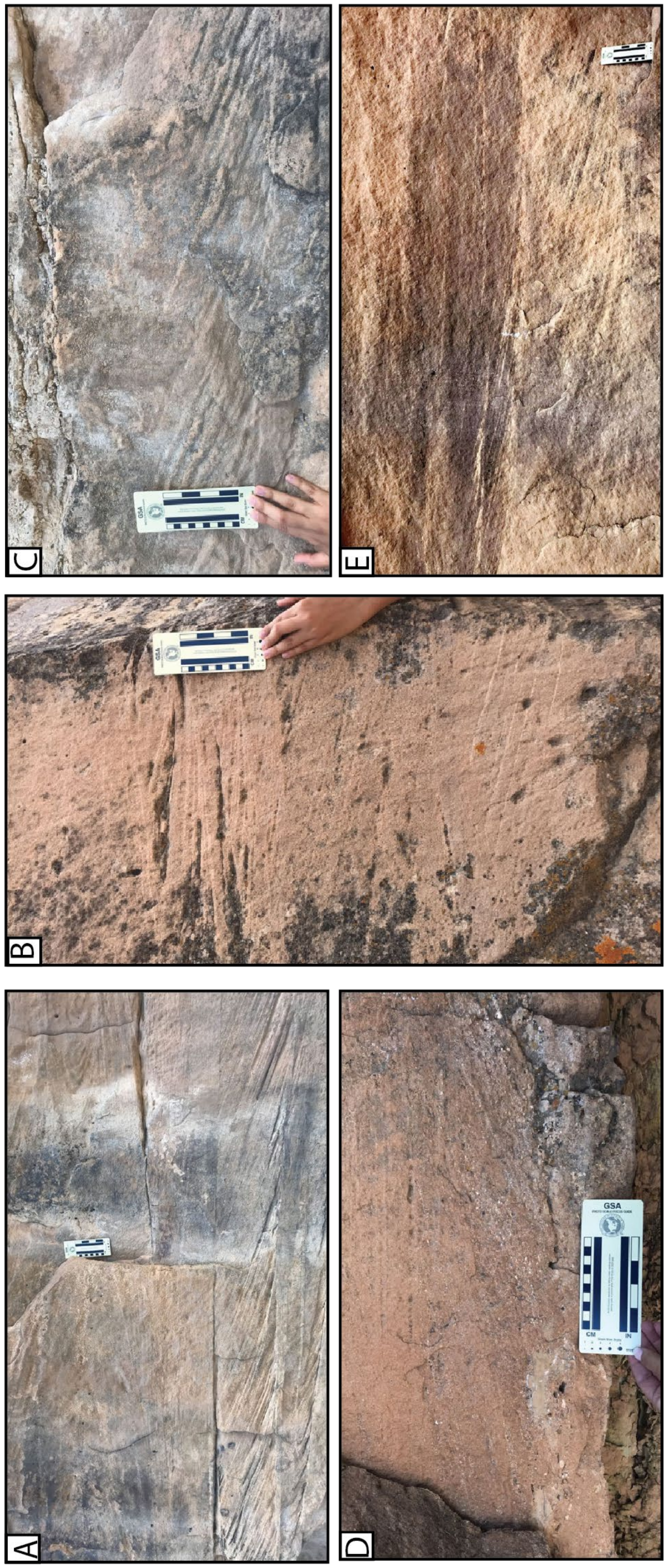

Figure 7. Different types of cross-stratification of the Burro Canyon Formation at Ninemile Hill in sandstones (A; B; C; E) and slightly conglomeratic sandstones (D). Cross-stratification ranges from tabular-tangential (A; base of B) to low-angle (top of B; C; D; E). Cross-stratified units are often stacked and topped by planar-bedded units (A; B; D). The cross-stratified conglomeratic sandstone beds are often graded with larger grains located along the bases of the cross-laminae and fining upward until the subsequent cross-laminae.

Thin-section petrography further defines the lithologic properties of the outcrop. The samples mostly consist of quartzarenites and sublitharenites. Sorting ranges from well- to poorly sorted. Rounding ranges from rounded to subangular. Dominant cements (more than 50%) include quartz and hematite. Minor cements (less than 50%) include calcite, clay, chert, and dedolomite. Thin-section results are summarized below and related to porosity and permeability data (Figure 8). The sample numbers are distance measurements (in ft, m) relative to the base of the measured section (e.g., BC-2 is at 2 ft [0.62 m] from the measured section base).

BC-2

BC-2 (2 ft; 0.62 m) is a coarse-grained, subrounded to rounded, moderately to poorly sorted sublitharenite (Figure 1; Appendix B). Framework grains are dominantly quartz with minor chert and feldspars. Cement types observed in thin section include quartz and minor hematite. Pore types are identified as mainly intergranular with the possibility of secondary porosity due to dissolved lithics and/or feldspars, although large void spaces could be plucked grains.

BC-5

BC-5 (5 ft; 1.52 m) is a medium-grained, subrounded to subangular, moderately sorted quartzarenite (Figure 1; Appendix B). Framework grains are dominantly quartz with minor chert. Cement types include quartz with minor dedolomite. Pore types are identified as mainly intergranular with the possibility of secondary porosity due to dissolved lithics and/or feldspars.

BC-7

BC-7 (7 ft; 2.1 m) is a medium-grained, subrounded to subangular, moderately to well sorted quartzarenite (Figure 1; Appendix B). Framework grains are dominantly quartz with minor chert. Cement types include quartz with minor hematite and dedolomite. Pore types are

FIGURE 8: THIN-SECTION SUMMARY

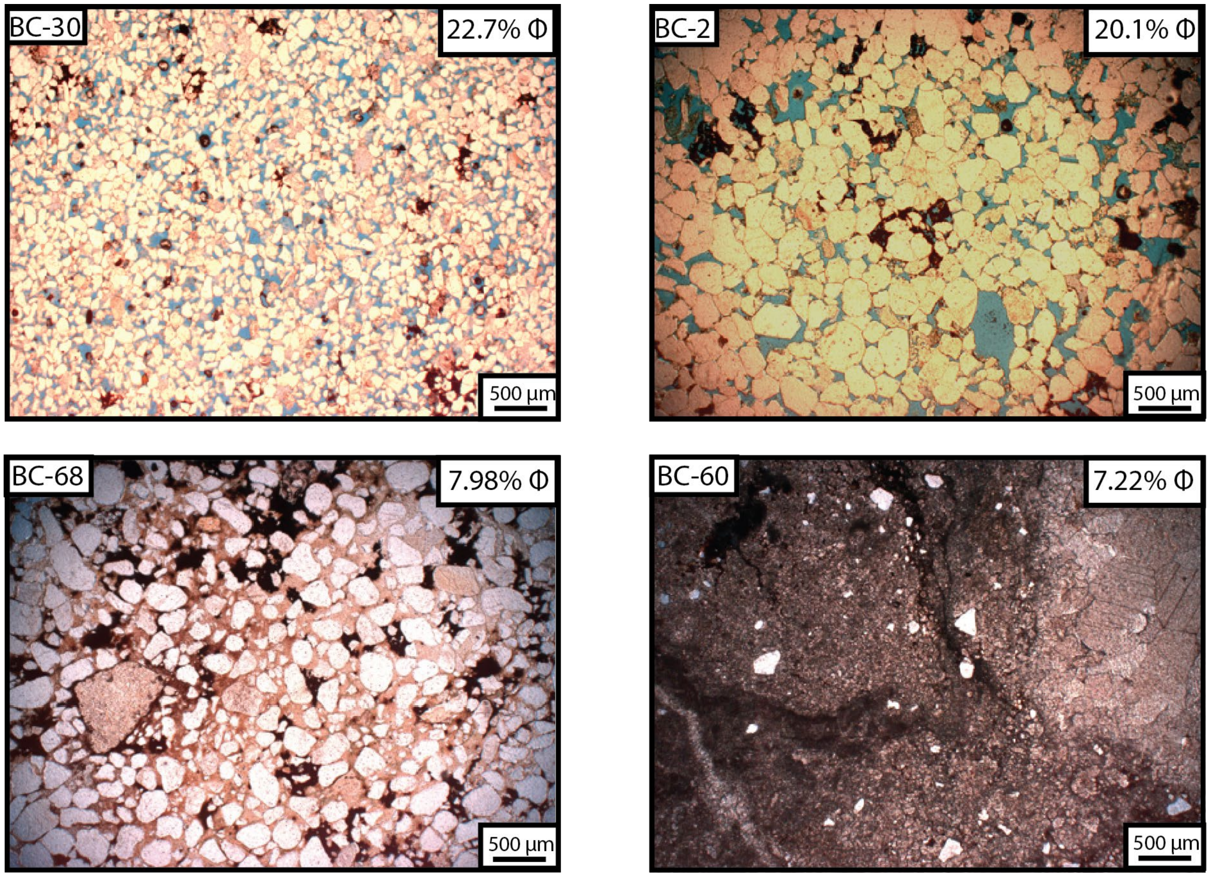

Figure 8. Thin-section photomicrographs (plane-polarized light) that provide examples of the variability of the sedimentology from the Burro Canyon samples at Ninemile Hill. BC-30, BC-2, and BC-68 are sandstones with a range of grain sizes, sorting, and cement types. Cement varies between chert, calcite, hematite, and quartz. BC-60 is a limestone. Porosity values are labeled for each.

identified as mainly intergranular with the possibility of secondary porosity due to dissolved lithics and/or feldspars.

BC-15

BC-15 (15 ft; 4.57 m) is a medium- to coarse-grained, subrounded to subangular, moderately sorted quartzarenite (Figure 1; Appendix B). Framework grains are dominantly quartz with minor chert. Cement types include quartz with minor hematite and dedolomite. Pore types are identified as mainly intergranular with the possibility of secondary porosity due to dissolved lithics and/or feldspars.

BC-21

BC-21 (21 ft; 6.4 m) is a coarse-grained, subrounded, moderately to poorly sorted quartzarenite (Figure 1; Appendix B). Framework grains are dominantly quartz with minor chert. Cement types include quartz with minor hematite and dedolomite. Pore types are identified as mainly intergranular with the possibility of secondary porosity due to dissolved lithics and/or feldspars.

BC-25

BC-25 (25 ft; 7.62 m) is a coarse-grained, subrounded, moderately to poorly sorted sublitharenite (Figure 1; Appendix B). Framework grains consist of quartz with minor chert and quartzite. Cement types include quartz with minor hematite and calcite. Pore types are identified as mainly intergranular with the possibility of secondary porosity due to dissolved lithics and/or feldspars.

BC-30

BC- 30 (30 ft; 9.14 m) is a fine- to medium-grained, subangular, well-sorted quartzarenite (Figure 1; Appendix B). Framework grains consists of quartz. Cement types include quartz with minor hematite. Pore types are identified as mainly intergranular with the possibility of secondary porosity due to dissolved lithics and/or feldspars.

BC-35

BC-35 (35 ft; 10.67 m) is a fine-grained, subangular, poorly sorted quartzarenite (Figure 1; Appendix B). Framework grains consist mostly of quartz. Cement types include quartz and hematite. Pore types are identified as mainly intergranular with the possibility of secondary porosity due to dissolved lithics and/or feldspars.

BC-38

BC-38 (38 ft; 11.58 m) is a fine to very fine-grained, subangular to subrounded, poorly sorted quartzarenite (Figure 1; Appendix B). Framework grains consist mostly of quartz. Cement type is dominantly hematite with minor quartz. Porosity is not visible in thin section.

BC-45

BC-45 (45 ft; 13.72 m) is a fine to very fine-grained, subangular, moderately sorted quartzarenite (Figure 1; Appendix B). Framework grains consist mostly of quartz. Cement types consist of quartz, hematite, and clay. Porosity is not visible in thin section.

BC-50

BC-50 (50 ft; 15.24 m) is a fine to very fine-grained, subrounded to subangular, moderately sorted quartzarenite (Figure 1; Appendix B). Framework grains consist mostly of quartz. Cement types consist of quartz, hematite, and calcite. Pore types are identified as mainly intergranular with the possibility of secondary porosity due to lithics and/or dissolved feldspars.

BC-55

BC-55 (55 ft; 16.76 m) is a fine to very-fine grained, subrounded to subangular, moderately sorted quartzarenite (Figure 1; Appendix B). Framework grains consist mostly of quartz. Cement types consist of quartz, hematite, and chert. Porosity is not visible in thin section.

BC-60

BC-60 (60 ft; 18.29 m) is classified as a dismicrite using Folk terminology that mostly consists of micrite, vein-like sparry calcite, with minor quartz clasts (Figure 1; Appendix B). Pore space is not visible in thin section.

BC-62

BC-62 (62 ft; 18.9 m) is a fine to very-fine grained, subrounded to subangular, moderately to poorly sorted quartzarenite (Figure 1; Appendix B). Framework grains are dominantly quartz with minor chert. Cement types consist of quartz, chert, and hematite. Porosity is not visible in thin section.

BC-68

BC-68 (68 ft; 20.73 m) is a medium-grained, subrounded to rounded, poorly sorted sublitharenite (Figure 1; Appendix B). Framework grains consist mostly of quartz with minor chert. Cement types consist of pervasive chert cement. Porosity is not visible in thin section.

Lithofacies

Burro Canyon lithofacies at Ninemile Hill consist of 1) conglomeratic sandstone 2) slightly conglomeratic sandstone 3) cross-stratified sandstone (trough and tabular-tangential) 4) wavy-bedded sandstone 5) planar-bedded sandstone 6) massive sandstone 7) limestone and 8) green mudrock (Table 1). Cross-stratified sandstone is the dominant facies in the lower Burro Canyon, while fine-grained sandstone and green mudrock are the dominant facies in the upper

TABLE 1: DOMINANT LITHOFACIES

Burro Canyon Lithofacies							
Lithofacies	Grain Size	Sorting	Stratification	Color	Cement Type	Clast Type	Depositional Environment
Conglomeratic to Slightly Conglomeratic Sandstone	Granule- Coarse	Poor- Moderate	Cross Bedded	Light Grey, Tan, with Brown Specks	Quartz, Minor Hematite, Calcite, Minor Dedolomite	Quartz, Chert	Channel Floor
Cross-Stratified Sandstone	Coarse-Fine	Poor- Moderate	Tabular Tangential and Trough	Light Grey, Tan, with Brown Specks	Quartz, Minor Hematite, Minor Dedolomite	Quartz, Chert	Channel & Compound Bars
Wavy-Bedded Sandstone	Very Fine-Fine	Moderate-Well	Wavy Bedded	Light Grey, Tan, with Brown Specks	Quartz, Minor Hematite, Calcite	Quartz	Channel & Compound Bars
Planar-Bedded Sandstone	Fine-Medium	Moderate-Well	Planar Bedded	Light Grey, Tan, with Brown Specks	Quartz, Minor Hematite, Calcite	Quartz	Channel & Compound Bars
Massive Sandsone	Fine-Medium	Moderate-Well	Structureless	Tan, White, with Brown Specks	Quartz, Chert, Clay, Minor Hematite, Calcite	Quartz	Channel & Compound Bars
Limestone	N/A	N/A	N/A	Grey, Light Tan	N/A	Minor Quartz	Floodplain and Lacustrine
Green Fissile Mudstone	Clay	Well	Thinly Laminated	Green, Minor Purple	Silica, clay	Clay, Quartz	Floodplain

Table 1. Dominant lithofacies in the Burro Canyon Formation at Ninemile Hill

Burro Canyon. Conglomeratic sandstone (dominantly granule-sized grains) and sandstone facies are commonly associated with fluvial channel complexes, whereas green mudrock is commonly associated with non-amalgamated channel complexes and floodplain environments of deposition.

The detailed stratigraphic section of Ninemile Hill depicts the common facies and their stratigraphic variability (Figure 5). The Burro Canyon Formation at Ninemile Hill is an overall fining-upward succession that contains higher-order fining upward successions. The base of the formation is defined by a conglomeratic sandstone, which is defined by a scour surface and directly overlies the green mudrock of the Jurassic Morrison Formation. Cross-stratified, planar-bedded, and massive sandstones overlie the conglomeratic sandstone in fining-upward intervals ranging in grain size from fine- to coarse-grained. The cross-stratified conglomeratic sandstones are often graded, with larger clasts at the base of the cross-laminae, and fine upwards until the subsequent cross-laminae. Cross-stratification varies from tabular-tangential to low-angle inclined cross-stratification (Figure 7). Green mudrock, fine-grained sandstone, and limestone comprise the upper Burro Canyon. The limestone varies in thickness throughout the outcrop, is characterized by an undulating base, and is not laterally continuous (Figure 9).

Clay Composition of the Upper Burro Canyon Formation

X-ray diffraction (XRD) results after the clay fraction process show that the clay composition of the green mudrock at Ninemile Hill is dominantly illite with mixed-layer illite-smectite (80% illite/20% smectite) (Figure 10). Illite was identified by strong peaks at 10Å, 5 Å, and 3.3 Å. Mixed-layer illite-smectite (80% illite/20% smectite) was identified by reflections at 12.2Å, 9.5Å, 5.1-5.2Å, and 2.5Å. Quartz was identified by peaks at 4.28Å and 3.3Å. These peaks represent remnant quartz that did not get separated out during the clay fraction process. Minor amounts of kaolinite, identified by 3.59Å and 7.2Å, exist in two of the five samples taken

FIGURE 9: CHARACTERISTICS OF THE LIMESTONES FOUND AT NINEMILE HILL

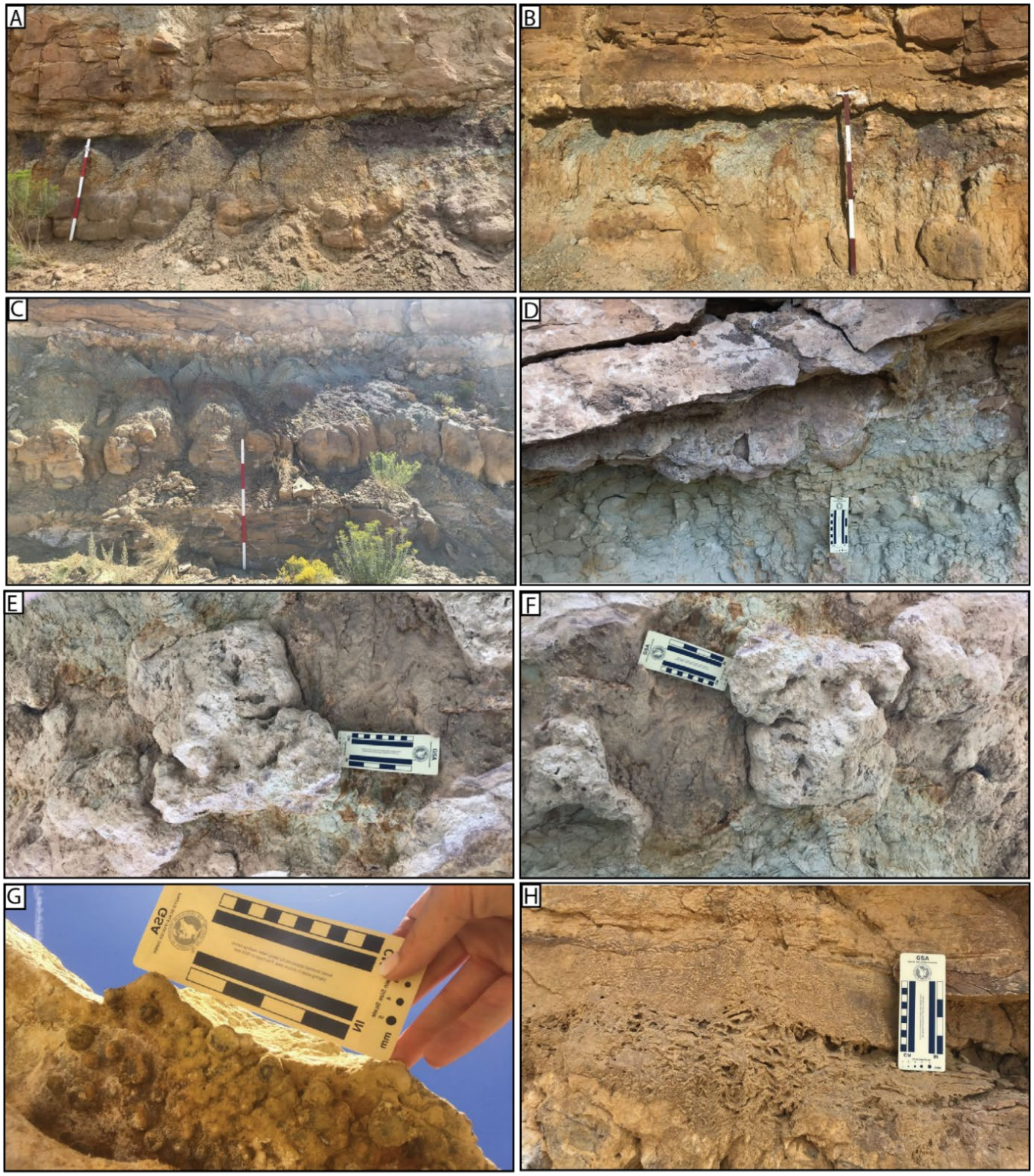

Figure 9. Characteristics of the limestone units. The bases of the limestone units vary in thickness (A; B) and are characterized by an undulated and sometimes nodular base (B; G). Ichnofossils (footprints) exist at the base of the limestone (D). Parts of the green mudstone underneath are eroded, exposing the base of the limestone unit (E; F; G). The base of some of the limestone units contain protruding features characterized by a porous tufa-like texture (E; F). Some of the unit is overlain by a bed containing a similar, calcareous porous texture (H).

FIGURE 10: XRD RESULTS OF NINEMILE HILL

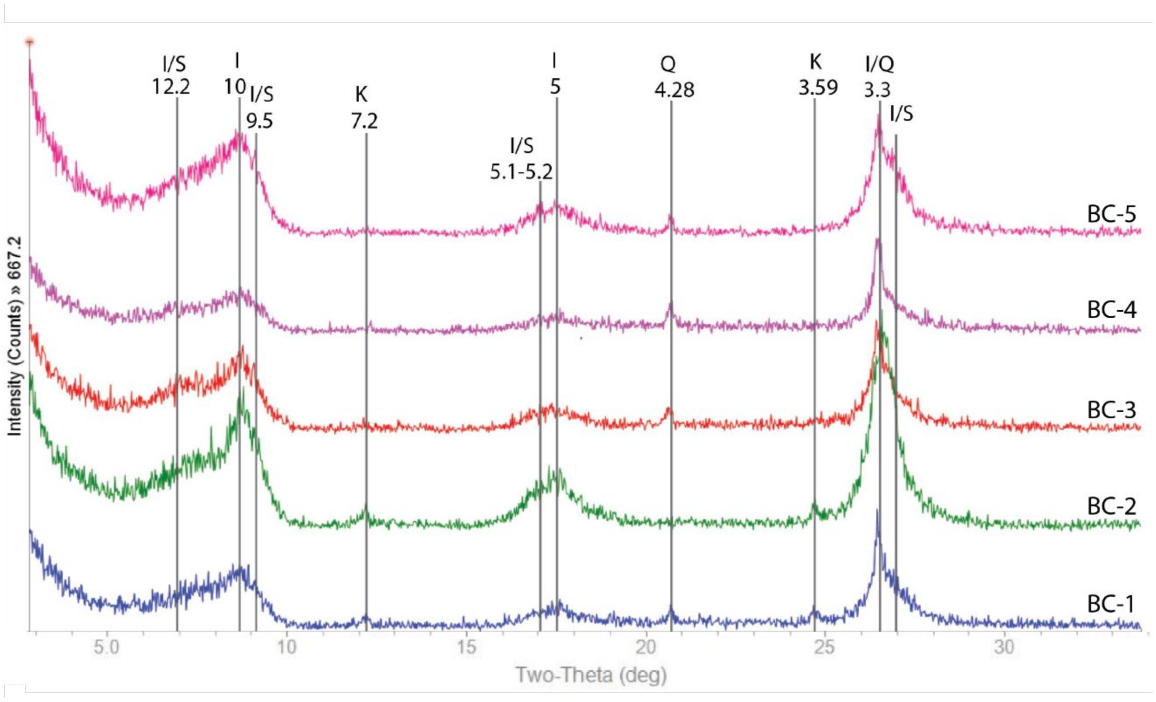

Figure 10. X-ray diffraction results from the clay separation process for the Ninemile Hill samples (N=5) after heat treatment. Samples are ordered stratigraphically. Intensities indicate the presence of illite (10Å, 5 Å, and 3.3 Å) with mixed layer illite-smectite (12.2Å, 9.5Å, 5.1-5.2Å, and 2.5Å). Minor peaks correspond to quartz (4.28Å and 3.3Å) and kaolinite (3.59Å and 7.2Å).

FIGURE 11: XRD RESULTS OF ESCALANTE CANYON

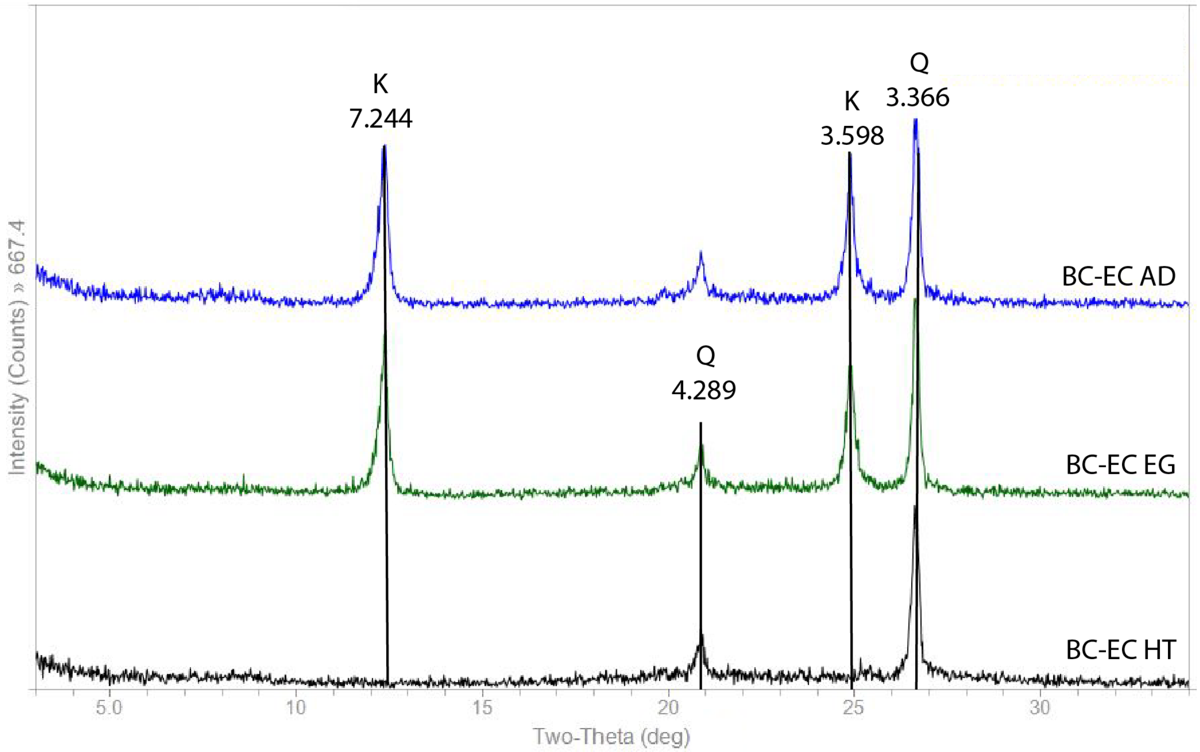

Figure 11. X-ray diffraction results from the clay separation process for the Escalante Canyon sample (N=1). BC-EC AD are the initial results from the air-dried mount, whereas BC-EC EG refers to the results produced from ethylene glycolation. BC-EC HT refers to the final results produced after undergoing heat treatment. Intensities indicate the presence of quartz (4.3Å and 3.4Å) and kaolinite (3.6Å and 7.2Å).

for analyses (BC-1 and BC-2). X-ray diffraction results after the clay fraction process show that the clay composition of the green mudrock at Escalante Canyon is dominantly kaolinite (Figure 11). Kaolinite was identified by strong peaks at 3.59Å and 7.2Å. Quartz was identified by peaks at 4.289Å and 3.366Å. These peaks also represent remnant quartz that did not get separated out during the clay fraction process. However, these peaks are stronger than the ones identified in the Ninemile Hill samples and perhaps indicate a greater proportion of quartz in the samples.

Chemofacies Variability

The stratigraphic variability of elemental abundances was analyzed. Thirty element concentrations were obtained, and six elements were used for interpretation due to their significance as proxies for lithology and depositional environment interpretation: silicon (Si), titanium (Ti), zirconium (Zr), aluminum (Al), potassium (K), calcium (Ca). Several iterations of chemofacies clustering were performed: one using all 30 elements and one using the six indicator elements. Ultimately, the six elements were chosen because they are the most representative of lithology and depositional environments and better capture the heterogeneity of the formation.

First, the data were assembled, color-coded, and grouped into simplified lithologies based on the measured section to visualize their correlation (grey is mudrock, blue is limestone and carbonate-rich lithologies, and yellow is sandstone). Box and whisker plots show that the data correlate well to a higher Al and K content lithology (mudrock), a higher Ca content lithology (limestone and carbonate-rich lithologies), and a higher Si content lithology (sandstone) (Figure 1; Appendix C). The data were plotted and color-coded by lithology to visualize their relationships to each other (Figure 12). As expected, the datapoints with higher K and Al (ppm) correspond with the mudrock lithology, while the higher Si corresponds with sandstone, and the

FIGURE 12: ELEMENTAL CROSS-PLOTS

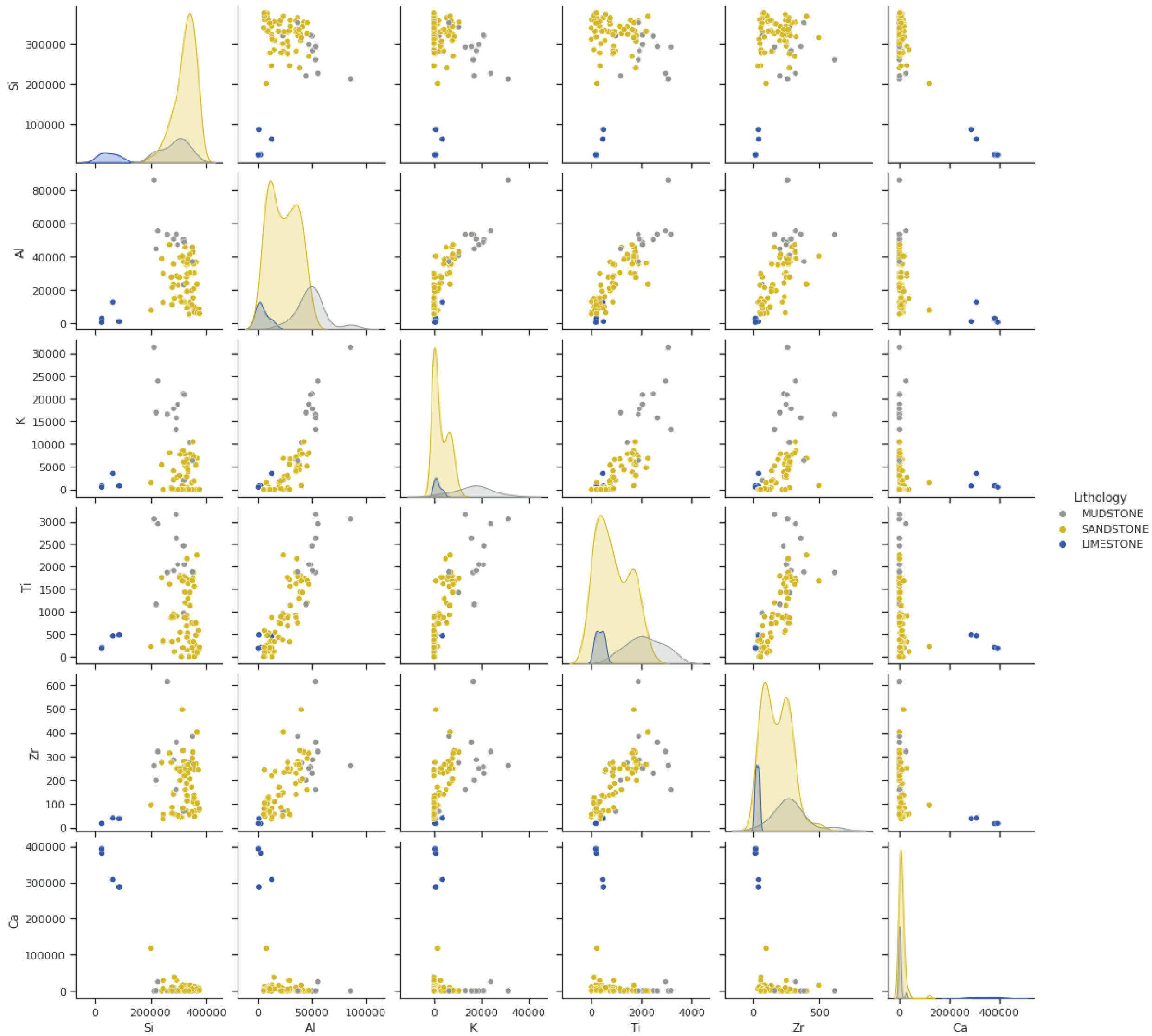

Figure 12. Cross-plots of the six main indicator elements. As expected, the datapoints with higher K and Al (ppm) correspond with the mudstone lithology, the datapoints with higher Si (ppm) correspond with sandstone, and the datapoints with higher Ca (ppm) with limestone. These cross-plots also show a positive relationship between Al, K, and the detrital indicators: Ti, and Zr. The Ca abundance does not appear to have any correlation with detrital elements, and no trend is observed.

higher Ca with limestone and carbonate-rich lithologies. These cross-plots show a positive relationship between the elements Ti, Zr, K, and Al. The Ca abundance does not appear to have any correlation with detrital elements and no trend is observed. Silicon appears to have little to no correlation to Al, K, Ti, and Zr. This is further confirmed by a correlation matrix, also known as a heat map (Figures 2 and 3; Appendix C), showing the relationships between elements. Appendix C, Figure 2 shows the correlation amongst all elements measured, whereas Appendix C, Figure 3 shows the relationship between the six main elements. Silicon appears to have a slight negative relationship between Ti, K and Al and a slight positive relationship to Zr. Again, Zr, Ti, K, and Al have positive relationships, with Al and Ti having the strongest correlation. Calcium has a negative correlation between Si, Al, K, Ti, and Zr, with Si having the strongest negative correlation. The elemental abundances also vary stratigraphically (Figure 4; Appendix C). This figure shows that overall, the outcrop is Si-rich, but Si content decreases towards the upper portion of the section as Al and K increase. Calcium abundance is, for the most part, low until you reach the upper portion of the section, where some limestone and carbonate-rich beds exist. There is, overall, an increase in Ti and Zr up-section, which roughly correspond with the increase in Al and K. This also happens to correlate with a decrease in grain size (i.e. fining upward section) and therefore a decrease in energy.

Before clustering the data into chemofacies, the original distributions of the elemental data were visualized and scaled (Figure 5 and 6; Appendix C). These plots show that the data have different distributions. To cluster the data, the values were scaled using a min-max scalar, and the sum of squares within (SSW) the clusters was determined via the elbow-plot method (Figure 7; Appendix C). The inflection point of the graph indicates an optimal number of clusters to be two, three, or four. However, given the domain knowledge of the lithologies identified in outcrop, three and four clusters were chosen to cluster the data. Two clusters would have been too simple. Clustering with three clusters identified a Si-rich facies, an Al-rich and K-rich facies, and a Ca-rich facies, but was not able to distinguish between the finer-grained sands with minor clay content and the mudrock within the outcrop. Four clusters yielded the greatest results, distinguishing the two contested facies into separate chemofacies.

First, the data were clustered into chemofacies using an unsupervised machine-learning method, k-means. After the data were clustered using k-means, the data were visualized in cross-plots color-coded to chemofacies clusters to analyze how the machine-learning method clustered the data. Appendix C, Figures 8, 9, and 10 show that k-means appeared to cluster the data into a high calcium content facies (chemofacies 3 (3 and 4 clusters)), a facies with higher proportions of aluminum, potassium, zirconium, and titanium (chemofacies 1 (3 clusters); chemofacies 2 (4 clusters)), and a facies that contains higher proportions of silicon (chemofacies 2 (3 clusters); chemofacies 4 (4 clusters)). Clustering with four clusters also yielded another chemofacies that contained relatively high silicon proportions with minor potassium, aluminum, zirconium, and titanium proportions (chemofacies 1) (Figure 10; Appendix C).

Next, the data were clustered into chemofacies using another unsupervised machine-learning technique, hierarchical clustering. After the data were clustered using hierarchical clustering, the data were visualized in cross-plots color coded to chemofacies clusters. Appendix C, Figures 11 and 12 show that hierarchical clustering using three clusters appeared to cluster the data similarly to k-means with subtle differences between the classification results. Clustering using hierarchical clustering with four clusters yielded a similar classification as clustering using k-means with four clusters. The distributions (ppm) of the elemental abundances are shown in color-coded box and whisker plots in Appendix C, Figure 12. These plots show similar chemofacies classification trends as k-means.

The results of the two clustering methods using 3 clusters are summarized in Figure 13. For clustering with 3 clusters, it appears that both methods were able to distinguish the calcium-rich facies from the other lithologies (chemofacies 2) but had a harder time distinguishing between the finer-grained sands with minor clay content and the mudrock within the outcrop. Overall, k-means appears to capture the heterogeneity better than hierarchical clustering using 3 clusters. K-means, in this instance, is able to identify more of the sandstones within the section than hierarchical clustering. The results of the k-means clustering methods using four clusters are summarized in Figure 14. For clustering with 4 clusters, it appears that k-means was able to distinguish the lithofacies in outcrop better than clustering with 3 clusters. The coarse- to medium-grained sandstones mostly correlate with chemofacies 4, whereas the medium-fine grained sandstones with a higher proportion of Al and K mostly correlate with chemofacies 1. Chemofacies 2 and 3 correctly identified the mudrock and limestones, respectively, within the interval. Minor misclassifications exist due to some mudrock containing high amounts of silt.

Porosity and Permeability

Porosity and permeability data are summarized in Table 2. Porosity and permeability values range from 6.1-23.1% and 0.001-1171.8 mD (k-klink values), respectively (Figure 15). There is a positive correlation overall between porosity and permeability. Most datapoints (N=14) are sandstones, which exhibit relatively high porosity and permeability. One datapoint (N=1) is a limestone. Mudrock were not adequately consolidated to acquire core plugs for the types of measurements conducted. Average porosity of the Burro Canyon Formation based on 15

FIGURE 13: CHEMOFACIES RESULTS (3 CLUSTERS)

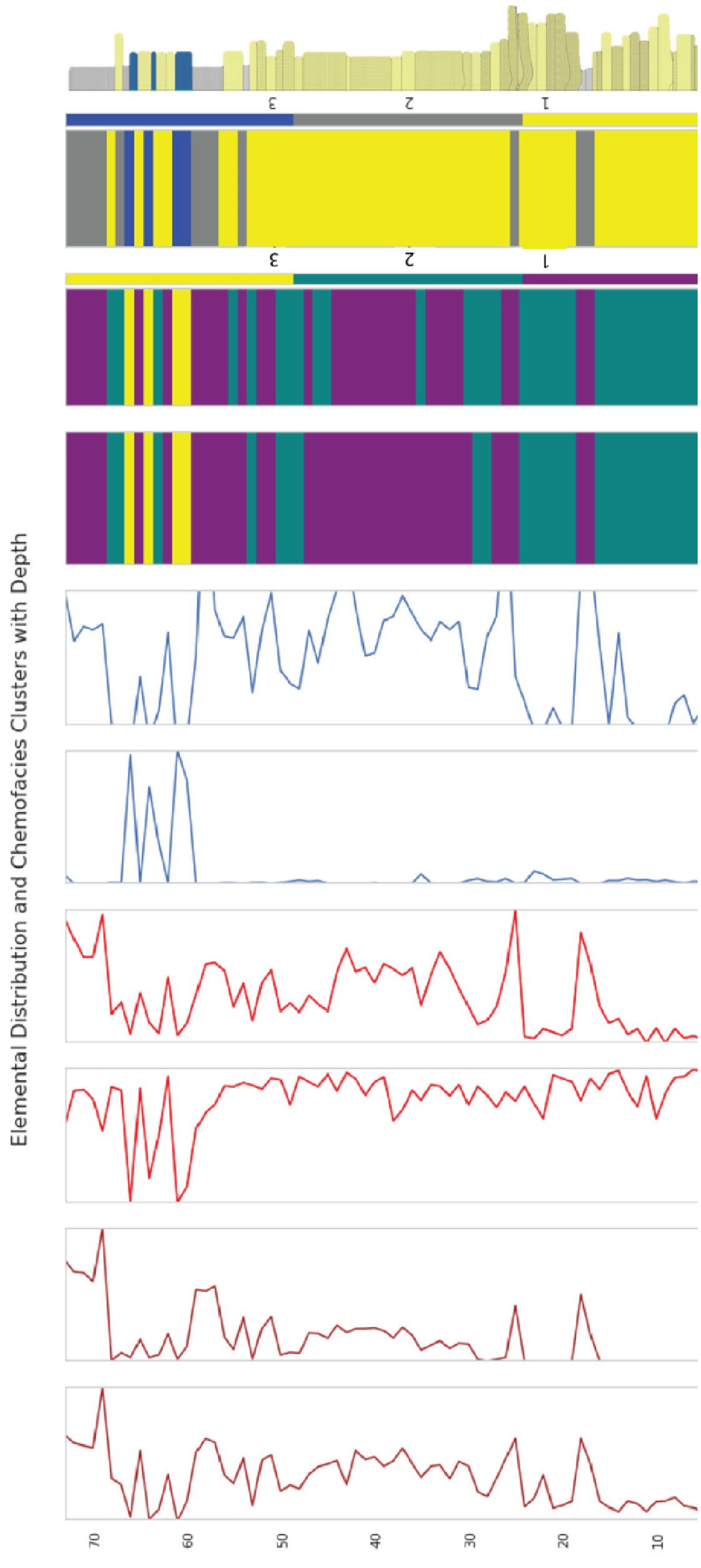

Figure 13. XRF elemental profile of the main indicator elements: Al, K, Si, Ti, Ca, and Zr along with the hierarchical clustering and k-means results using three clusters and a simplified lithology log. Chemofacies one is purple, chemofacies two is teal, and chemofacies three is yellow. In the lithology log, yellow represents sandstones, grey represents mudstones, and blue represents limestone.

FIGURE 14: CHEMOFACIES RESULTS (4 CLUSTERS)

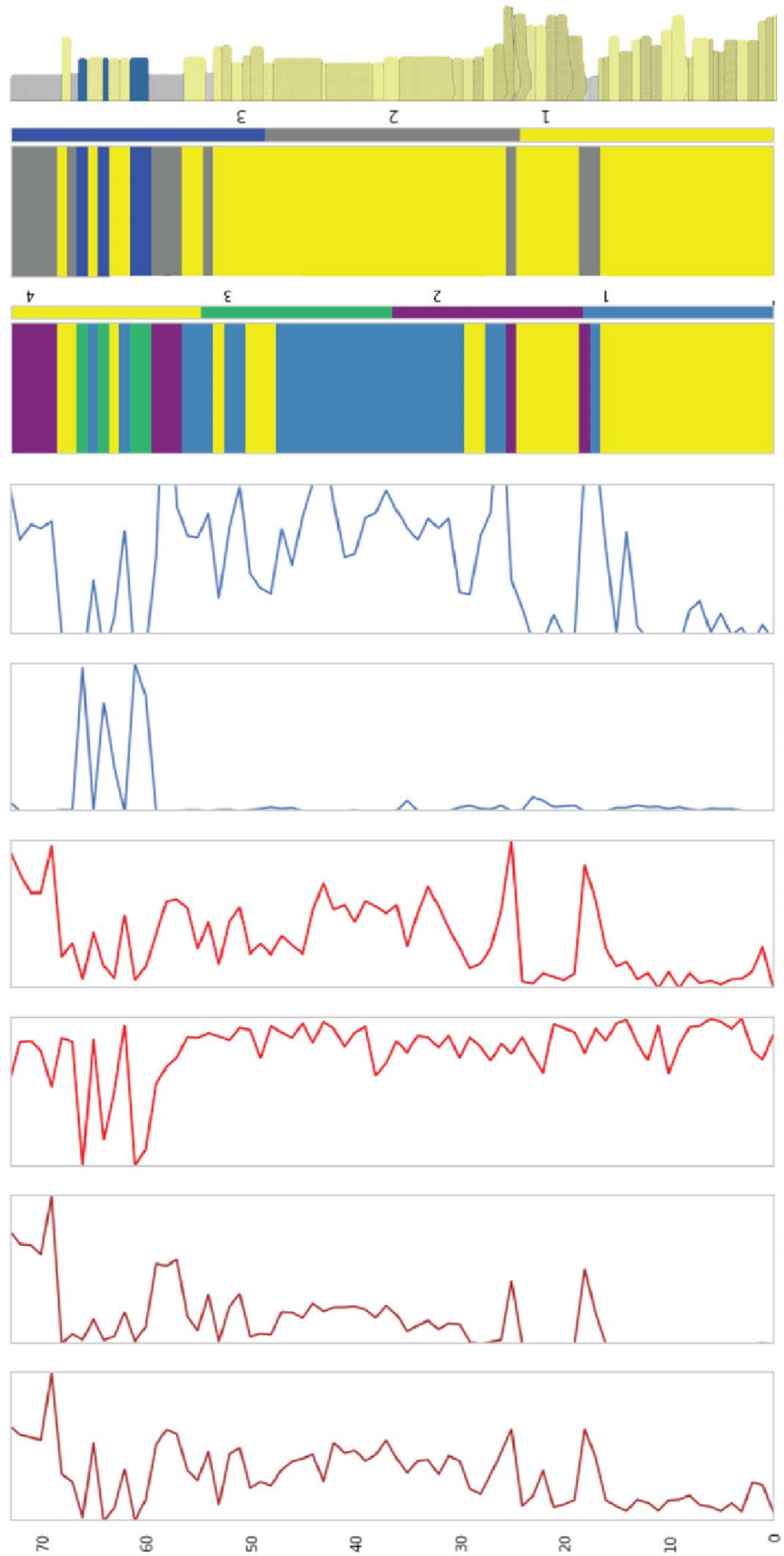

Figure 14. XRF elemental profile of the main indicator elements: Al, K, Si, Ti, Ca, and Zr along with the k-means results using four clusters and a simplified lithology log. Chemofacies one is blue, chemofacies two is purple, chemofacies three is green, and chemofacies four is yellow. In the lithology log, yellow represents sandstones, grey represents mudstones, and blue represents limestone.

TABLE 2: POROSITY AND PERMEABILITY DATA

Sample (ft)	Length(cm)	Diam (cm)	V bulk (cm3)	P conf (psi)	V pore	Porosity (%)	K-air (mD)	K-klink (mD)
BC-68	3.417	2.518	17.016	822.7	1.578	9.274	0.019	0.009
				1494.1	1.333	7.831	0.009	0.004
				2991.4	1.16	6.82	0.003	0.001
BC-62	3.121	2.534	15.74	826.5	2.119	13.462	0.599	0.469
				1508	1.871	11.889	0.54	0.419
				2995.9	1.699	10.794	0.461	0.354
BC-60	3.194	2.537	16.146	824.3	1.376	8.519	0.026	0.013
				1492	1.14	7.059	0.023	0.011
				2977.5	0.983	6.09	0.02	0.01
BC-55	3.366	2.533	16.962	827.8	2.118	12.485	0.068	0.039
				1504.6	1.877	11.065	0.06	0.034
				2971.5	1.696	10.001	0.055	0.031
BC-50	1.746	2.523	8.729	778.4	1.285	14.717	2.629	2.311
				1509.4	1.236	14.158	2.506	2.197
				2966.4	1.134	12.996	2.094	1.82
BC-45	2.714	2.534	13.687	827.3	1.899	13.878	0.331	0.245
				1506.8	1.657	12.106	0.297	0.218
				2977.5	1.573	11.491	0.278	0.202
BC-38	2.967	2.514	14.728	820	2.12	14.392	0.114	0.073
				1494.6	2.072	14.067	0.097	0.06
				2972.8	2.038	13.838	0.083	0.05
BC-35	3.179	2.525	15.919	786.1	2.814	17.676	3.249	2.89
				1501.7	2.799	17.585	3.053	2.707
				2974.2	2.754	17.298	2.792	2.465
BC-30	2.698	2.528	13.542	795	3.132	23.129	258.247	253.892
				1498.8	3.053	22.544	254.288	249.999
				2966.6	3.008	22.211	248.212	243.862
BC-25	2.289	2.515	11.371	794.5	2.166	19.05	822.538	814.291
				1473.3	2.117	18.618	804.55	796.442
				2969.5	2.036	17.902	778.798	770.825
BC-21	3.81	2.517	18.958	810.9	3.203	16.895	315.269	310.332
				1505.2	3.119	16.45	307.118	302.21
				2968.9	3.017	15.915	292.004	287.295
BC-15	2.498	2.528	12.538	792.9	2.073	16.536	510.518	504.222
				1510.7	2.051	16.36	506.068	499.81
				2971.1	1.997	15.929	497.927	491.691
BC-7	2.7	2.51	13.36	794.4	2.091	15.652	305.22	300.468
				1503	2.084	15.602	302.708	297.921
				2989.3	2.039	15.26	297.657	292.923
BC-5	2.495	2.534	12.583	806.5	2.248	17.868	585.151	578.337
				1498.5	2.242	17.815	578.302	571.565
				2988.8	2.203	17.507	564.856	558.178
BC-2	2.929	2.518	14.585	811	3.044	20.871	1181.814	1171.76
				1503.7	2.938	20.145	1127.856	1118.111
				2988.3	2.802	19.211	1069.943	1060.485

Table 2. Porosity and permeability measurements for the Burro Canyon Formation at Ninemile Hill. Porosity and permeability were measured from fifteen core plug samples that were acquired at a 5-ft (1.5-m) sample increment. Samples are ordered stratigraphically.

FIGURE 15: POROSITY AND PERMEABILITY

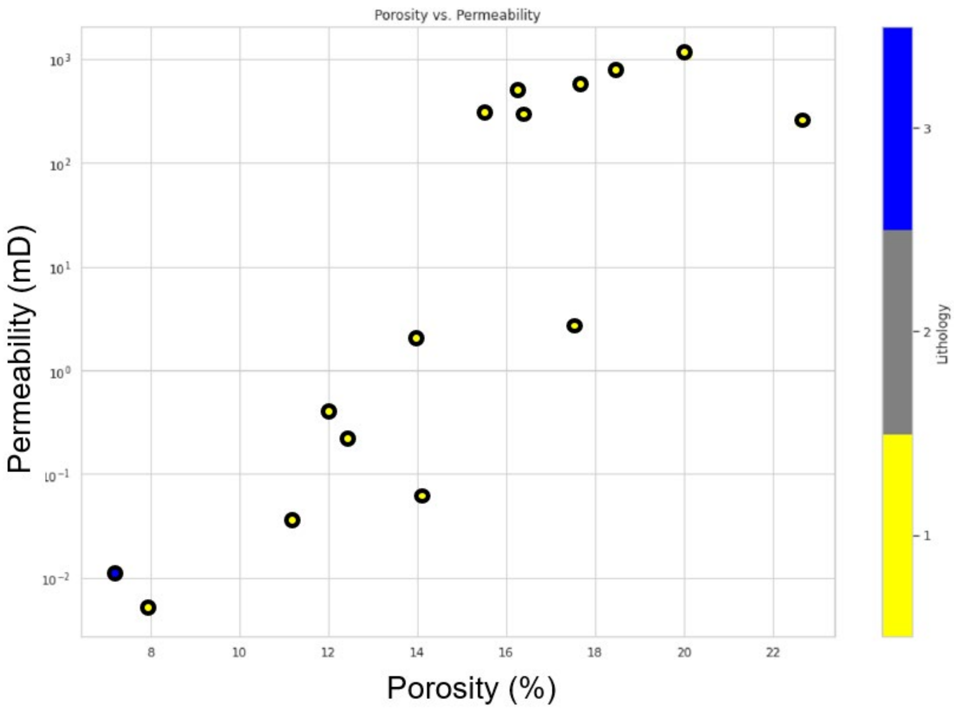

Figure 15. Porosity and permeability data color coded by lithology. Porosity and permeability values range from 6.1-23.1% and 0.001-1171.8 mD, respectively. Overall, as expected, there is a positive correlation between porosity and permeability. Two different trends (groups) are shown, one with lower porosity (6.9-17.5%) and permeability (0.002-10 mD) and one with higher overall porosities (15-23%) and permeabilities close to 1000 mD.

core plugs is 14.9%, and the average permeability is 255 mD. Median porosity is 15.6% and median permeability is 2.7 mD. Overall, porosity and permeability both decrease up section (Figure 5). There is a significant difference in porosity and permeability between the upper and lower Burro Canyon. Average porosity of the lower Burro Canyon is 18.2%, whereas average porosity of the upper Burro Canyon is 12.1%. Average permeability of the lower Burro Canyon is 546 mD and average permeability of the upper Burro Canyon is 0.69 mD. The lowest permeability exists in the unit that roughly corresponds with 68-ft (20.7-m) of the measured section (0.001-0.009 mD). Thin-section petrography and outcrop description show that this sample is a medium-grained, subrounded, poorly sorted, and heavily chert-cemented sandstone. The lowest porosity (6.09-8.52%) corresponds with the only limestone sample (60-ft [18.3-m] in the measured section). Thin-section petrography shows that this sample is a dismicrite that consists of micrite, vein-like sparry calcite, with minor quartz clasts. Pore space is not visible in thin section. The highest porosity exists in the sample taken at 30-ft (9.1-m) in the measured section (22.2-23.1%). Thin-section petrography and outcrop description show that this sample is a medium-grained, subangular, well-sorted sandstone that has consistent intergranular porosity. However, the highest permeability corresponds with the sample at the base of the Burro Canyon (BC-2) (1060.5-1171.8 mD). Thin-section petrography and outcrop description show that this sample is coarse-grained, subrounded, moderately to poorly-sorted, and appears to have both primary (intergranular) and secondary porosity. This sample is also sucrosic, poorly consolidated, and therefore contains limited cement in the form of quartz overgrowths.

To visualize the relationships between porosity, permeability, and sedimentary characteristics, the data was color-coded according to lithofacies, grain size, and sorting (Figure 16). The limestone datapoint was removed for the purposes of this study. These results indicate

FIGURE 16: POROSITY AND PERMEABILITY VS. SEDIMENTARY CHARACTERISTICS

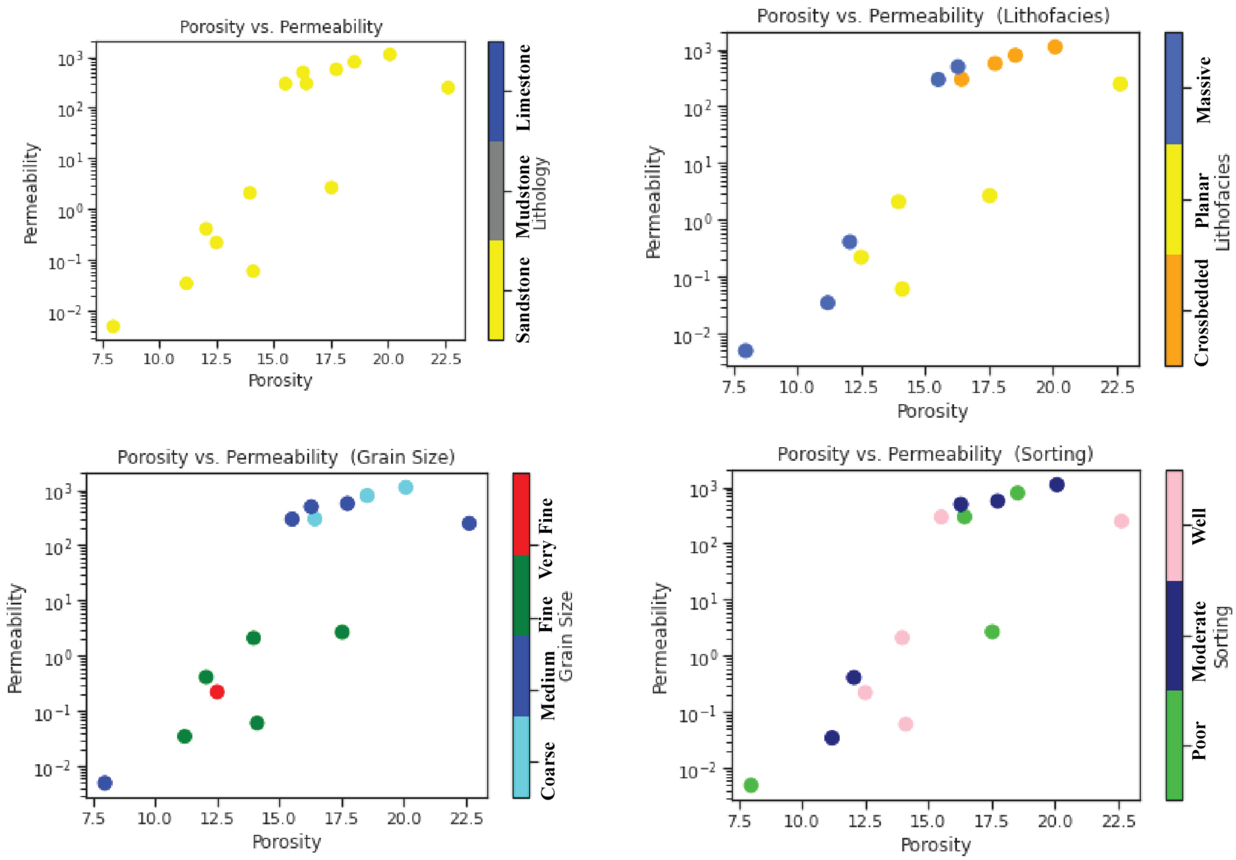

Figure 16. Porosity and permeability measurements color-coded by lithology, lithofacies, grain size, and sorting. The limestone datapoint was removed.

that porosity and permeability are mostly a function of grain size with minor correlations between cross-stratified units and planar-bedded units. These findings correlate with the data from the Mitchell Energy 8-1 Federal Core, where conglomeratic sandstone and cross-stratified sandstone contain the highest porosity and permeability (Figure 16; Appendix C). Sorting appears to not affect porosity and permeability, most likely due to the differences in cementation and dissolved grains that have been observed by thin-section petrography.

The porosity and permeability data were also visualized with the chemofacies classification of hierarchical clustering and k-means (Figures 13 and 14; Appendix C). Using three clusters, chemofacies 2 classified by hierarchical clustering appears to correlate with higher permeabilities and porosities. K-means clustering using three clusters did not yield conclusive results: there is not a strong enough correlation between chemofacies clusters and porosity/permeability data. However, chemofacies clustering using four clusters yielded similar results as that of hierarchical clustering using three clusters. Chemofacies 4 has higher porosities and permeabilities and chemofacies 1 and 3 have relatively lower porosities and permeabilities.

Paleoflow Direction

Paleocurrent data from cross-stratification (N=45) indicate a paleocurrent direction of 145° (vector mean) with a standard deviation of 62° (Figure 13). The average dip angle of the foresets is 20°. The dominant paleocurrent direction at Ninemile Hill is southeasterly. The median of the paleocurrent data is 135°. The average thickness of the cross-stratified sandstones from which the paleocurrent data was acquired is 1.58-ft (0.31-m). The median thickness of the cross-stratified sandstones is 1.67-ft (0.51-m). These paleocurrent data differ from the surrounding outcrops, which have a more easterly to northeasterly vector-mean azimuth (Figure 17).

FIGURE 17: PALEOFLOW SUMMARY

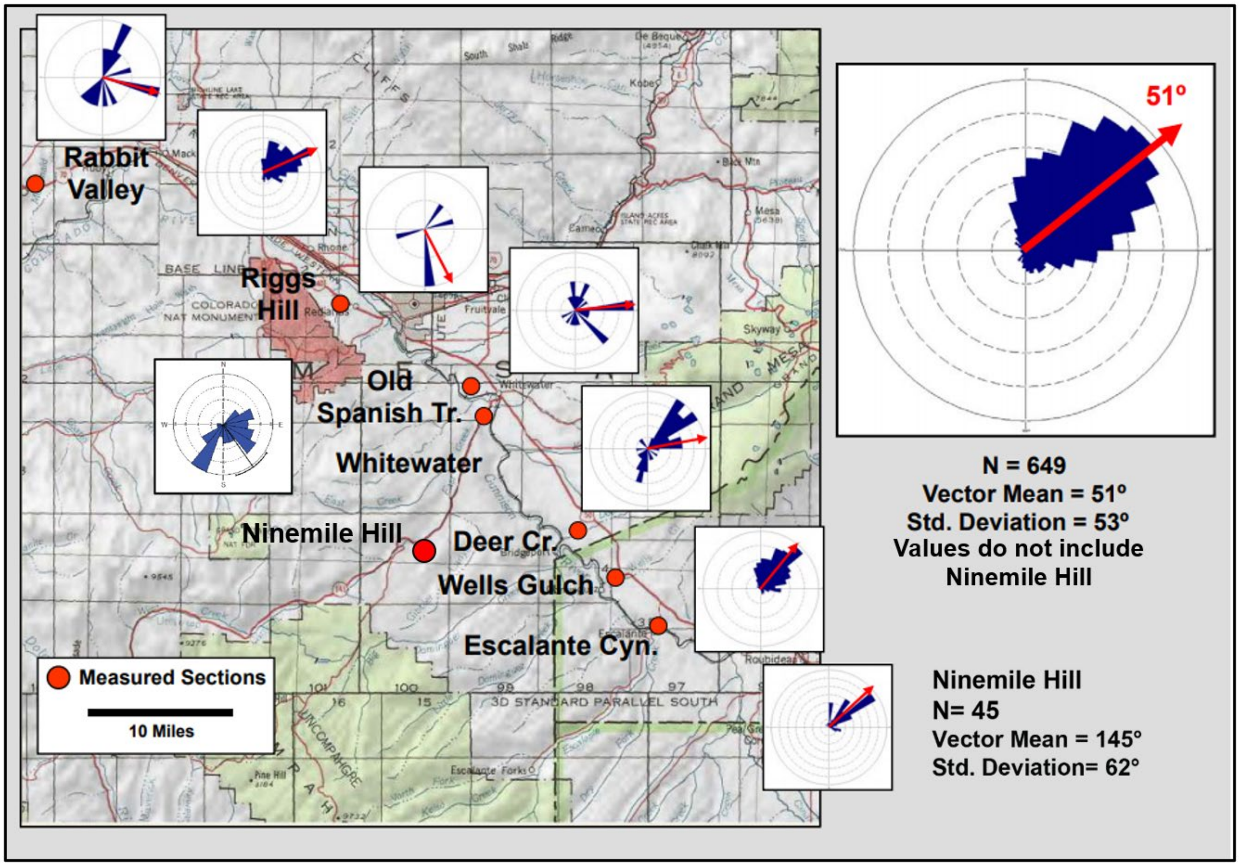

Figure 17. Paleocurrent data of the Ninemile Hill location in relation to other surrounding outcrops. The average paleocurrent direction is 51 degrees taken from 649 samples (which does not include Ninemile Hill samples). At Ninemile hill however, the overall paleocurrent direction corresponds to a SE direction (N=45). This mostly correlates with the Old Spanish Trail and Rabbit Valley outcrops to the north, which have similar paleocurrent directions to the SE. From Cole (2014).

Stratigraphic Architecture

Following the hierarchy of alluvial strata established by Patterson et al. (2002; 2010) and Sprague et al. (2002), three facies associations are defined (smaller-scale hierarchical elements) that stack to form channel complexes (Figure 18). Patterson et al. (2010) defined the channel-fill element as a succession of genetically related bar or bar-set deposits within a channel. The channel-fill elements typically have a concave-up basal geometry and are bounded on top by floodplain lithofacies (mudrock-dominated) when preserved. However, the tops of the channel-fill elements are commonly eroded during subsequent channel scouring and deposition due to the high energy of the fluvial system. The Burro Canyon Formation at Ninemile Hill forms one depositional sequence which is composed of two distinct channel complexes: a lower amalgamated channel complex and an upper non-amalgamated channel complex (Figure 19). The lower amalgamated channel complex is formed by the amalgamation of multiple channel-fill elements. This channel complex is overlain by a non-amalgamated channel complex which dominantly consists of floodplain and lacustrine facies. The channel fill boundaries were determined by the measured section given that the distinct channel fills correspond with scoured bases and basal deposits of slightly conglomeritic sandstones or sands with mud clasts eroded out of the section. The fluvial bar sets each make up the accumulation of beds and bed sets that fine upward.

Based on the dominant lithofacies, three main architectural elements are present within the fluvial strata. The coarse sandy fluvial-bar channel-fill facies and sandy fluvial-bar channel-fill facies comprise the lower amalgamated channel complex and the floodplain and lacustrine deposits comprise the upper non-amalgamated channel complex. The fining upward channel-fill deposits stack vertically and laterally to form the lower amalgamated channel complex. The

FIGURE 18: HIERARCHY OF ARCHITECTURAL ELEMENTS

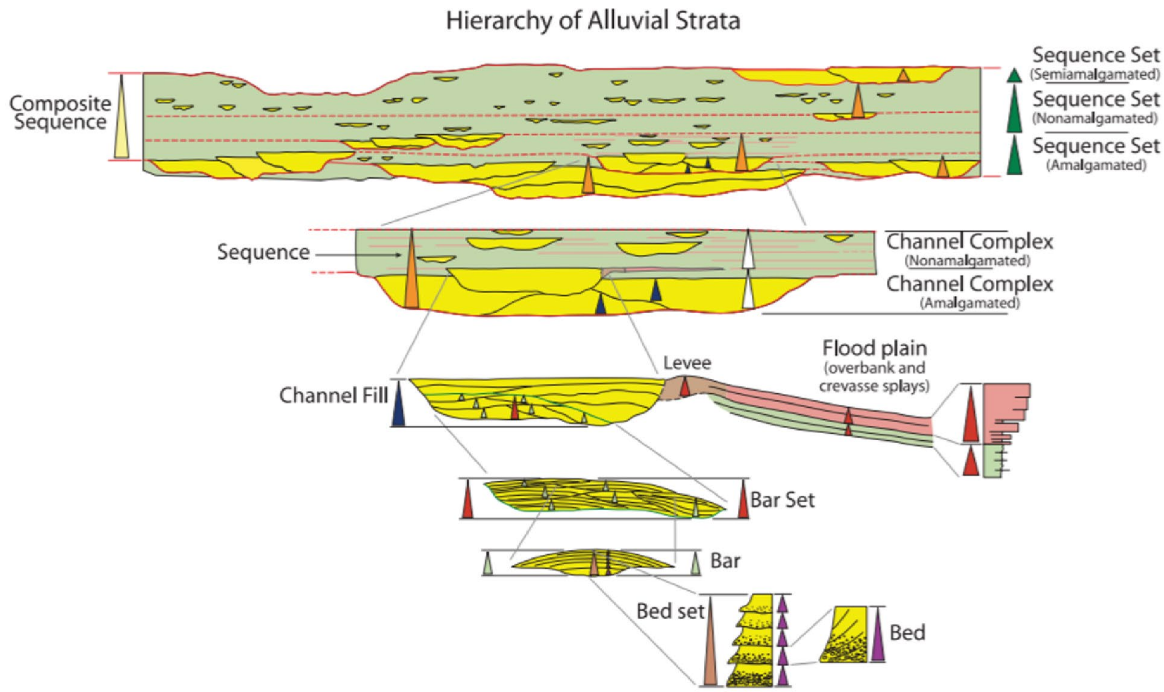

Figure 18. Schematic diagram of alluvial hierarchical elements from the bed scale to composite-sequence scale. Yellow strata consist of fluvial sandstones, green strata consist of floodplain deposits, brown strata represent levee sandstones, and pink strata represent overbank and crevasse splays. Red dashed lines are sequence boundaries. From Patterson et al. (2010), modified from Sprague et al. (2002).

FIGURE 19: STRATIGRAPHIC ARCHITECTURE

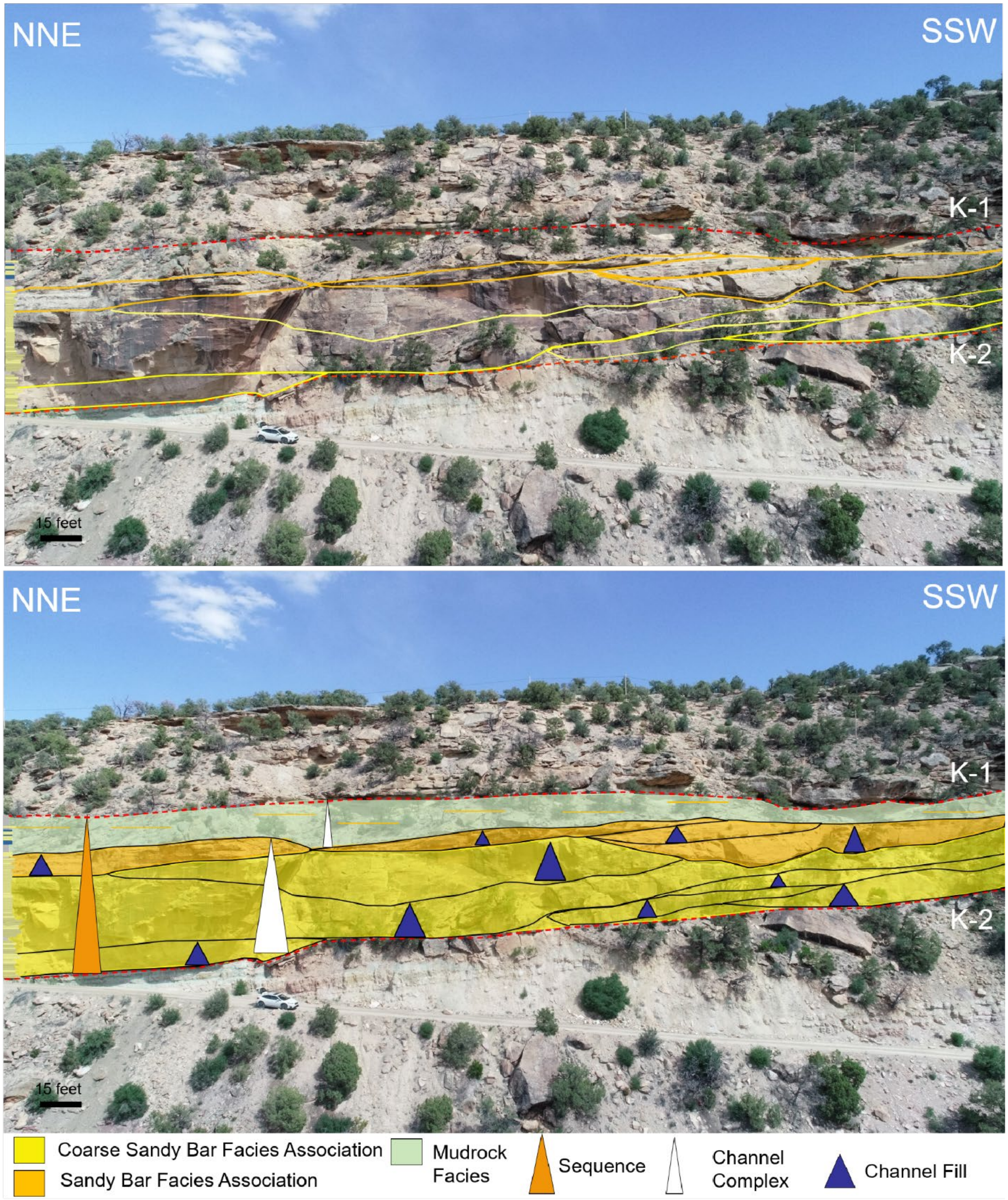

Figure 19. Stratigraphic architecture of the Burro Canyon Formation outcrop at Ninemile Hill. The outcrop is bounded by both the K-1 and K-2 unconformities at the base and top, respectively. It directly overlies the Jurassic Morrison Formation (Jm) and is underlain by the Cretaceous Dakota Formation (Kd). The outcrop is composed of one sequence with two channel complexes: an amalgamated channel complex at the base and a non-amalgamated channel complex at the top. The amalgamated channel complex fines upward and consists of multiple stacked channel fills that vary from a coarse sandy bar facies association to a finer-grained sandy bar facies association.

lowermost channel complex is extremely amalgamated, where the tops of most of the bar successions are eroded out.

Architectural Element 1: coarse sandy fluvial-bar channel-fill facies

Coarse sandy fluvial-bar channel-fill deposits consist of fining-upward successions characterized by basal scour surfaces and conglomeratic sandstones that fine upward into a cross-stratified coarse- to medium-grained sandstone. The cross-stratification varies from tabular-tangential to inclined (Figure 7). Some horizontal planar- and massive-bedding exists. Some channel-fill tops are preserved, which consist of green mudrock facies, but most are eroded. This architectural element mostly correlates with braided transverse and longitudinal bars.

Architectural Element 2: sandy fluvial-bar channel-fill facies

Sandy fluvial-bar channel-fill deposits consist of fining-upward successions characterized by basal scour surfaces and fine- to medium-grained sandstones. Sedimentary structures include horizontal planar- and wavy-bedding. This architectural element mostly correlates with lower sinuosity bar successions.

Architectural Element 3: floodplain and lacustrine deposits

Floodplain and lacustrine deposits are composed of mudrock and limestone facies. The mudrock in the interval ranges in color from green to purple and is thinly laminated. The limestones contain root traces and trace fossils in the form of footprints (Figure 9). The limestones contain variable textures. Some of the limestones are microcrystalline or contain a porous, sponge-like texture and are formed in columnar shapes resembling tufa-like deposits (Figure 2; Appendix A). Some of the limestones are silty/sandy (impure) (Figure 2; Appendix A).

Lateral Variability of the Fluvial Deposits

The stratigraphic column was used to make a simplified cross-section to analyze the lateral and spatial variability of the fluvial deposits. Figure 20 shows a cross-section from the northwest to the southeast that includes Ninemile Hill, Black Ridge, Whitewater, Escalante Canyon, and Rattlesnake Canyon. The Ninemile Hill section is significantly thinner than those at Whitewater, Rattlesnake Canyon, and Escalante Canyon. The Ninemile Hill outcrop is more similar in thickness to Black Ridge. Although each outcrop shares similar facies: floodplain mudrock, fluvial conglomerate, and fluvial sandstone, some minor differences exist. The Ninemile Hill outcrop is the only outcrop within the area to contain limestones within the interval. The Ninemile Hill outcrop is finer in grain size overall. For example, it contains slightly conglomeratic to conglomeratic sandstones whereas the other outcrops contain granule-pebble conglomerates. The floodplain facies are also much thinner at the Ninemile Hill location, yielding a sandier outcrop. With an approximate net-to-gross of 77%, the Ninemile Hill outcrop has a higher net-to-gross ratio of sandstone than Black Ridge, Whitewater, Escalante Canyon, and Rattlesnake Canyon.

DISCUSSION

Chemofacies, Lithofacies, and Environment of Deposition

This study used two unsupervised machine-learning techniques, k-means and hierarchical clustering, to cluster the XRF data and visualize the stratigraphic variability of chemofacies. This study used six elements to cluster the data into chemofacies based off their utility as proxies for lithology and environment of deposition interpretation: silicon (Si), potassium (K), aluminum

FIGURE 20: CROSS-SECTION

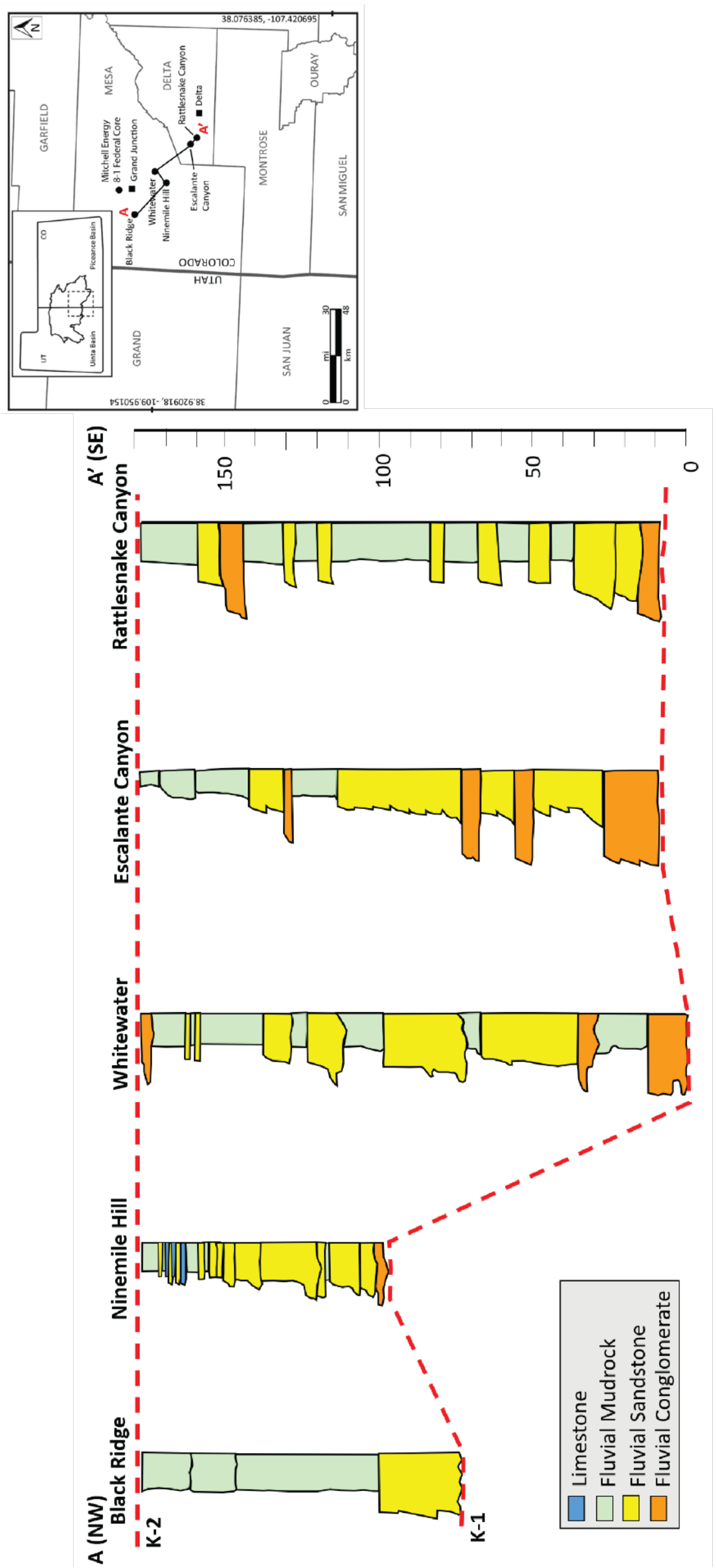

Figure 20. Cross-section through A to A' of the Burro Canyon Formation bounded by the K-1 and K-2 unconformities.

(Al), titanium (Ti), zirconium (Zr), and calcium (Ca) (Pearce and Jarvis, 1992). Silicon is a biogenic and detrital quartz, clay, and feldspar indicator; however, by analyzing Si in tandem with Al and Ti, Si can be used as a proxy for quartz (Pearce and Jarvis, 1992; Pearce et al., 1999; Sageman and Lyons, 2004). In this study, Si is used as a proxy for detrital quartz and is therefore used to identify sandstones and mudrock within the section. Potassium and aluminum are mainly associated with clay minerals but can also be associated with alkali feldspars (Pearce et al., 1999; Tribovillard et al., 2006). In this study, K and Al are assumed to be proxies for clay minerals and therefore mudrock. Titanium and zirconium are used as detrital proxies due to their purely detrital origin and immobility during diagenetic processes (Bhatia and Crook, 1986; Tribovillard et al., 1994; Sageman and Lyons, 2004). Calcium is used as a proxy for calcite and is therefore used as a proxy for calcium carbonate (limestone and carbonate-rich lithologies).

Given the chemofacies clusters determined by these proxies and their stratigraphic variability, a few trends in the elemental data are observed. The variability in chemofacies suggests an increase in more clay- and carbonate-rich lithologies and a decrease in quartz-rich lithologies up section. This transition also correlates with a decrease in grain size and overall increase in clay content. Overall, the section fines-upward, which represents a decrease in the energy of the fluvial system, which correlates with a marine transgression and base level rise (Tellez et al. 2020). The sedimentary structures also suggest a decrease in energy, as the cross-stratification changes from dominantly planar and tabular-tangential cross-stratification to low-angle cross-stratification and ripple-bedding. This data, combined with the lithologic description acquired from outcrop, yield insights into the environment of deposition at Ninemile Hill as it changes through time. The lower Burro Canyon Formation consists of multiple amalgamated channel-fill elements that are characterized by cross-stratification, planar-bedding, massive-bedding, and fining-upward sandstones (slightly conglomeritic sandstones – fine sandstones). Whereas the upper Burro Canyon consists of amalgamated to non-amalgamated channel-fill elements that are characterized by medium- to fine-grained sandstones, laminated green mudrock, and limestones. Given the stacking patterns of the architectural elements and the elemental trends shown through chemofacies clustering, it appears that the transition between chemofacies cluster 1 and 2 (four clusters) marks the shift between a dominantly braided-fluvial system to a low-sinuosity fluvial system as the section transitions to a floodplain- and interfluve-dominated environment of deposition.

The mudrock within the unit represent overbank deposits formed in interfluve areas (Craig, 1982). The presence of limestone lenses also indicates an interfluve environment of deposition: either by deposition through ephemeral fresh-water lakes or ponds (Craig, 1982, Kirkland et al., 1997). The characteristics of the specific limestones within the Ninemile Hill section most likely indicate a paleosol or an ephemeral pond or lake depositional environment that is affected by ground-water processes due to the presence of green and red mudrock. The presence of tufa-like mineral deposits and textures potentially indicate the pond or lake being spring fed (Figure 2; Appendix A). The ichnofossils and root traces also are indicative of a floodplain environment. Since the limestone deposits are not laterally continuous and localized, it most likely represents a local phenomenon of ground-water seepage and spring interaction.

Clay Composition of the Upper Burro Canyon Formation

The differences in clay composition of the upper Burro Canyon Formation green mudrock samples at Ninemile Hill and Escalante Canyon suggest that the clay minerals are laterally heterogeneous. This heterogeneity is due to the local alteration of the clay minerals at Escalante Canyon. The clay composition of the green mudrock section at Ninemile dominantly consists of illite with mixed-layer illite-smectite (80% illite/20% smectite). The presence of illite at Ninemile Hill most likely represents routine detrital deposition within a floodplain environment. This is confirmed by the elemental data showing that the clay content has a positive correlation to the detrital indicators Ti and Zr. At Escalante Canyon, the clay composition consists of kaolinite clay. The presence of kaolinite at Escalante Canyon suggests authigenesis or early diagenesis. This possibly suggests that the clay underwent significant amounts of leaching due to a somewhat acidic environment, either from decaying organic matter in an interfluve- or floodplain-dominated environment or downward percolating acidic ground-water from the coalification process from the coal and carbonaceous mudrock intervals that occur in the lowermost Cretaceous Dakota Formation at Escalante Canyon (Dr. Bill Hood and Dr. Rex Cole, personal communication, February 2021).

Lateral Variability of the Fluvial Deposits

In addition to clay content, the lithology, interval thickness, and net-to-gross ratios of the Burro Canyon Formation vary laterally. The cross-section shown in Figure 20 demonstrates this variability amongst five of the closest outcrops with measured sections to the Ninemile Hill outcrop. These differences have implications for the depositional environment of the Burro Canyon Formation. Previous work based on wells within the Piceance Basin and outcrop locations at Mack Ridge, Whitewater, Deer Creek, Escalante Canyon, and Rattlesnake indicate a paleovalley axis of the Burro Canyon Formation that is centered on Whitewater and trends to the northeast (Tellez et al., 2020). The Ninemile Hill location is directly southwest of Whitewater down the axis of the paleovalley, which based off Tellez et al. (2020), would indicate that Ninemile Hill should be around 220-ft (67.1-m) thick. However, the measured section indicates that the interval thins significantly at Ninemile Hill with a thickness of approximately 73-ft

(22.3-m). This leads to the interpretation that Ninemile Hill is most likely either on the fringes of the paleovalley or was deposited on a paleo-high and endured subsequent paleovalley avulsion once the paleo-low was infilled near Whitewater to Rattlesnake Canyon (most likely an old interfluve of the Jurassic Morrison Formation). Another possible interpretation, based off the paleocurrent data in Figure 17, is that the area represents a tributary coming into the main trunk stream. Overall, there are numerous additional exposures of the Burro Canyon Formation on the Uncompahgre Uplift along the Gunnison River and to the northeast through wells within the Piceance Basin (Tellez et al., 2020). However, more datapoints to the south and southwest of these outcrops is needed to fully understand the nature and trend of the paleovalley axis to the southwest along the Uncompahgre Uplift and Unaweep Canyon.

Reservoir Implications

Outcrop analogs and their associated stratigraphic heterogeneity can provide a more informed subsurface understanding, insight into optimal reservoir targets, and an ability to predict their distribution. Furthermore, chemostratigraphy can also be an excellent tool for stratigraphic correlation and identifying optimal reservoir targets (Duarte et al. 2019). Chemofacies analysis is a simple tool to investigate stratigraphic variability in mineralogy and associated sedimentology. XRF data goes beyond the capabilities of the data acquired from a gamma-ray tool: it identifies a wider range of elements and the relative proportions of those elements (rather than simply K, U, and Th abundance). This type of study can be useful for reservoir quality prediction which has implications for future optimal well placement or reservoir targeting. As shown through chemofacies clustering using four clusters, chemofacies clustering can be useful to identify sandstone lithofacies with optimal reservoir quality (Figure 14; Appendix C). In this study, chemofacies clustering quickly differentiated outcrop-defined sandstones into two separate chemofacies, potentially distinguishing subtle elemental differences that are not as apparent from simple lithologic description. For example, clustering the data (using four clusters) appeared to identify a "cleaner" sand (lower Al and K content that also roughly correlates with grain size) with higher porosities and permeabilities (Figure 14; Appendix C), further differentiating the outcrop-defined sandstones. As shown in Figure 14, chemofacies 4, the most optimal chemofacies from an elemental and reservoir quality standpoint, mostly exists at the base of the formation and correlates with coarse massive- and cross-stratified sands. If these chemofacies zones could be correlated to other outcrop locations, this could be useful for reservoir studies of the Burro Canyon Formation to improve or refine depositional or reservoir models.

CONCLUSIONS

The stratigraphic variability of elements, mineralogy, lithology, lithofacies, chemofacies, and architectural elements of the Burro Canyon Formation suggest that the lower Burro Canyon Formation consists of an amalgamated channel complex that represents a braided-fluvial environment, whereas the upper Burro Canyon Formation consists of a non-amalgamated channel complex that represents a transition to a low-sinuosity fluvial system dominated by floodplain and lacustrine depositional environments. The stratigraphic architecture controls the reservoir heterogeneity of the deposits of the Burro Canyon Formation. Chemofacies analysis proved to be a useful tool in identifying the intervals with the best reservoir quality. Chemofacies clustering therefore can provide information on reservoir quality, identifying elemental relationships to reservoir properties and providing insight into the stratigraphic variability of reservoir quality sands. In conclusion, the study of outcrop analogs and the stratigraphic heterogeneity of fluvial systems provides a more informed subsurface understanding and ability to predict the distribution of optimal reservoirs.

REFERENCES

Bhatia, M.R. and K.A.W. Crook, 1986, Trace element characteristics of greywackes and tectonic setting discrimination of sedimentary basins: Contributions to Mineralogy and Petrology, 92, p. 181-193.

Bish, D.L., and S. Howard, 1988, Quantitative phase analysis using the Rietveld Method: Journal of Applied Crystallography, Vol. 21, No. 2, pp. 86-91.

Case, J.E., 1991, Geologic map of the northwestern part of the Uncompahgre Uplift, Grand County, Utah, and Mesa County, Colorado, with emphasis on Proterozoic rocks: U.S. Geological Survey, p.1-16.

Cashion, W .B., 1973, Geologic and structure map of the Grand Junction quadrangle, Colorado and Utah: U.S. Geological Survey Miscellaneous Geologic Investigations Map 1-736, scale 1:250,000.

Clark, S., 2018, Fluvial architecture of the Burro Canyon Formation using UAV-based photogrammetry- implications for reservoir performance, Escalante Canyon, southwestern Piceance Basin, Colorado, M.S. thesis, University of Oklahoma, Norman, Oklahoma, p. 1-157.

Clark, S. A., M. J. Pranter, Z. A. Reza, and R. D. Cole, 2018, Fluvial architecture of the Burro Canyon Formation using unmanned aerial vehicle-based photogrammetry and outcrop-based modeling: Implications for reservoir performance, Escalante Canyon, southwestern Piceance Basin, Colorado: Interpretation, vol. 6, no. 4, p. T1117-1139.

Cole, R., 2014, Lithofacies, depositional systems, and reservoir characteristics of the Burro Canyon (Cedar Mountain)- Dakota interval, southwest Piceance Basin, Colorado: RMS-SEPM Luncheon Talk, Denver, Colorado.

Craig, L. C., 1982, Uranium potential of the Burro Canyon Formation in western Colorado: United States Department of the Interior Geological Society Open-File Report 82-222, p. 1-25.

DeCelles, P. G., T. F. Lawton, and G. Mitra, 1995, Thrust timing, growth of structural culminations, and synorogenic sedimentation in the type Sevier orogenic belt, western United States: Geology, v. 23; no. 8; p. 699-702.

DeCelles, P.G., 2004, Late Jurassic to Eocene evolution of the Cordilleran Thrust Belt and Foreland basin system, Western USA: American Journal of Science, v. 304, p. 105-168.

Demirel, C., Soreghan, G.S., McCollom, N., Elwood Madden, A.S., Marra, K., and M.E. Elwood Madden, 2018, XRD characterization of Antarctic glacial drift deposits: Implications for quantifying weathering products on Earth and Mars: 49th Lunar and Planetary Science Conference, The Woodlands, Texas, March 19-23, 2018.

Duarte, D., Pires de Lima, R., Slatt, R., and K. Marfurt, 2019, Comparison of clustering techniques to define chemofacies: Case study for Mississippian rocks in the STACK Play, Oklahoma: 2019 AAPG Annual Convention and Exhibition, San Antonio, Texas.

Johnson, R. C., 1989, Geologic history and hydrocarbon potential of Late Cretaceous- age low-permeability reservoirs, Piceance Basin, Western Colorado: U.S. Geological Survey Bulletin, v. 1787-E, p. 51.

Johnson, R. C, and R. M Flores, 2003, History of the Piceance Basin from Latest Cretaceous through Early Eocene and the characterization of Lower Tertiary sandstone reservoirs: Peterson, K.M., Olson, T.M. and Anderson, D.S. (eds) Piceance Basin 2003 Guidebook, Rocky Mountain Association of Geologists, Denver, CO. p. 21-61.

Kirkland, J.I., Britt, B., Burge, D.L., Carpenter, K., Cifelli, R., Decourten, F., Eaton, J., Hasiotis, S., and T. Lawton, 1997, Lower to Middle Cretaceous dinosaur faunas of the central Colorado Plateau: A key to understanding 35 million years of tectonics, sedimentology, evolution and biogeography: Provo, Brigham Young Geology Studies, v. 42, part II., p. 69-103.

Kirkland, J. I., S. K. Madsen, 2007, The Lower Cretaceous Cedar Mountain Formation, eastern Utah: The view up an always interesting learning curve: Geological Society of America Rocky Mountain Section, v. 35, p. 1-108.

Lewis, K. D., M. J. Pranter, Z. A. Reza, and R. D. Cole, 2018, Fluvial architecture of the Burro Canyon Formation using UAV-based photogrammetry and outcrop-based modeling: implications for reservoir performance, Rattlesnake Canyon, southwestern Piceance Basin, Colorado: The Sedimentary Record, Society for Sedimentary Geology, vol. 16, no. 3, p. 4-10.

Lewis, K. D., 2018, Fluvial architecture of the Burro Canyon Formation using UAV-based photogrammetry and outcrop-based modeling: implications for reservoir performance, Rattlesnake Canyon, southwestern Piceance Basin, Colorado, M.S. thesis, University of Oklahoma, Norman, Oklahoma, p. 1-131.

Patterson, P. E., A. R. Sprague, R. E. Hill, and K. M. McDonald, 1995, Sequence stratigraphy and fluvial facies architecture, Farrer and Tuscher Formations (Campanian), Tusher Canyon, Utah: AAPG Abstracts with Program, p. 74A.

Patterson, P. E., T. A. Jones, C. J. Donofrio, A. D. Donovan, and J. D. Ottmann, 2002, Geologic modeling of external and internal reservoir architecture of fluvial systems: in M. Armstrong, C. Bettini, N. Champigny, and A. Galli, eds., Geostatistics Rio 2000, Proceedings of the Geostatistics Sessions of the 31st International Geological Congress, Rio de Janeiro, Brazil: Kluwer Academic Publishers, p. 41-43.

Patterson, P. E., C. R. Jones, and R. L. Skelly, 2010, Hierarchical description and sequence stratigraphy of Cretaceous alluvial strata, Hawkins Field, Texas: in V. Abreu, J. E. Neal,

K. M. Bohacs, and J. L. Kalbas, eds., Sequence Stratigraphy of Siliciclastic Systems – The ExxonMobil Methodology: Tulsa, SEPM (Society for Sedimentary Geology), p. 226.

Pearce, T.J., B.M. Besly, D.S. Wray, and D.K. Wright, 1999, Chemostratigraphy: a method to improve interwell correlation in barren sequences- a case study using onshore Duckmantian/Stephanian sequences (West Midlands, U.K.): Sedimentary Geology, 124, p. 197–220.

Pearce, T.J. and I. Jarvis, 1992, Applications of geochemical data to modelling sediment dispersal patterns in distal turbidites: Late Quaternary of the Madeira Abyssal Plain: Journal of Sedimentary Petrology, 62, p. 1112-1129.

Rowe, H. D., Hughes, N., and K. Robinson, 2012, The quantification and application of handheld energy-dispersive x-ray fluorescence (ED-XRF) in mudrock chemostratigraphy and geochemistry: Chemical Geology 324-325, 122-131.

Sageman, B.B., and T.W. Lyons, 2004, Geochemistry of fine-grained sediments and sedimentary rocks: Mackenzie, F. (ed.) Sediments, Diagenesis, and Sedimentary Rock Treatise on Geochemistry, v. 7, p. 115–158.

Sprague, A. R., P. E. Patterson, R. E. Hill, C. R. Jones, K. M. Campion, J. C. Van Wagoner, M. D. Sullivan, D. K. Larue, H. R. Feldman, T. M. Demko, R. W. Wellner, and J. K. Geslin, 2002, The physical stratigraphy of fluvial strata: A hierarchical approach to the analysis of genetically related stratigraphic elements for improved reservoir prediction: AAPG Annual Convention Abstracts, p. A167-A168.

Stokes, W.L., 1944, Morrison and related deposits in and adjacent to the Colorado Plateau: Geological Society of America Bulletin, Vol. 55, pp. 951-92.

Stokes, W.L. and D.A. Phoenix, 1948, Geology of the Egnar-Gypsum Valley area, San Miguel and Montrose Counties, Colorado: U.S. Geological Survey Prelim. Map 93, Oil and Gas Inv. Ser.

Tellez, J. J., M. J. Pranter, and R. Cole, 2017, Application of UAV-based photogrammetry for outcrop characterization of fluvial deposits of the Burro Canyon Formation, Piceance Basin, Colorado: 7th International Symposium on Hydrocarbon Accumulation Mechanism and Petroleum Resources Evaluation, Beijing, China, Oct 2017.

Tellez, J. J., M. J. Pranter, and R. Cole, 2018a, Application of UAV-based photogrammetry for outcrop characterization of fluvial deposits of the Burro Canyon Formation, Piceance Basin, Colorado: The Outcrop, v. 67, no. 3, May 2018.

Tellez, J. J., K. Lewis, S. Clark, R. Cole, M. J. Pranter, and Z. A. Reza, 2018b, Exploring multi-scale heterogeneity of braided-fluvial reservoirs: implications for reservoir performance: AAPG Annual Convention and Exhibition, Salt Lake City, UT, May 2018.

Tellez, J. J., M. J. Pranter, and R. Cole, 2019a, UAV-based photogrammetry for facies architecture and fluvial sequence stratigraphic definition of the Burro Canyon Formation, Piceance Basin, Colorado: AAPG International Conference and Exhibition, Buenos Aires, Argentina, Aug 2019.

Tellez, J. J., M. J. Pranter, and R. Cole, 2019b, Fluvial architecture and sequence stratigraphy of the Burro Canyon Formation using UAV-based outcrop models, southwestern Piceance Basin, Colorado: AAPG Rocky Mountain Section Convention Program, Cheyenne, Wyoming, Sep 2019.

Tellez, J. J., M. J. Pranter, and R. Cole, 2020, Fluvial architecture and sequence stratigraphy of the Burro Canyon Formation, southwestern Piceance Basin, Colorado: Interpretation, Vol. 8, No. 4.

Tribovillard, N., T.J. Algeo, T.W. Lyons, and A. Riboulleau, 2006, Trace metals as paleoredox and paleoproductivity proxies: An update: Chem. Geol., v. 232, p. 12–32.

Tweto, O., 1975, Laramide (Late Cretaceous-Early Tertiary) orogeny in the southern Rocky Mountains: in Curtis, B.F., ed., Cenozoic history of the Southern Rocky Mountains: Geological Society of America Memoir 144, p.1-44.

Williams, P.L., 1964, Geology, structure, and uranium deposits of the Moab quadrangle, Colorado and Utah: U.S. Geological Survey Miscellaneous Geologic Investigations Map 1-360, scale 1:250,000.

Young, R. G., 1960, Dakota group of Colorado Plateau: Bulletin of the American Association of Petroleum Geologists, v. 44, p. 156–194.

Young, R. G., 1970, Lower Cretaceous of Wyoming and the southern Rockies: The Mountain Geologist, v. 7, p. 105–121.

Young, R. G., 1973, Depositional environments of basal Cretaceous rocks of the Colorado Plateau: in J. E. Fassett, ed., Cretaceous and Tertiary rocks of the Southern Plateau: A memoir of the four corners geological society: Four Corners Geological Society, p. 10–27.

Young, R. G., 1975, Lower Cretaceous rocks of northwestern Colorado and northeastern Utah: Proceedings of the Rocky Mountain Association of Geologists Symposium, p. 141–147.

APPENDIX A: OUTCROP DESCRIPTION

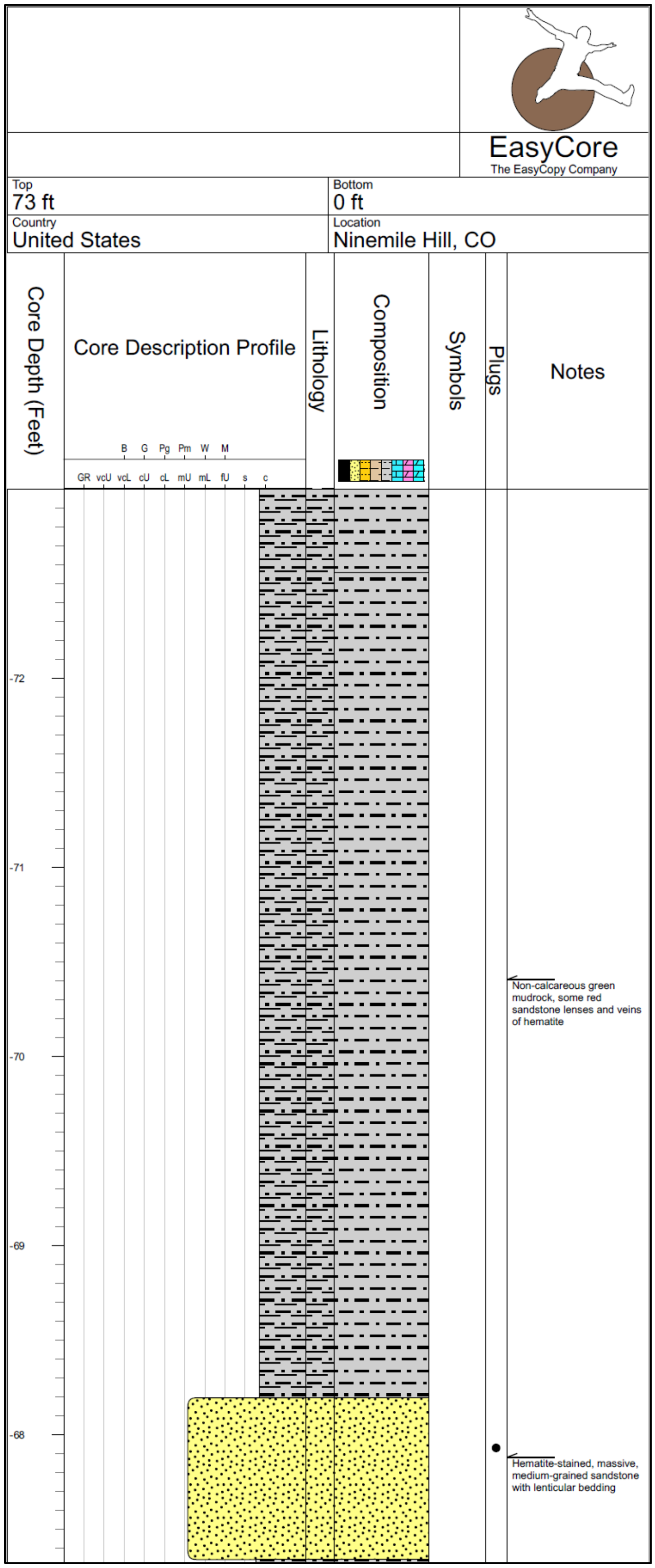

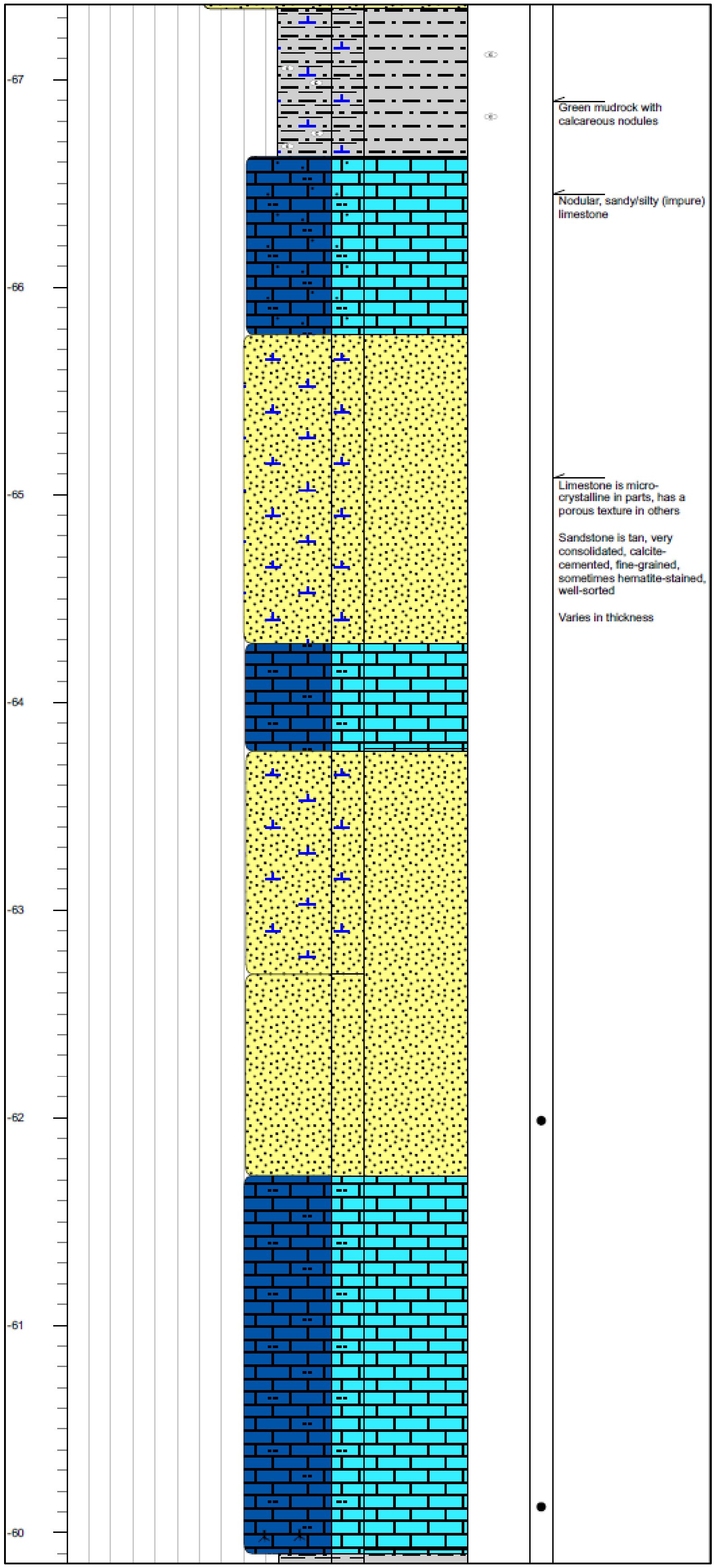

-67
-66
-65
-64
-63
-62
-61
-60
Green mudrock with calcareous nodules
Nodular, sandy/silty (impure) limestone
Limestone is micro-crystalline in parts, has a porous texture in others
Sandstone is tan, very consolidated, calcite-cemented, fine-grained, sometimes hematite-stained, well-sorted
Varies in thickness

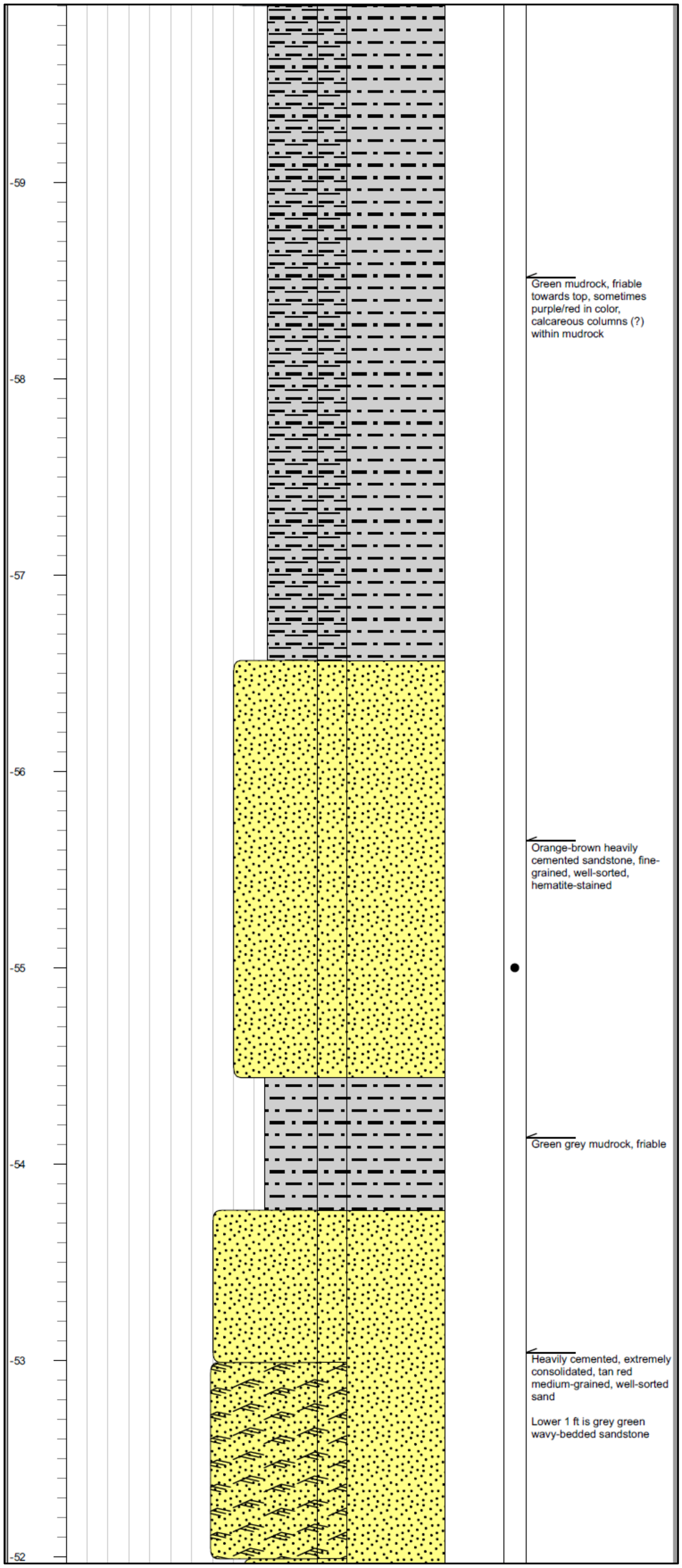
-59
-58
-57
-56
-55
-54
-53
-52
Green mudrock, friable towards top, sometimes purple/red in color, calcareous columns (?) within mudrock
Orange-brown heavily cemented sandstone, fine-grained, well-sorted, hematite-stained
Green grey mudrock, friable
Heavily cemented, extremely consolidated, tan red medium-grained, well-sorted sand
Lower 1 ft is grey green wavy-bedded sandstone

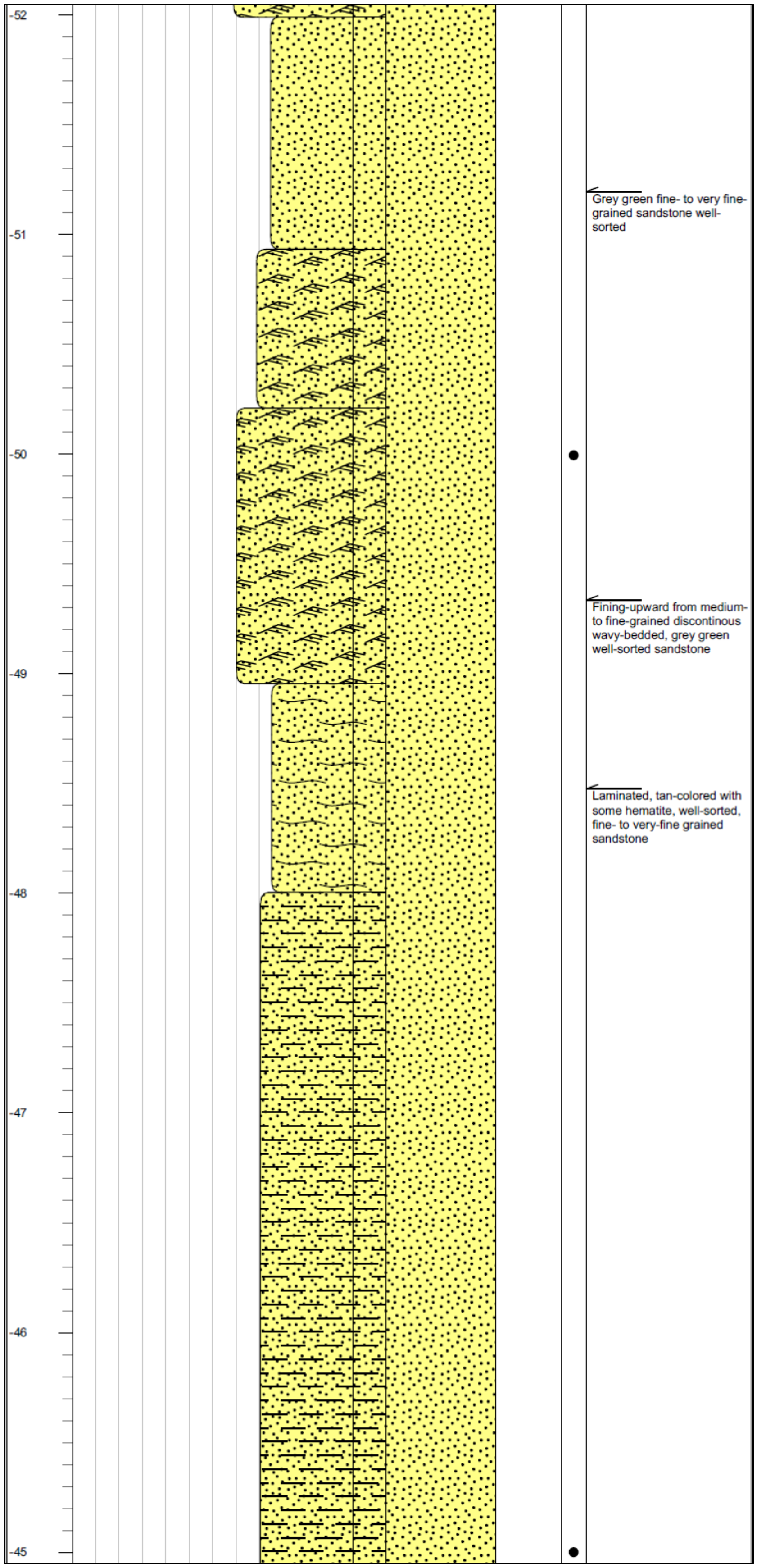
-52
-51
-50
-49
-48
-47
-46
-45
Grey green fine- to very fine-grained sandstone well-sorted
Fining-upward from medium- to fine-grained discontinous wavy-bedded, grey green well-sorted sandstone
Laminated, tan-colored with some hematite, well-sorted, fine- to very-fine grained sandstone

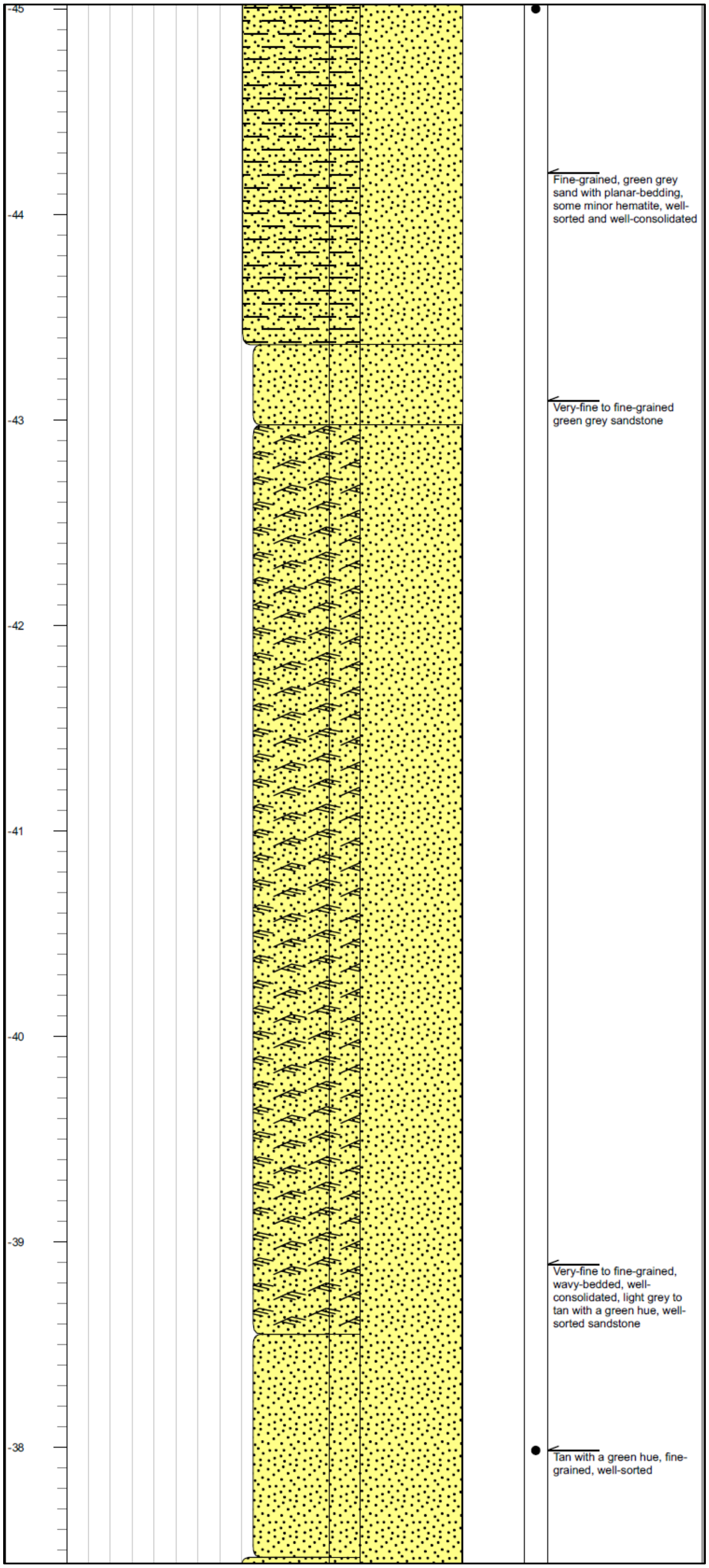
-45
-44
-43
-42
-41
-40
-39
-38
Fine-grained, green grey sand with planar-bedding, some minor hematite, well-sorted and well-consolidated
Very-fine to fine-grained green grey sandstone
Very-fine to fine-grained, wavy-bedded, well-consolidated, light grey to tan with a green hue, well-sorted sandstone
Tan with a green hue, fine-grained, well-sorted

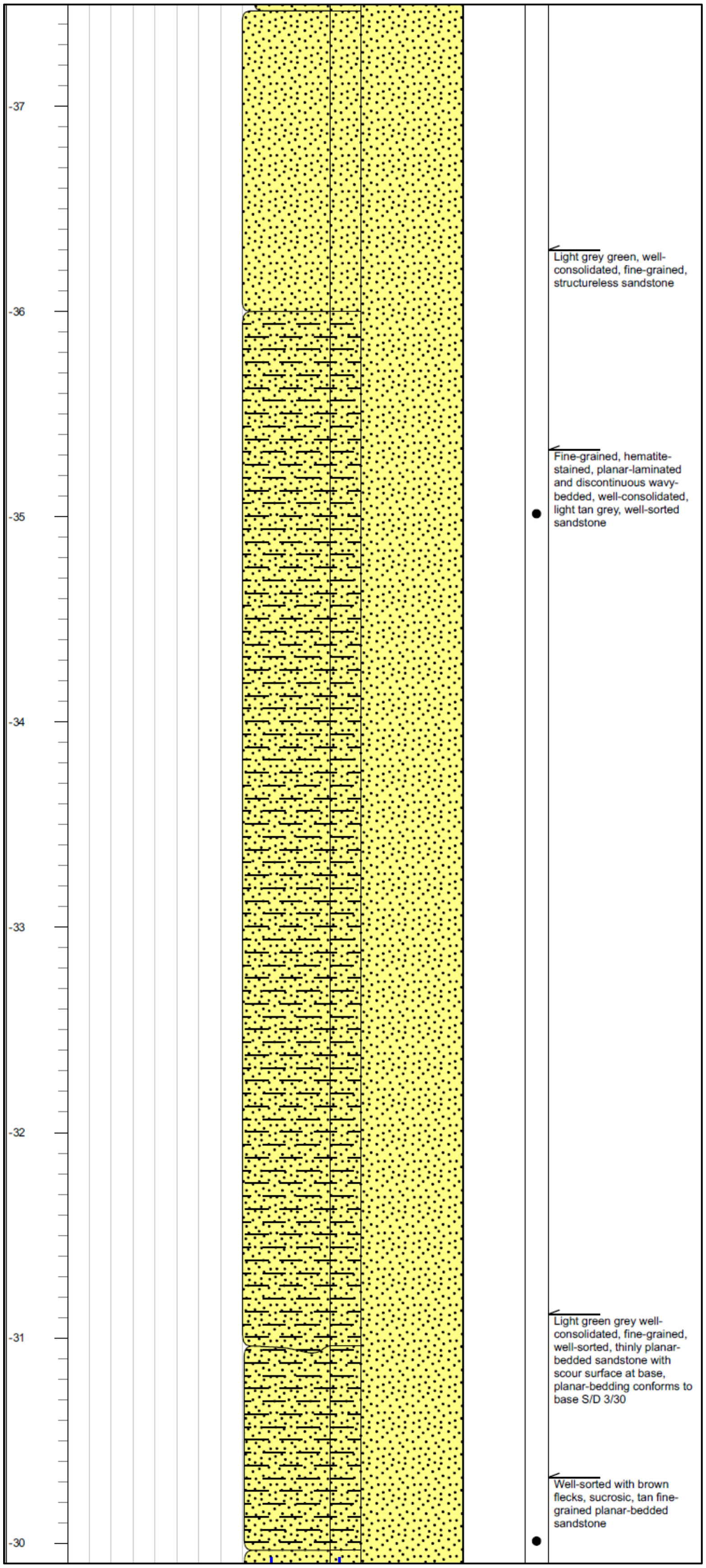
-37
-36
-35
-34
-33
-32
-31
-30
Light grey green, well-consolidated, fine-grained, structureless sandstone
Fine-grained, hematite-stained, planar-laminated and discontinuous wavy-bedded, well-consolidated, light tan grey, well-sorted sandstone
Light green grey well-consolidated, fine-grained, well-sorted, thinly planar-bedded sandstone with scour surface at base, planar-bedding conforms to base S/D 3/30
Well-sorted with brown flecks, sucrosic, tan fine-grained planar-bedded sandstone

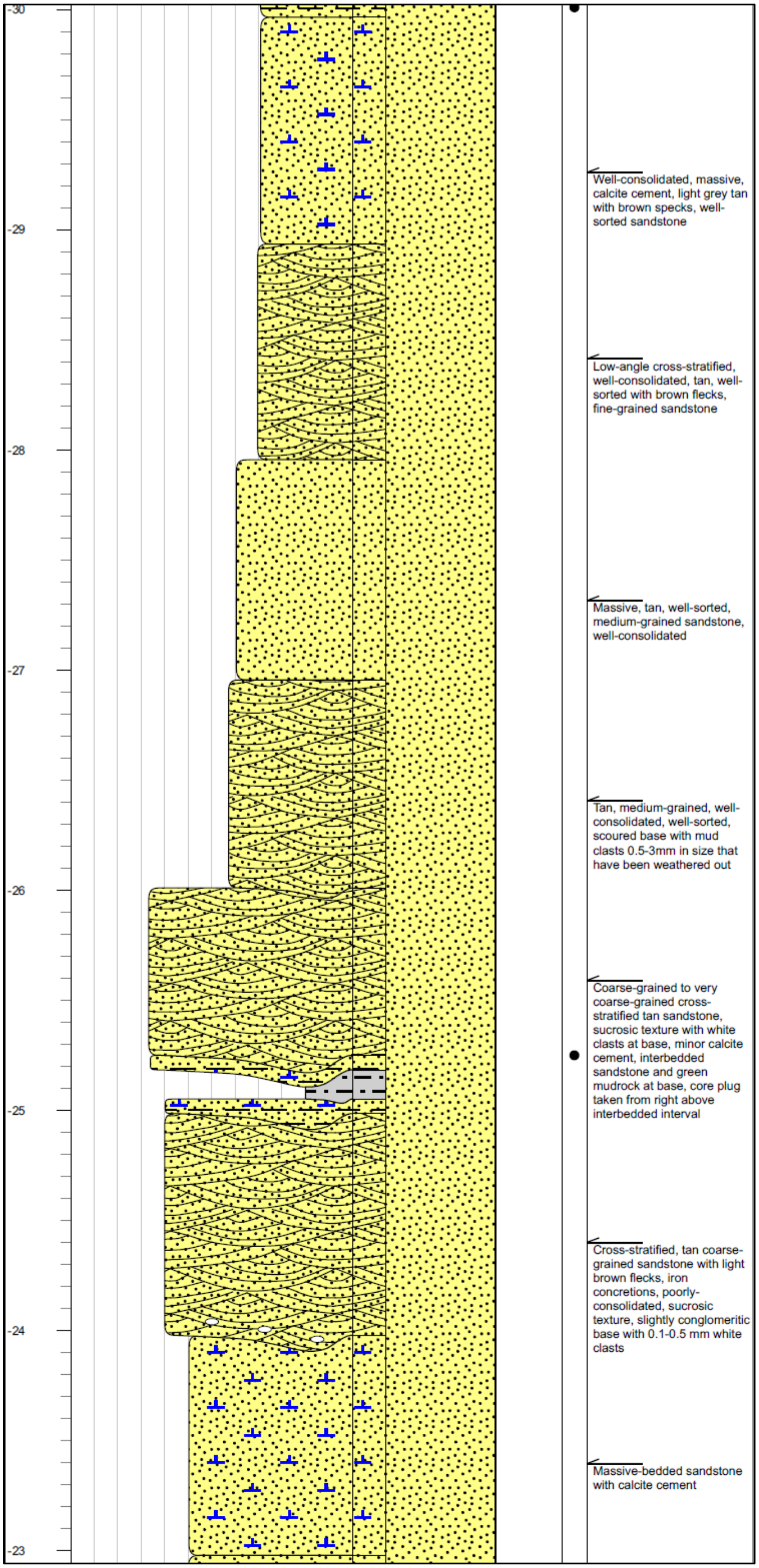
-30
-29
-28
-27
-26
-25
-24
-23
Well-consolidated, massive, calcite cement, light grey tan with brown specks, well-sorted sandstone
Low-angle cross-stratified, well-consolidated, tan, well-sorted with brown flecks, fine-grained sandstone
Massive, tan, well-sorted, medium-grained sandstone, well-consolidated
Tan, medium-grained, well-consolidated, well-sorted, scoured base with mud clasts 0.5-3mm in size that have been weathered out
Coarse-grained to very coarse-grained cross-stratified tan sandstone, sucrosic texture with white clasts at base, minor calcite cement, interbedded sandstone and green mudrock at base, core plug taken from right above interbedded interval
Cross-stratified, tan coarse-grained sandstone with light brown flecks, iron concretions, poorly-consolidated, sucrosic texture, slightly conglomeritic base with 0.1-0.5 mm white clasts
Massive-bedded sandstone with calcite cement

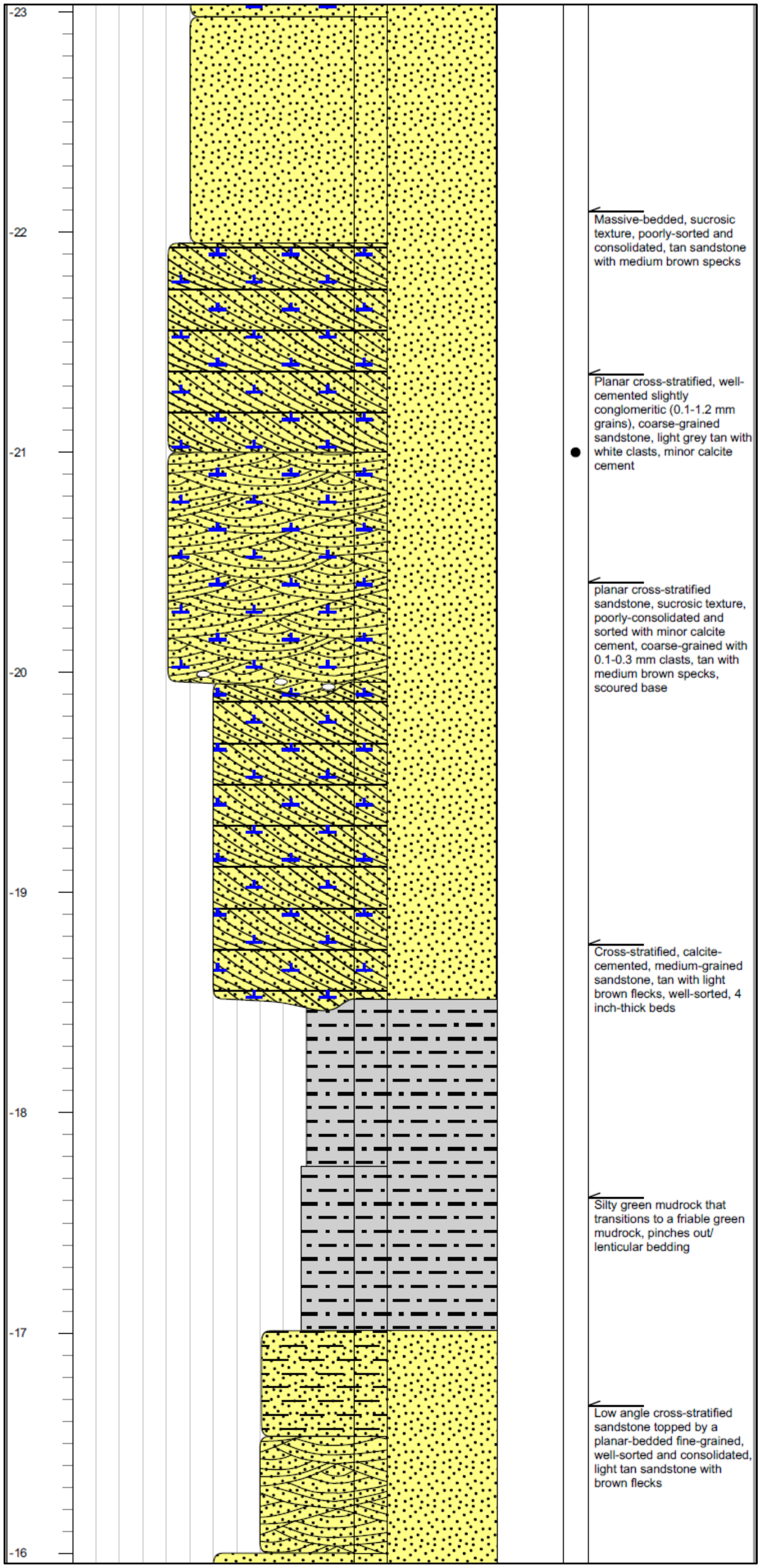
-23
-22
-21
-20
-19
-18
-17
-16
Massive-bedded, sucrosic texture, poorly-sorted and consolidated, tan sandstone with medium brown specks
Planar cross-stratified, well-cemented slightly conglomeritic (0.1-1.2 mm grains), coarse-grained sandstone, light grey tan with white clasts, minor calcite cement
planar cross-stratified sandstone, sucrosic texture, poorly-consolidated and sorted with minor calcite cement, coarse-grained with 0.1-0.3 mm clasts, tan with medium brown specks, scoured base
Cross-stratified, calcite-cemented, medium-grained sandstone, tan with light brown flecks, well-sorted, 4 inch-thick beds
Silty green mudrock that transitions to a friable green mudrock, pinches out/ lenticular bedding
Low angle cross-stratified sandstone topped by a planar-bedded fine-grained, well-sorted and consolidated, light tan sandstone with brown flecks

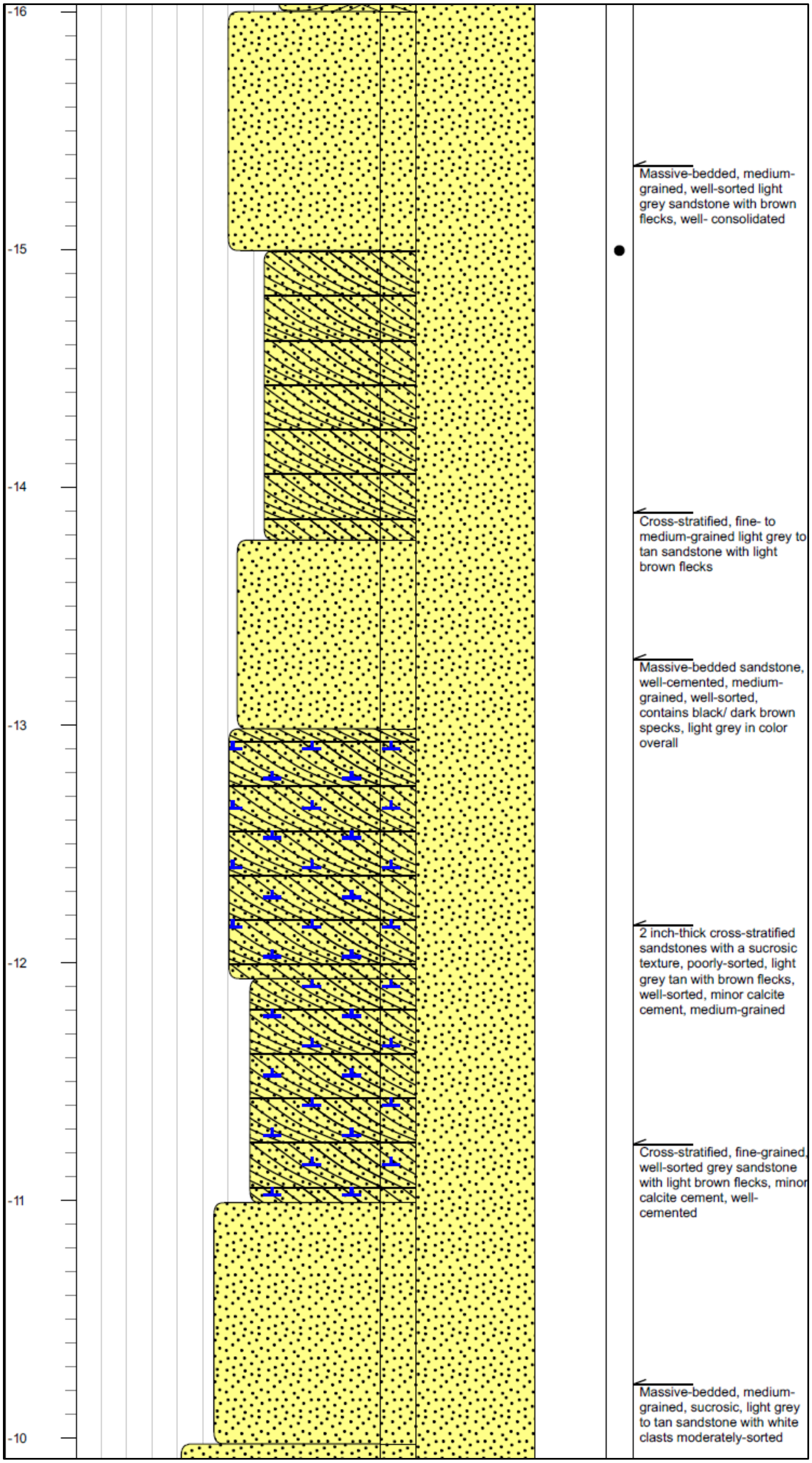
-16
-15
-14
-13
-12
-11
-10
Massive-bedded, medium-grained, well-sorted light grey sandstone with brown flecks, well- consolidated
Cross-stratified, fine- to medium-grained light grey to tan sandstone with light brown flecks
Massive-bedded sandstone, well-cemented, medium-grained, well-sorted, contains black/ dark brown specks, light grey in color overall
2 inch-thick cross-stratified sandstones with a sucrosic texture, poorly-sorted, light grey tan with brown flecks, well-sorted, minor calcite cement, medium-grained
Cross-stratified, fine-grained, well-sorted grey sandstone with light brown flecks, minor calcite cement, well-cemented
Massive-bedded, medium-grained, sucrosic, light grey to tan sandstone with white clasts moderately-sorted

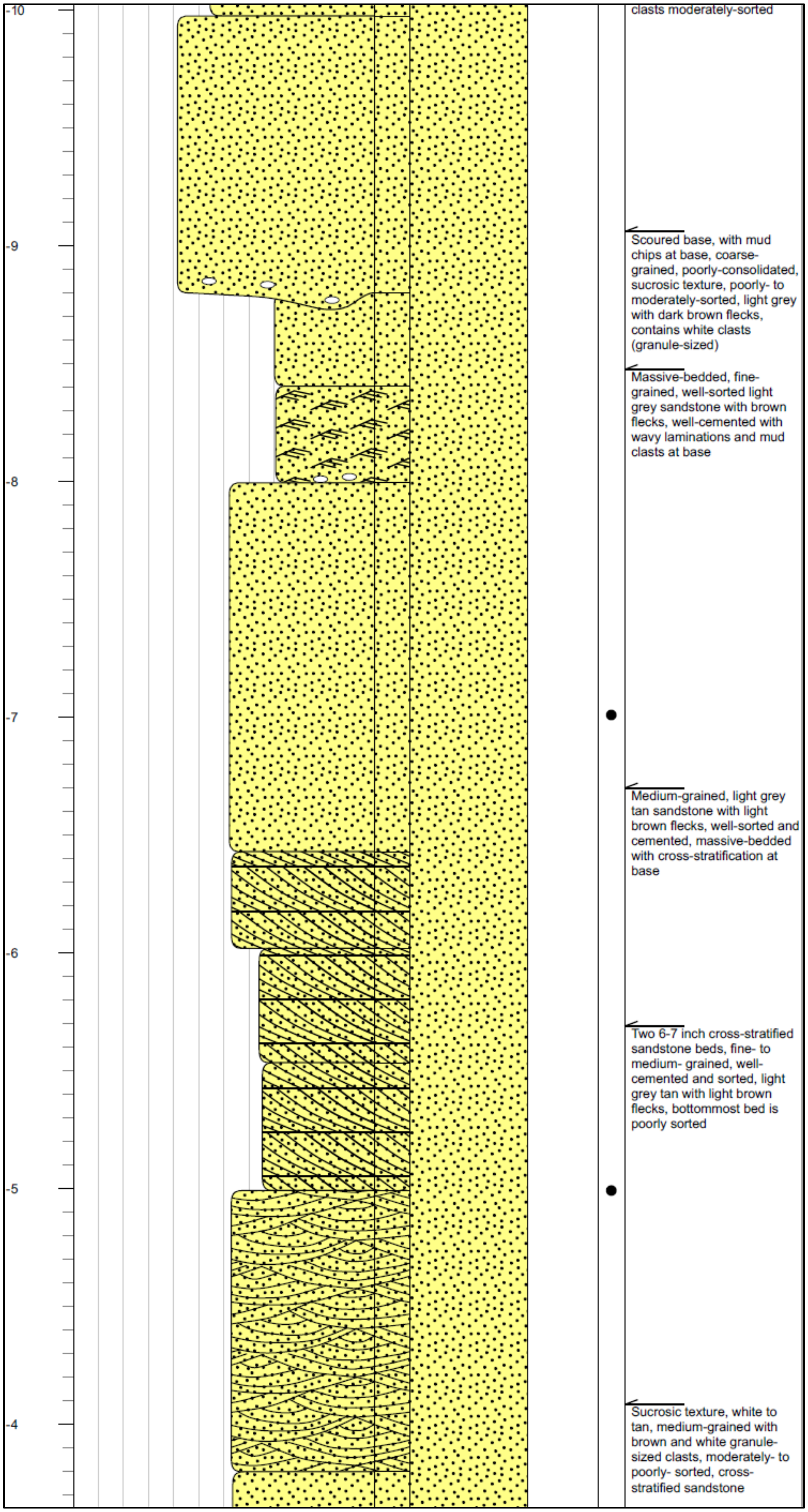
-10
-9
-8
-7
-6
-5
-4
clasts moderately-sorted
Scoured base, with mud chips at base, coarse-grained, poorly-consolidated, sucrosic texture, poorly- to moderately-sorted, light grey with dark brown flecks, contains white clasts (granule-sized)
Massive-bedded, fine-grained, well-sorted light grey sandstone with brown flecks, well-cemented with wavy laminations and mud clasts at base
Medium-grained, light grey tan sandstone with light brown flecks, well-sorted and cemented, massive-bedded with cross-stratification at base
Two 6-7 inch cross-stratified sandstone beds, fine- to medium- grained, well-cemented and sorted, light grey tan with light brown flecks, bottommost bed is poorly sorted
Sucrosic texture, white to tan, medium-grained with brown and white granule-sized clasts, moderately- to poorly- sorted, cross-stratified sandstone

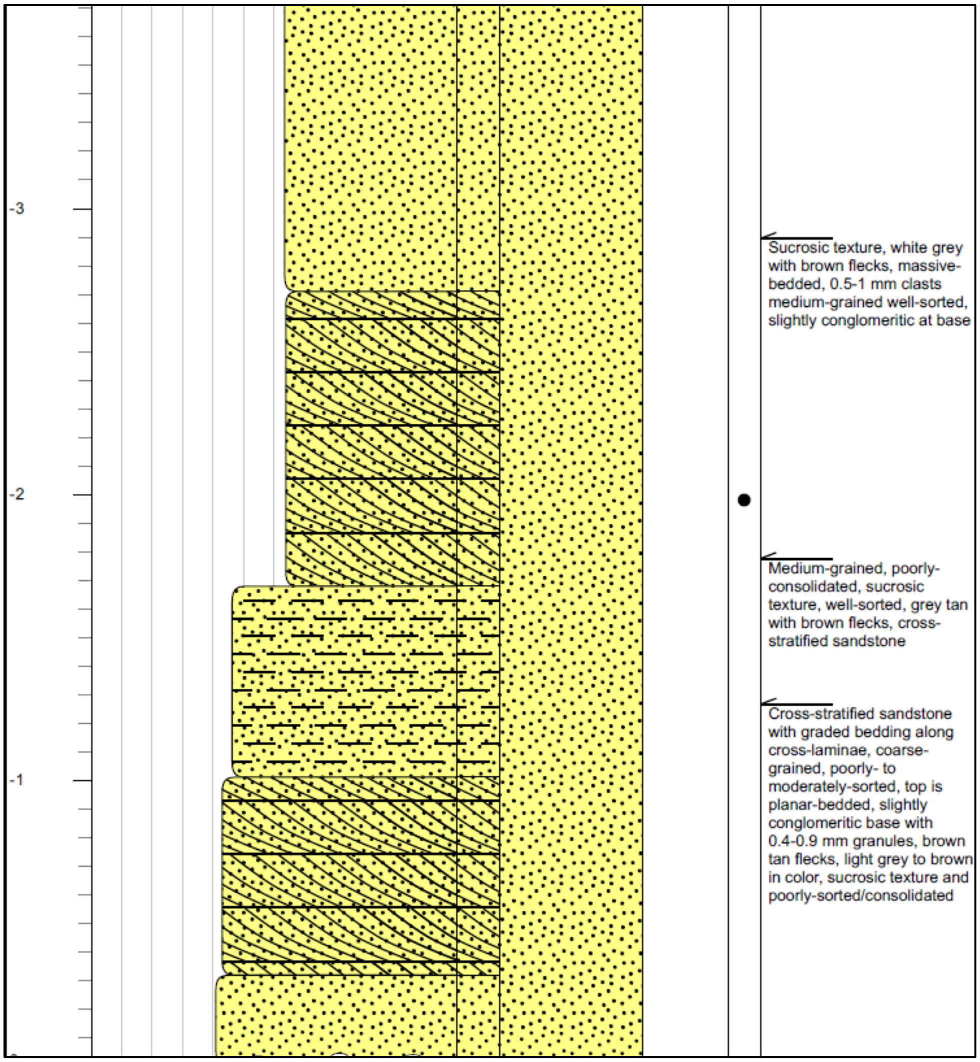

Figure 1. Detailed measured section created in EasyCore. Sample locations for thin-section petrography and porosity/permeability measurements are listed.

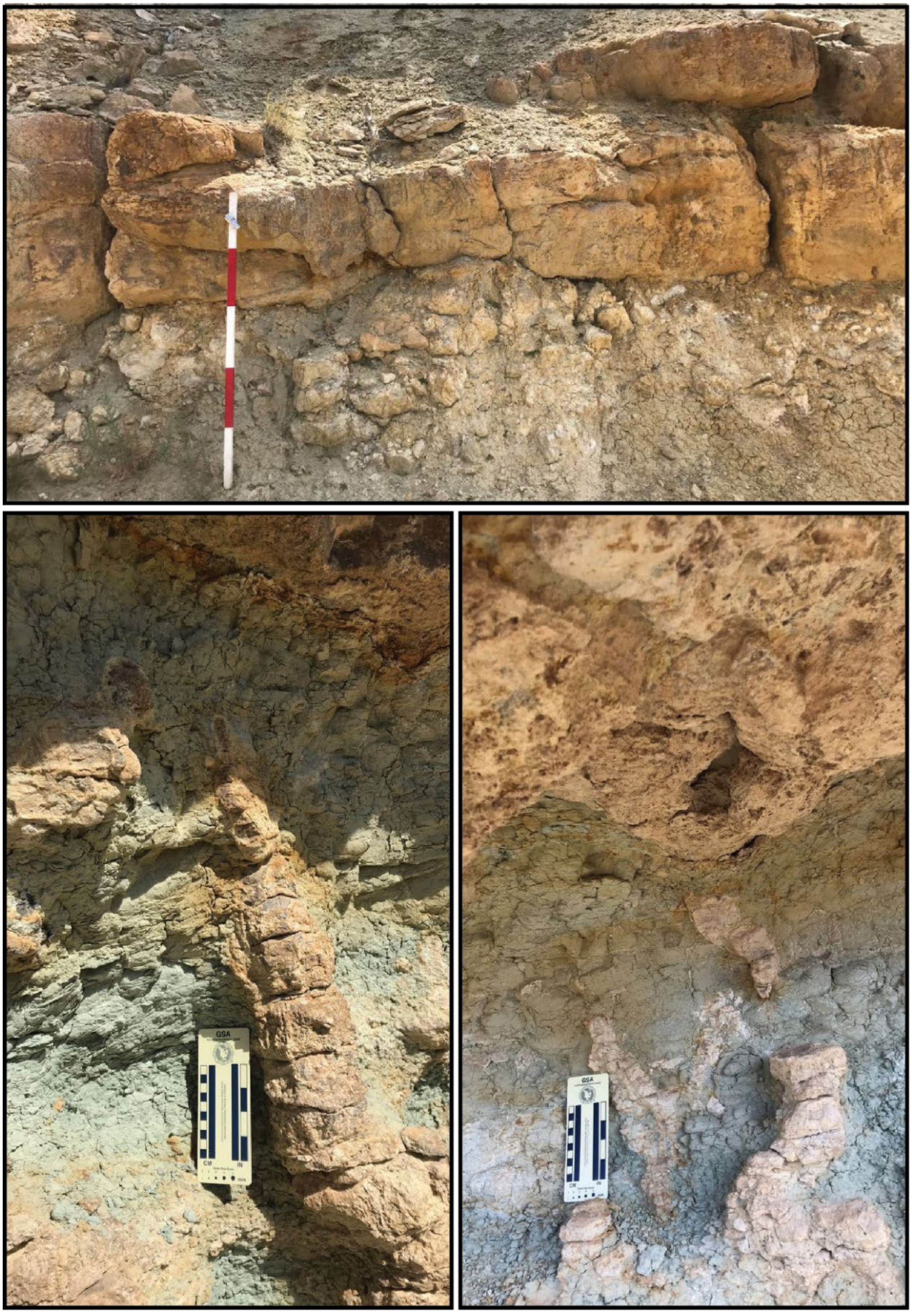
GSA
GSA

Figure 2. Characteristics of the calcareous lithologies of the Burro Canyon Formation. Top image shows a silty/sandy (impure) limestone. The bottom two images show calcareous columnar features that connect to the porous limestone above. These features resemble tufa-like deposits or could possibly be roots or burrows.

APPENDIX B: THIN-SECTION PETROGRAPHY

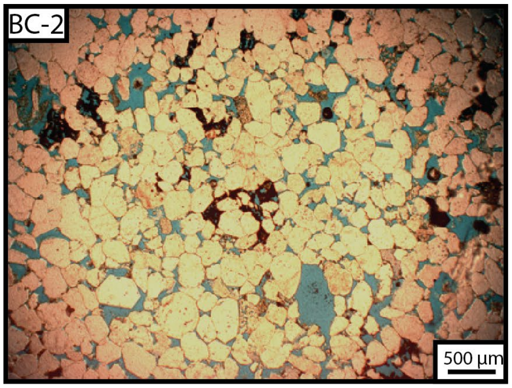

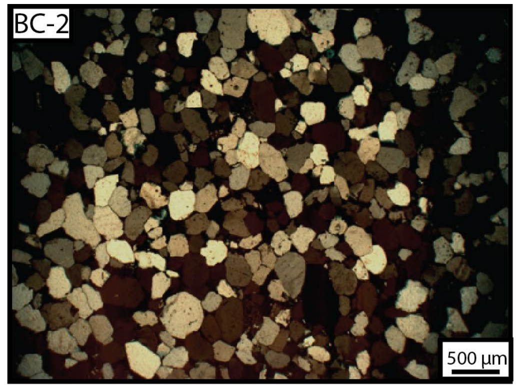

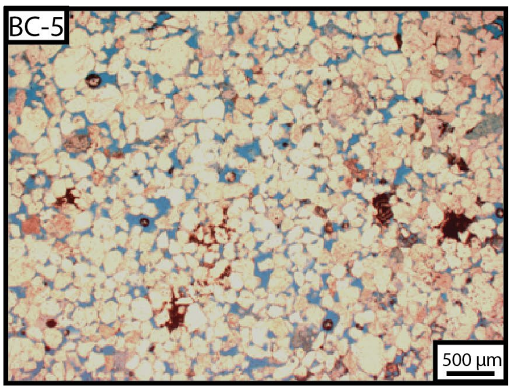

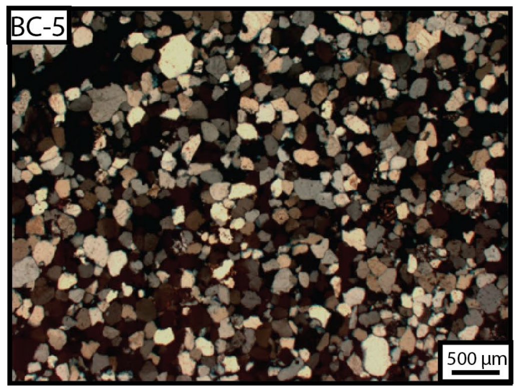

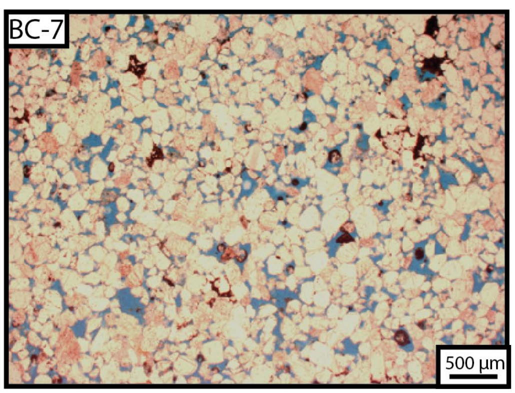

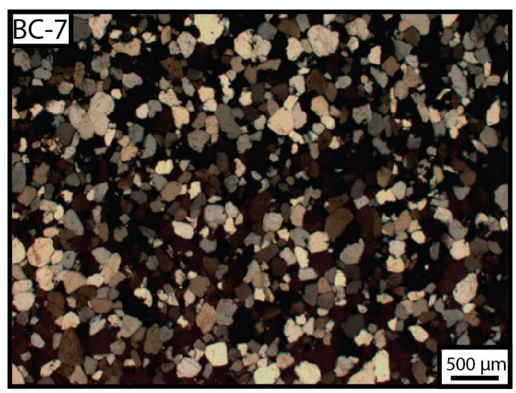

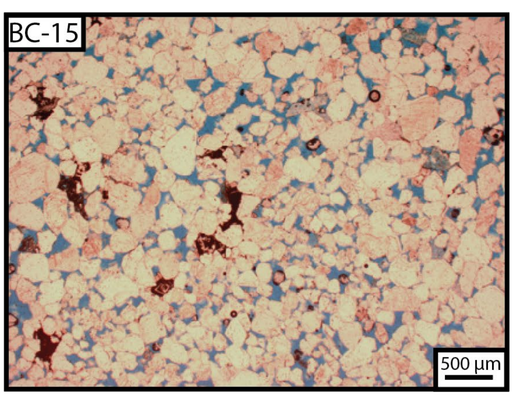

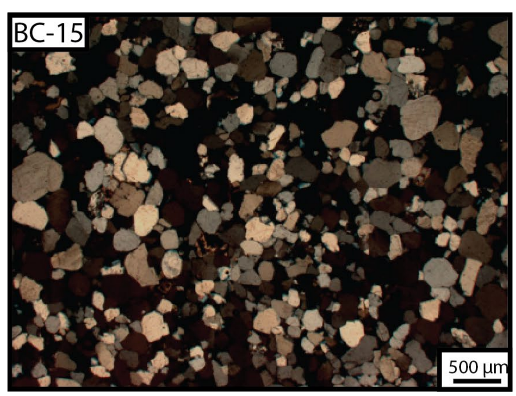

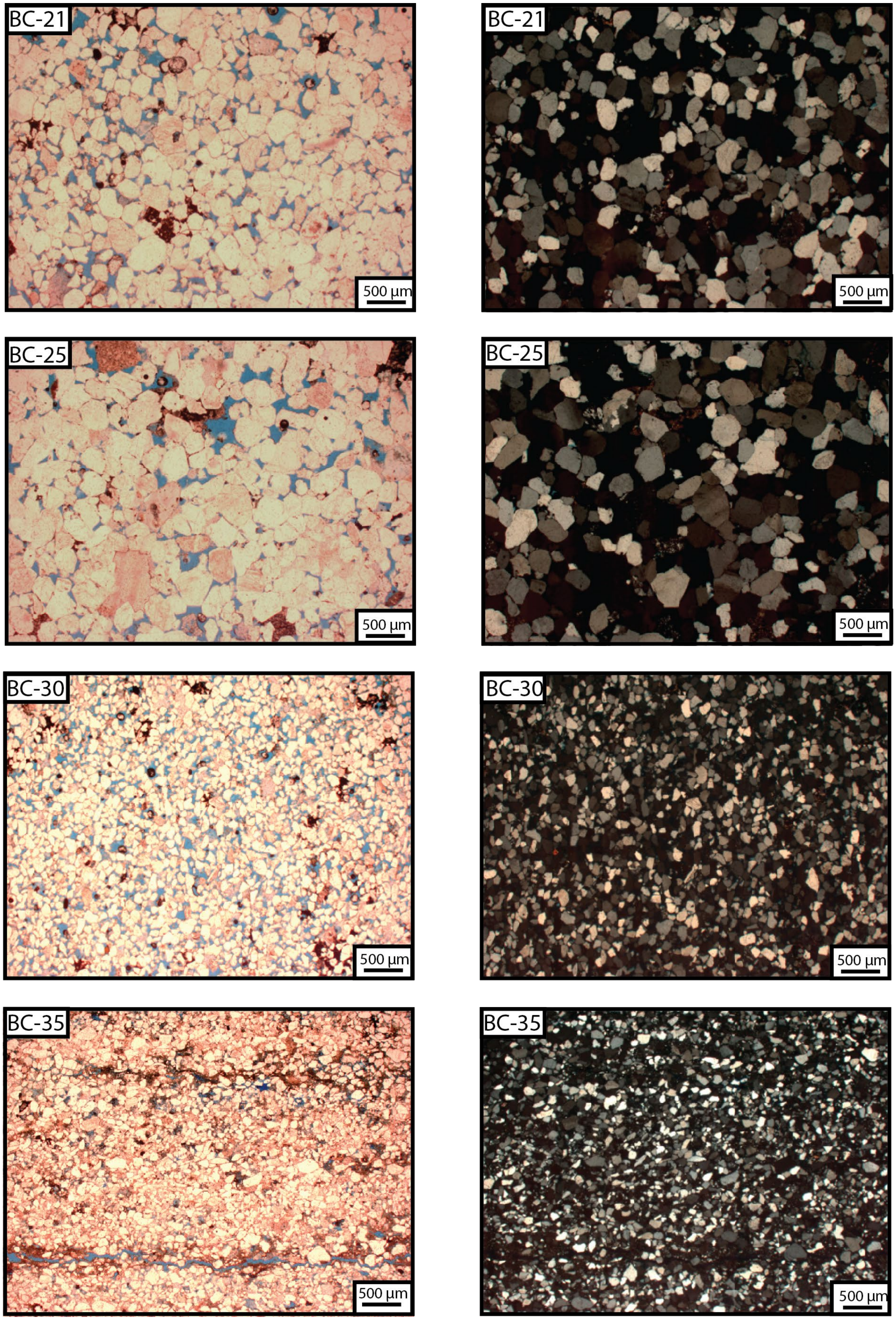
BC-21
500 µm
BC-21
500 µm
BC-25
500 µm
BC-25
500 µm
BC-30
500 µm
BC-30
500 µm
BC-35
500 µm
BC-35
500 µm

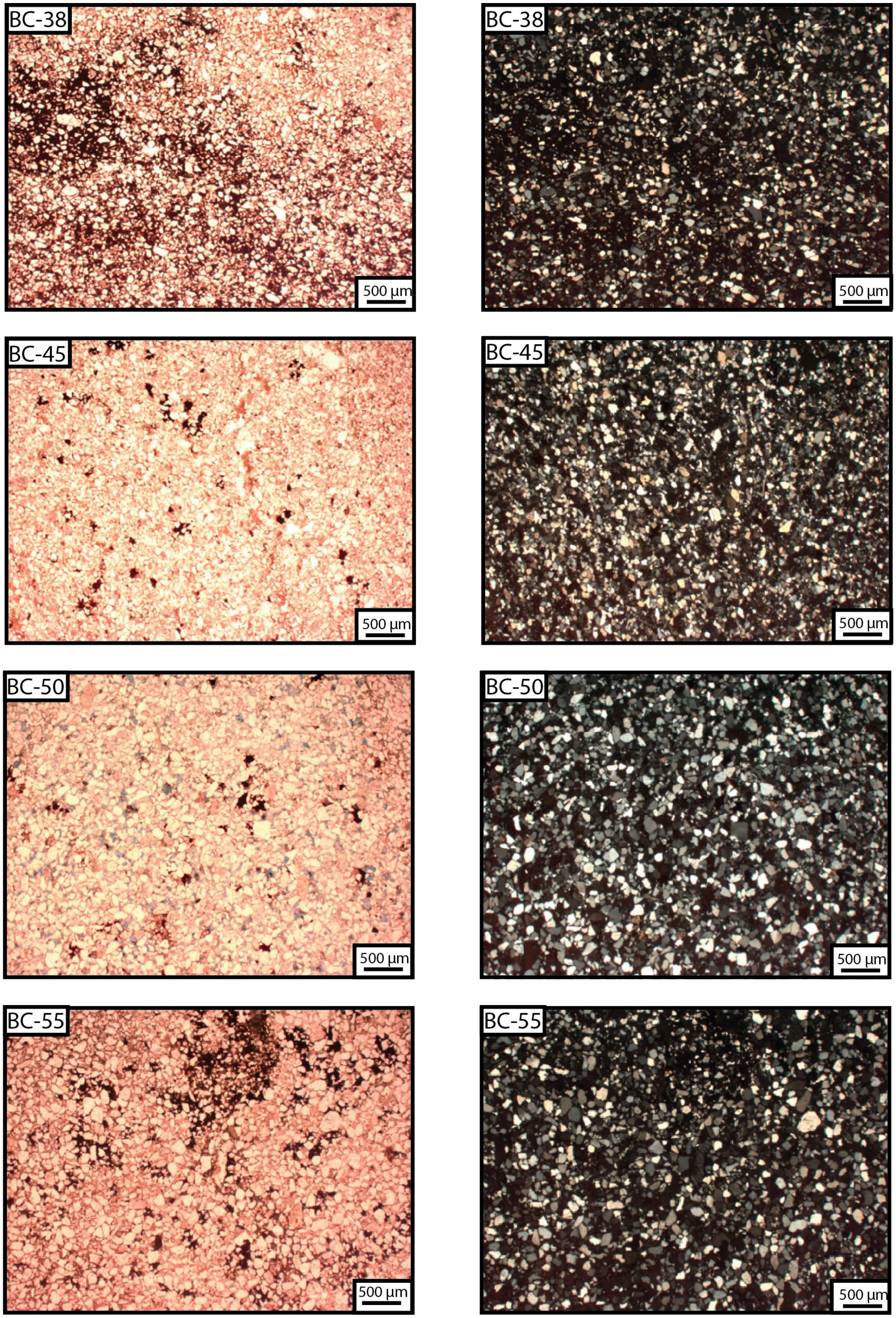
BC-38
500 µm
BC-38
500 µm
BC-45
500 µm
BC-45
500 µm
BC-50
500 µm
BC-50
500 µm
BC-55
500 µm
BC-55
500 µm

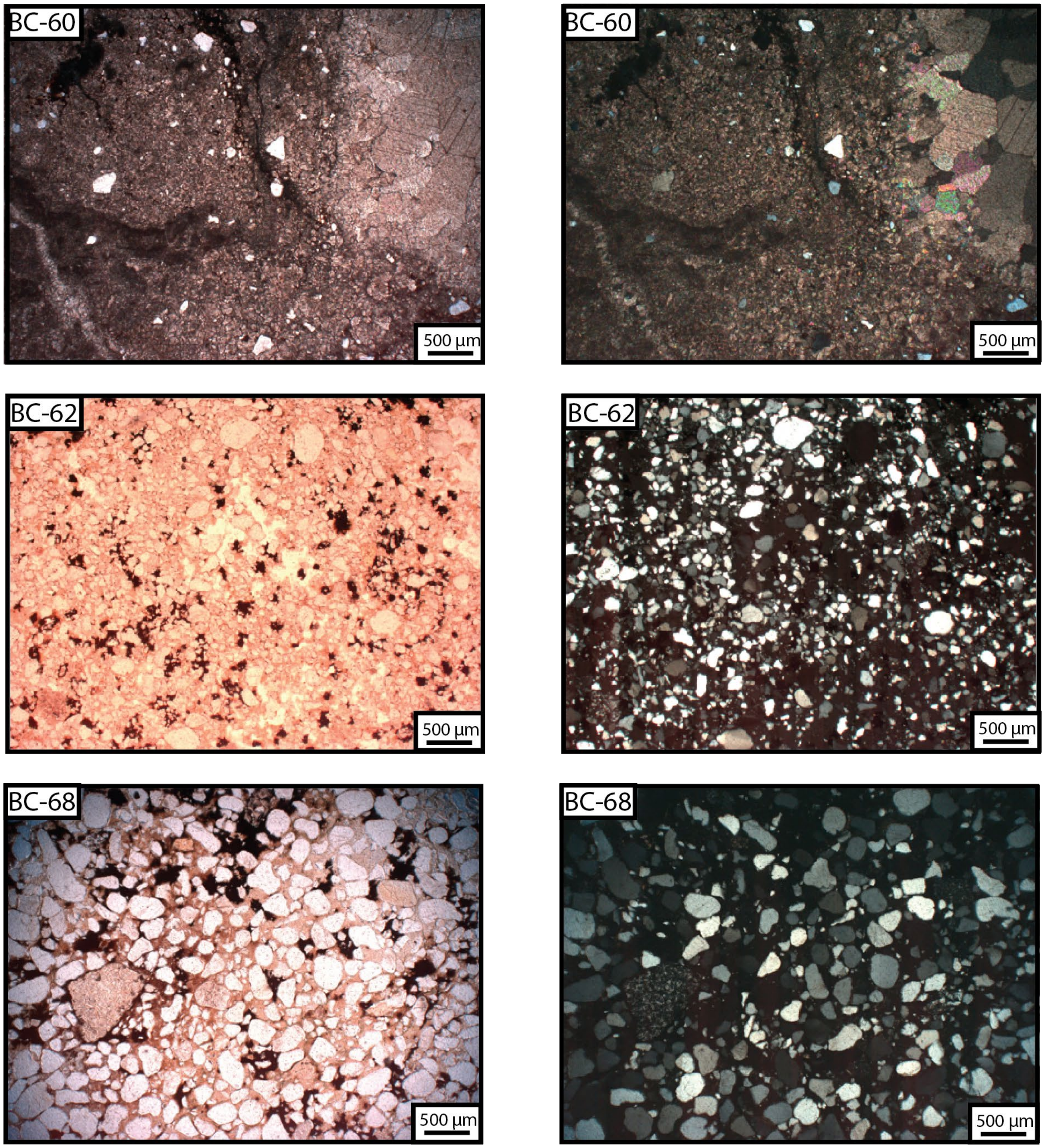

Figure 1. Thin-section photomicrographs of the 15 samples of the Burro Canyon Formation at Ninemile Hill ordered stratigraphically. Plane-polarized photomicrographs are on the left and the equivalent photomicrograph in cross-polarized light is on the right.

APPENDIX C: CHEMOFACIES CLUSTERING

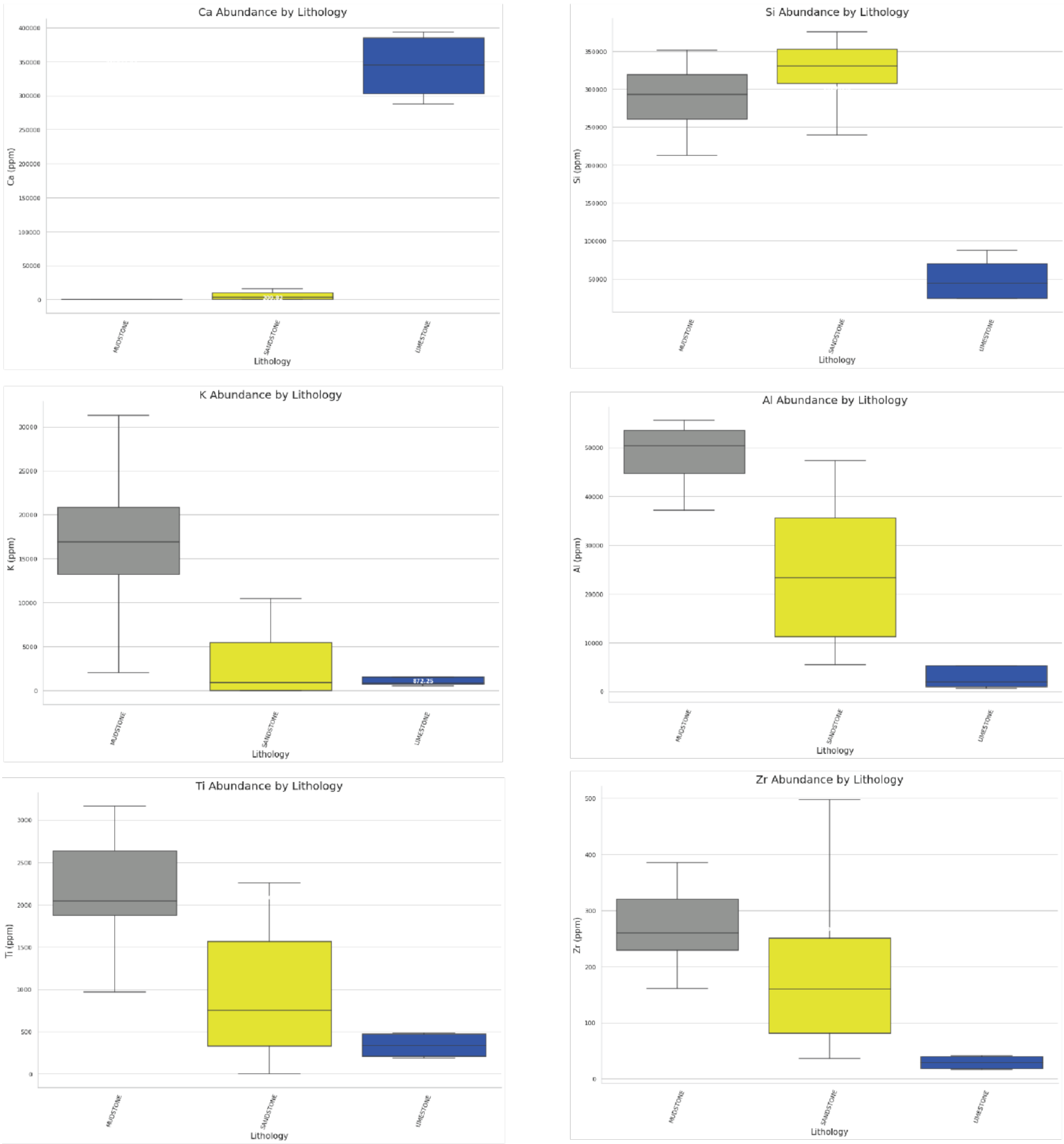

Figure 1. Box and whisker plots showing the proportion of the elemental abundances of Ca, Si, K, Al, Ti, and Zr that each lithology contains. Grey is mudstone, blue is limestone, and yellow is sandstone. The box and whisker plots show the minimum, first quartile, median, third quartile, and maximum of each lithology.

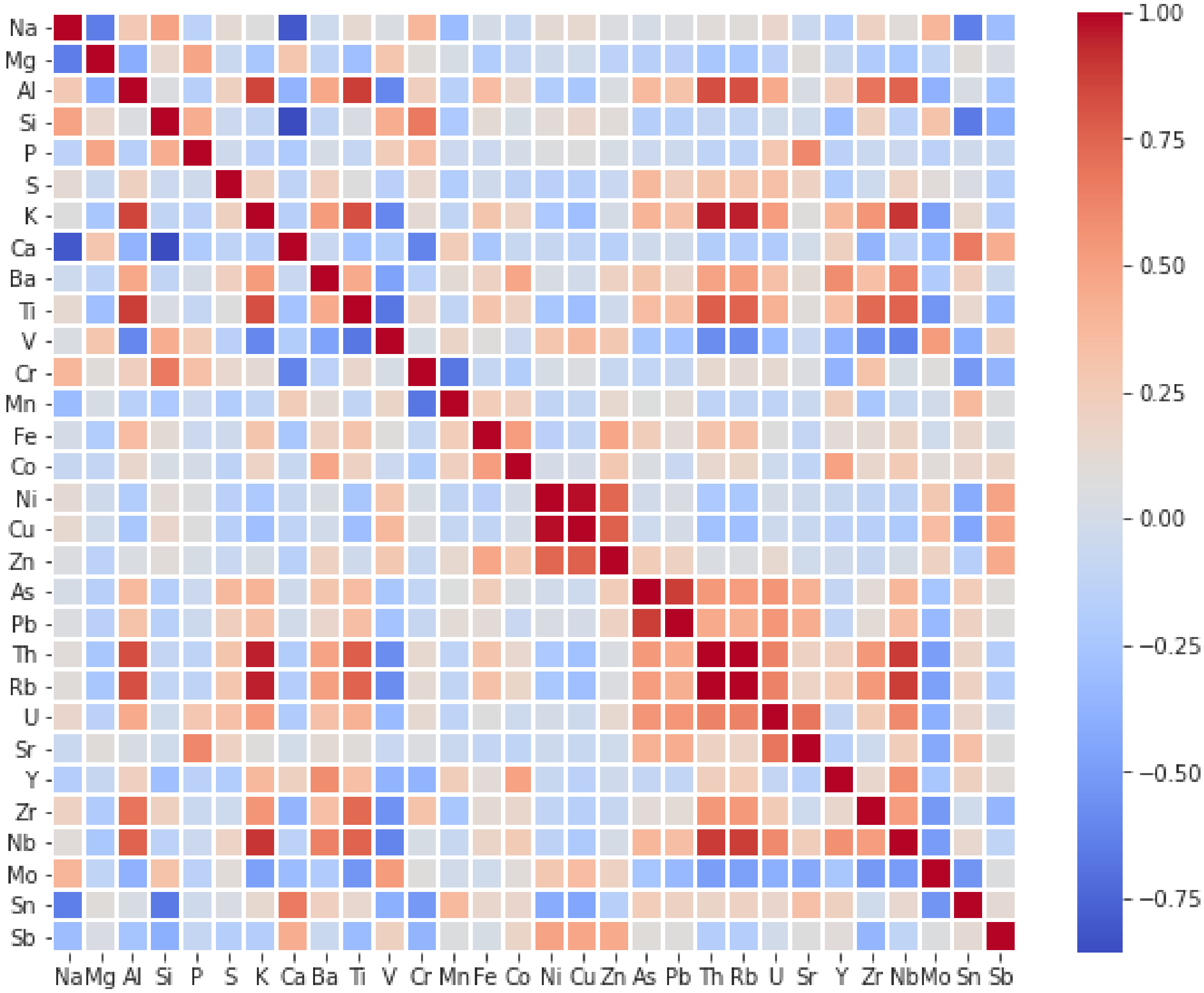

Figure 2. Correlation matrix or heat map of the thirty major and trace elements measured in this study. Red indicates a strong positive relationship. Blue indicates a strong negative relationship. The legend is the scale bar on the right of the heat map.

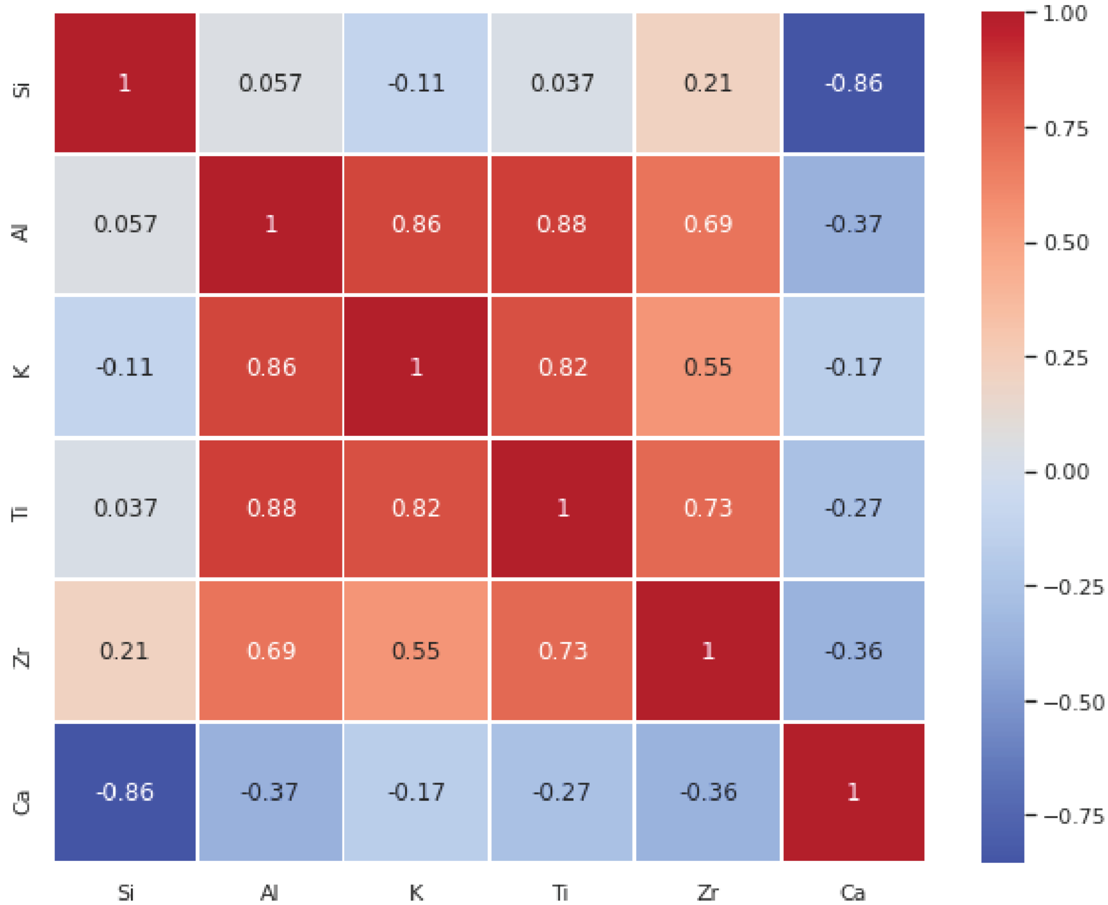

Figure 3. Correlation matrix or heat map of the six main indicator elements with their respective correlation coefficients. Red indicates a strong positive relationship. Blue indicates a strong negative relationship. Calcium (Ca) is shown to have a negative relationship between the elements Si, Al, K, Ti, and Zr. Zr, Ti, Al, and K all have a slight positive to positive corelation.

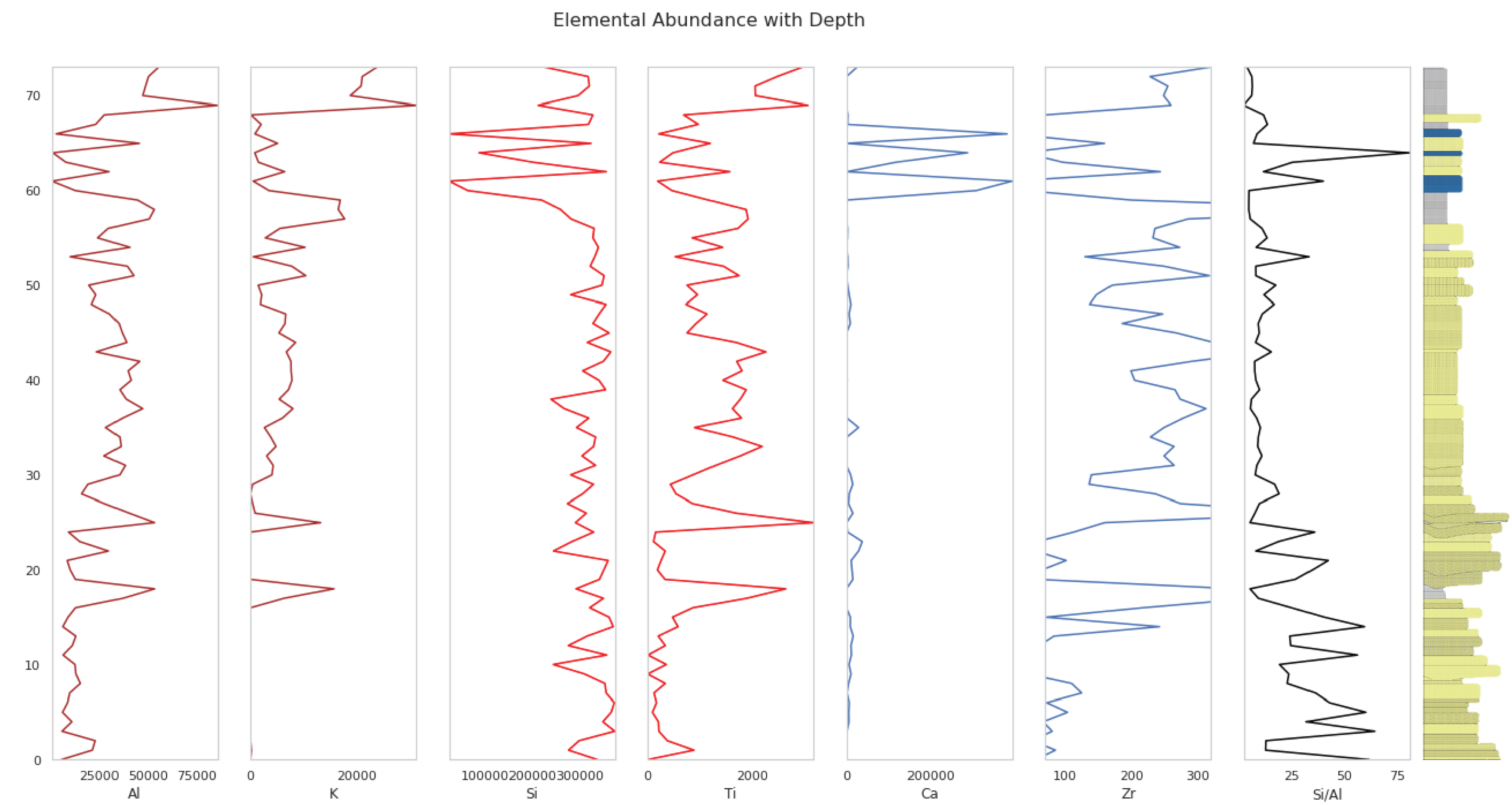

Figure 4. Elemental abundances (ppm) with depth of the six main indicator elements aluminum (Al), potassium (K), silicon (Si), titanium (Ti), calcium (Ca), zirconium (Zr), and Si/Al ratio. Measured section on right.

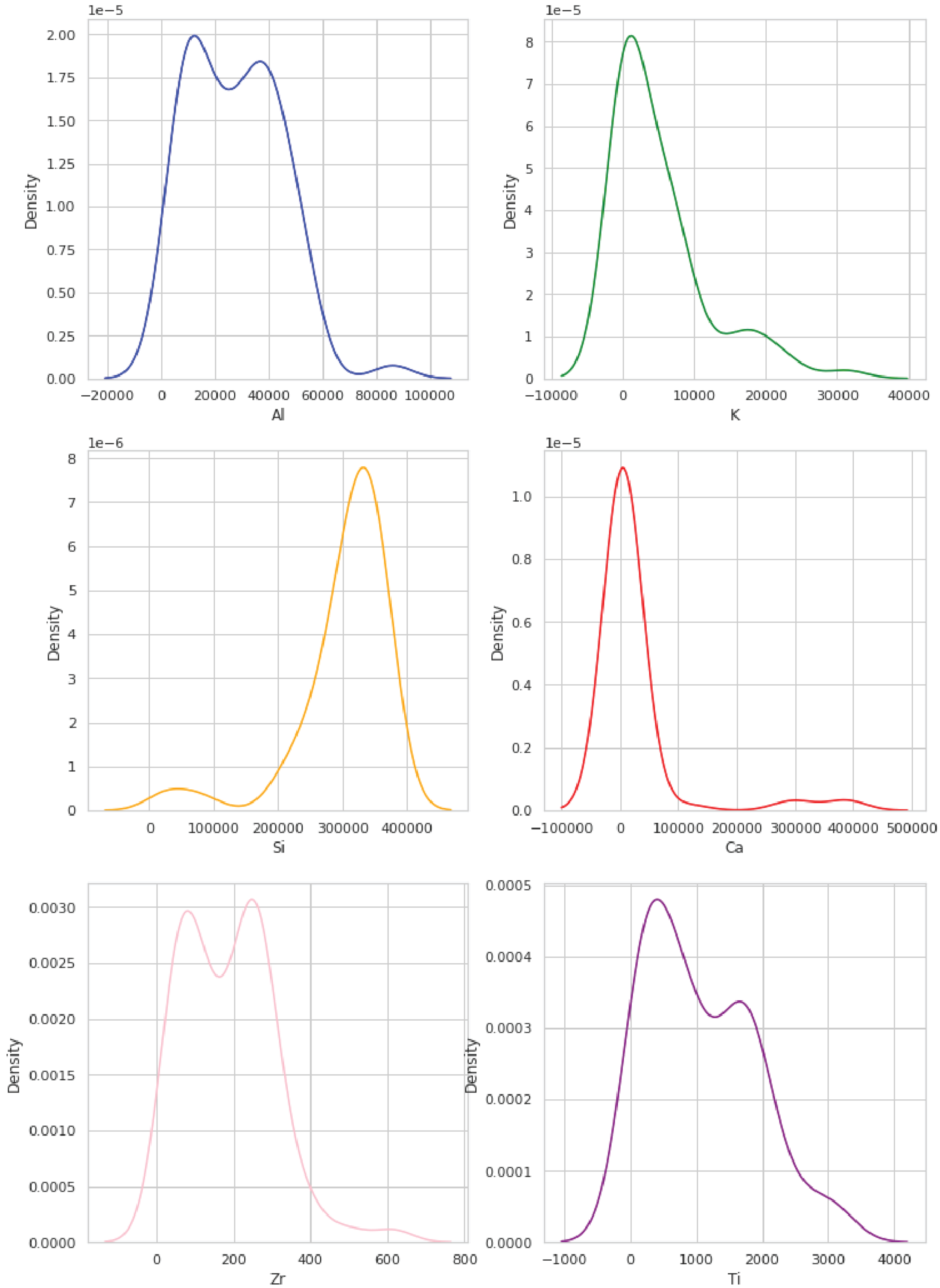

Figure 5. Individual data distributions of Al, K, Si, Ca, Zr, and Ti before scaling.

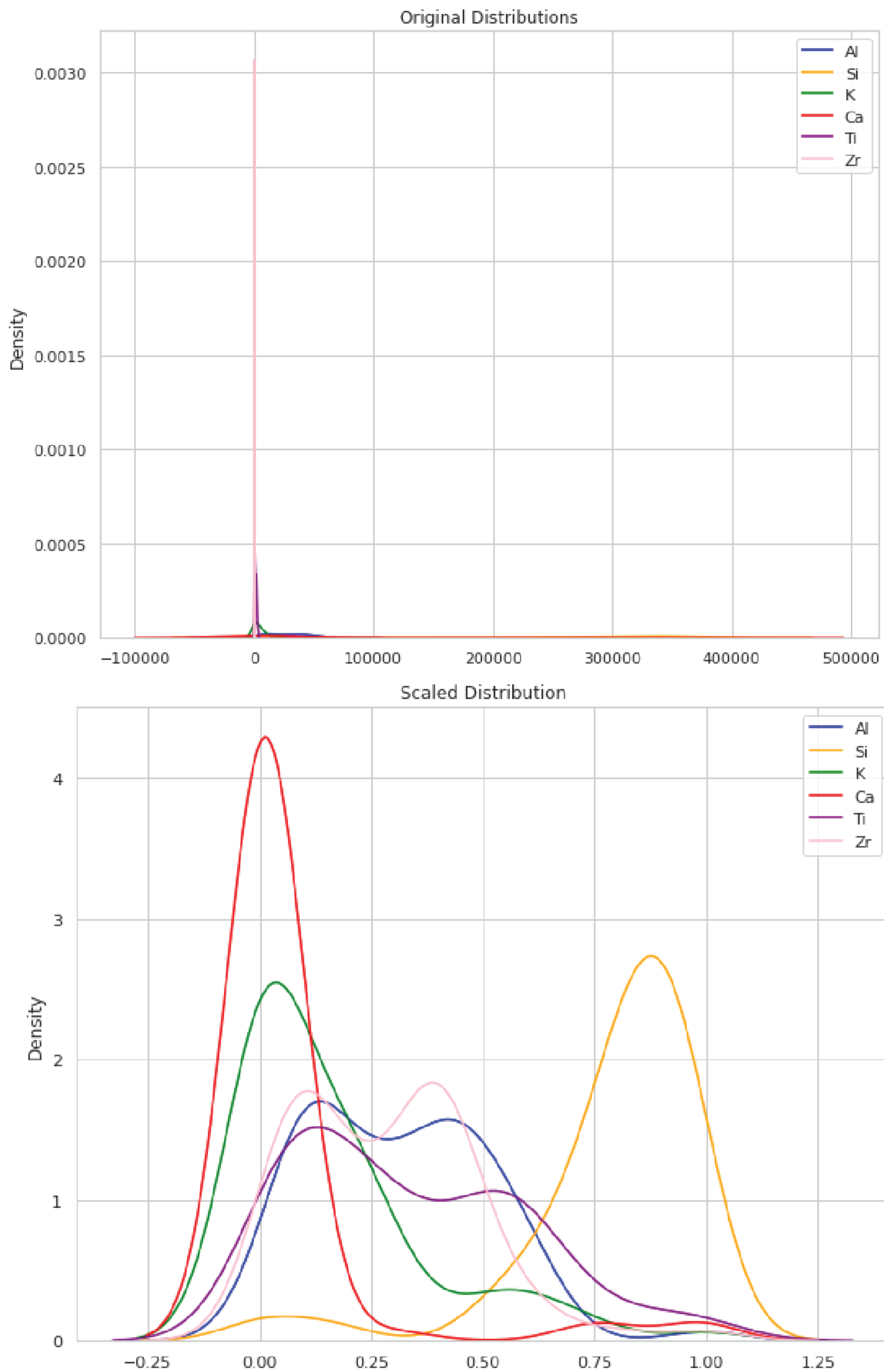

Figure 6. Original distributions of the elemental data (top figure) and the scaled distributions (bottom figure). Data was scaled using a minmax scalar.

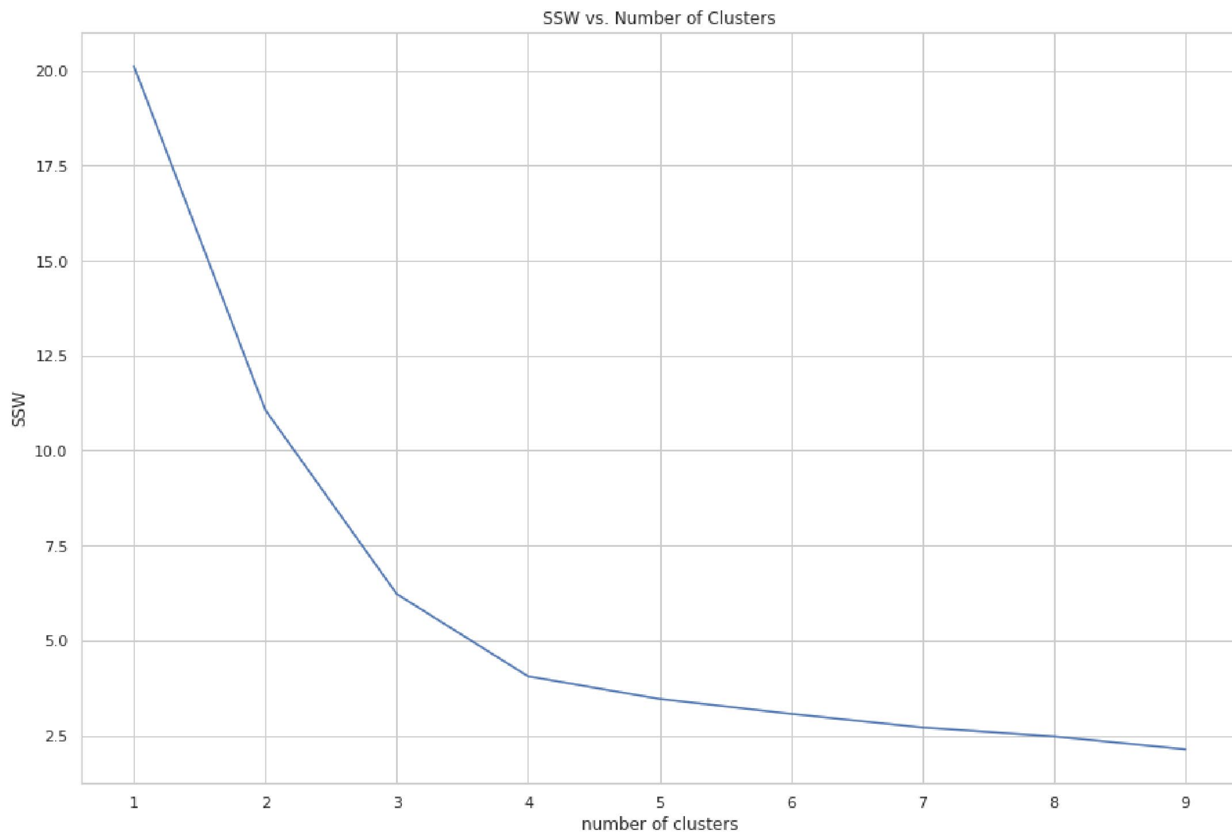

Figure 7. Elbow plot showing the sum of squares within (SSW) and the optimal number of clusters. The plot indicates a cluster of two, three, or four to be the optiaml number of clusters within the data. Both three and four clusters were chosen to cluster the data given the plot and the domain knowledge about the types of lithologies that exist in outcrop in Ninemile Hill.

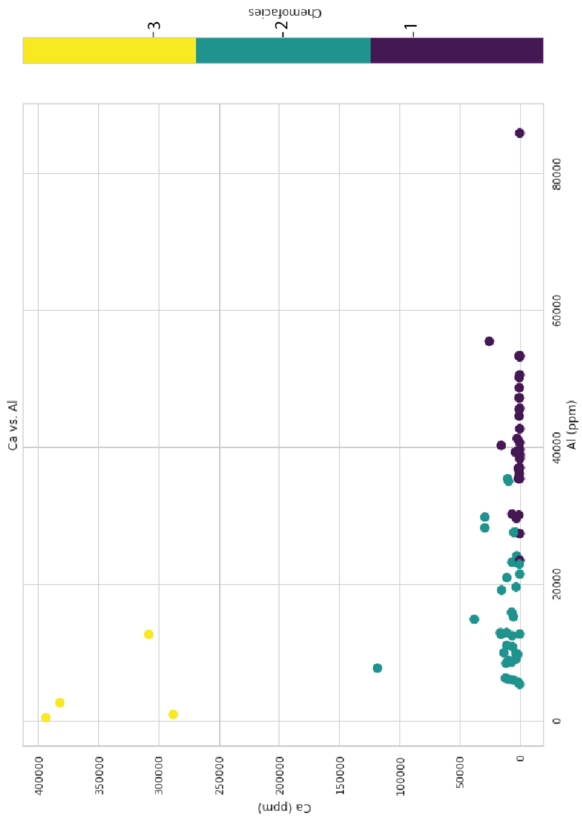
Ca vs. Al
Ca (ppm)
Al (ppm)
Chemofacies
1
2
3

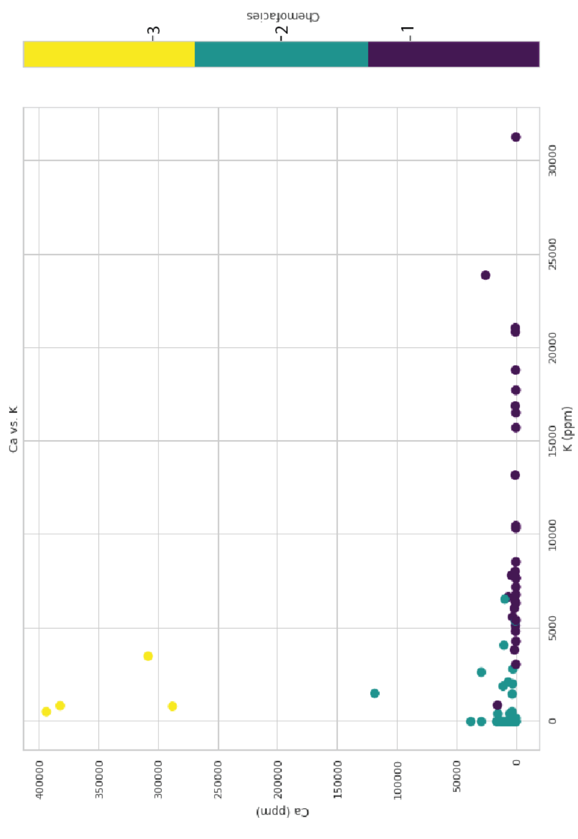
Ca vs. K
Ca (ppm)
K (ppm)
Chemofacies
1
2
3

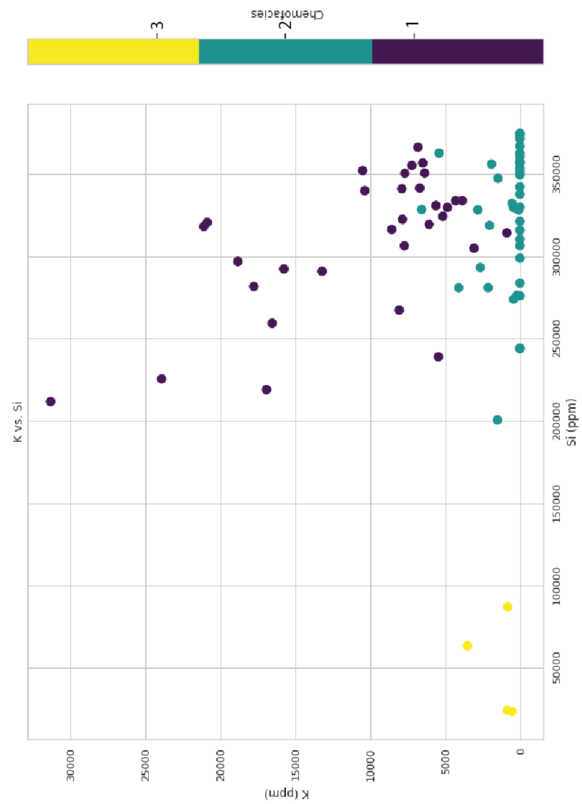
K vs. Si
K (ppm)
Si (ppm)
Chemofacies
1
2
3

Figure 8. Cross-plots of Ca, K, Al, and Si showing the chemofacies clustering results of k-means clustering using three clusters. It appears that k-means is clustering the XRF data into a higher Ca content facies, a higher Al and K content facies, and a higher Si content facies with low K.

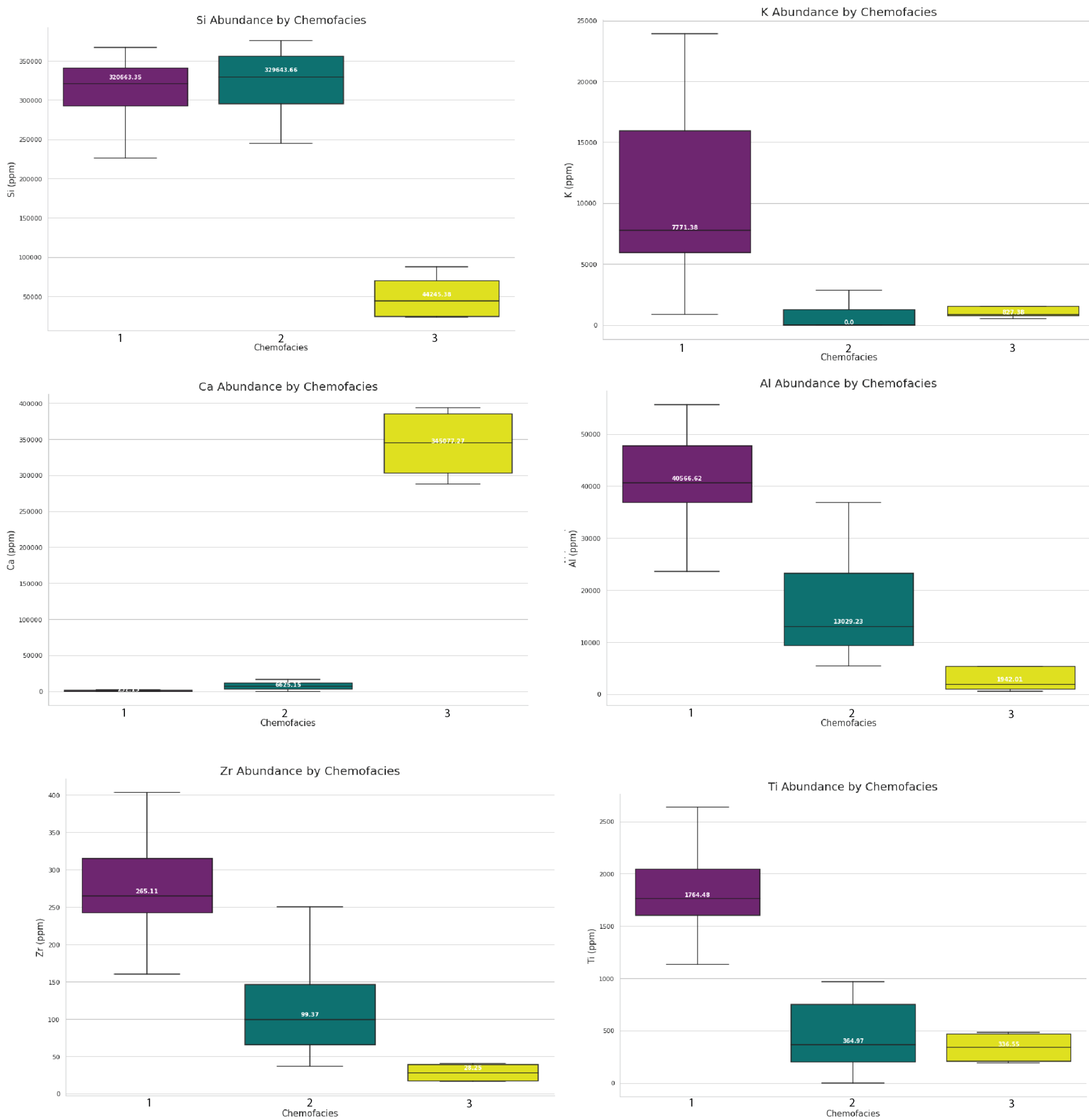

Figure 9. Box and whisker plots showing the distributions (in ppm) of the six main indicator elements Si, Ca, K, Al, Zr, and Ti color-coded by k-means-clustered chemofacies. Si abundance varies slightly between chemofacies cluster one and two but is significantly lower in chemofacies three. K abundance varies slightly between chemofacies two and three but is higher in chemofacies one. Ca abundance is significantly high for chemofacies cluster three. Al abundance is relatively higher in chemofacies one, moderately high in chemofacies cluster two, and low for chemofacies three. Chemofacies one contains the highest proportion of Ti and Zr and follows the trend of Al.

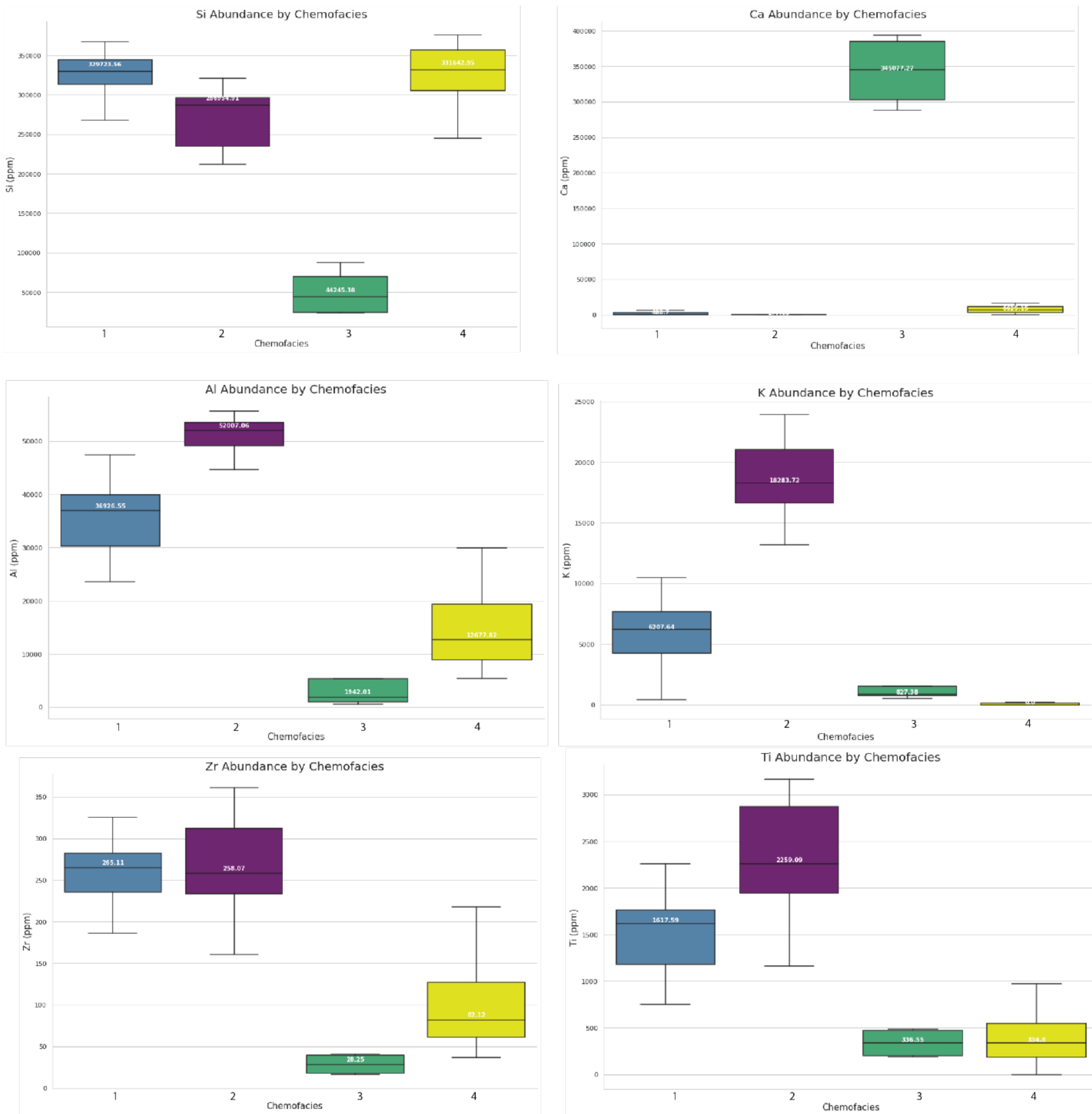

Figure 10. Box and whisker plots showing the distributions (in ppm) of the six elements used for chemofacies clustering Si, Ca, K, Al, Zr, and Ti color-coded by k-means clusters. Si abundance varies slightly between chemofacies cluster one, two, and four but is significantly lower in chemofacies three. Chemofacies one contains high proportions of Si but lower Al and K than chemofacies two. Chemofacies two contains high proportions of both Al and K with relatively lower Si content. Chemofacies three contains the highest proportion of Ca. Chemofacies two contains the highest proportion of Zr and Ti, followed closely by chemofacies one.

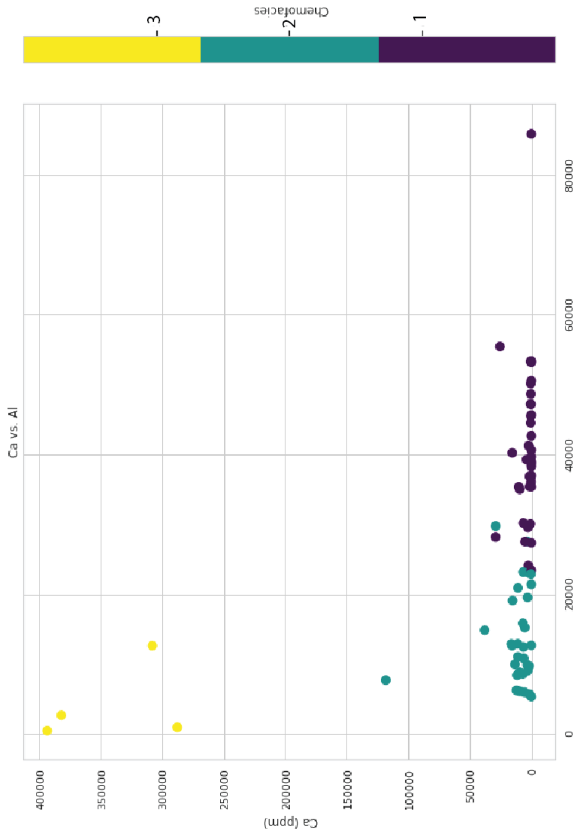
Ca vs. Al
Al (ppm)
Ca (ppm)
Chemofacies
1
2
3

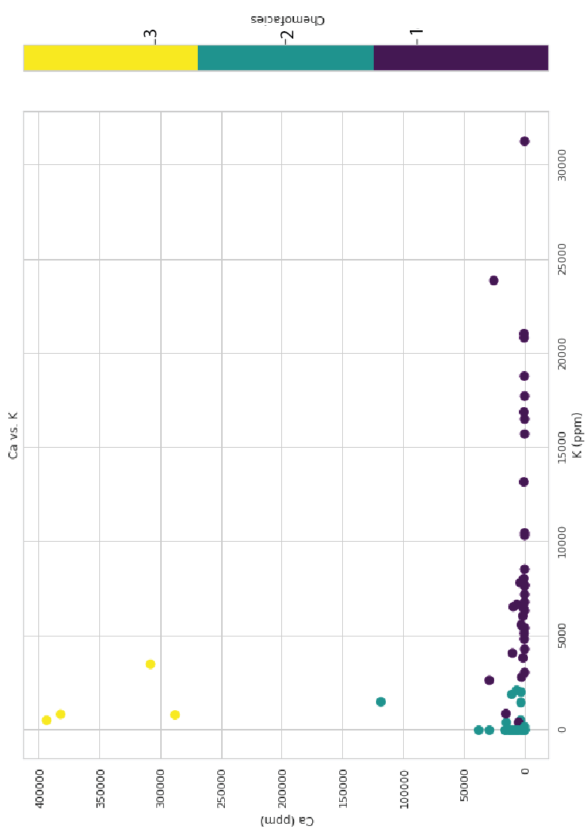
Ca vs. K
K (ppm)
Ca (ppm)
Chemofacies
1
2
3

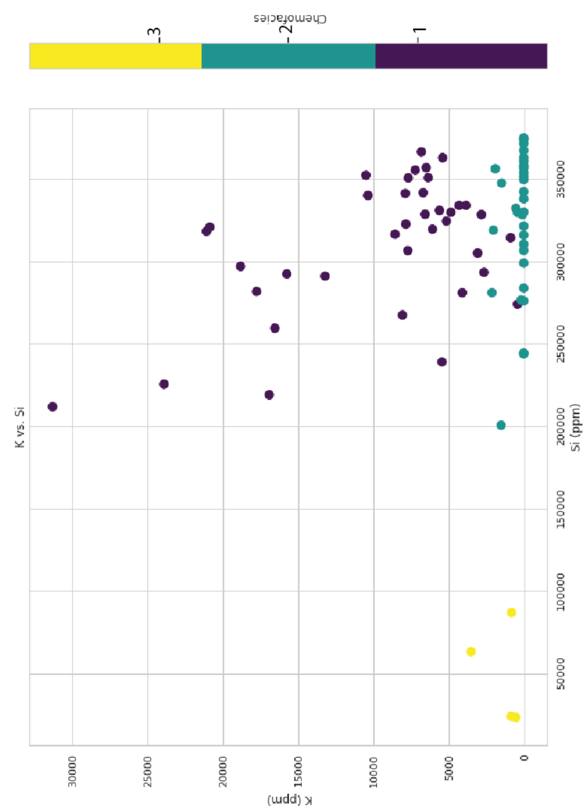
K vs. Si
Si (ppm)
K (ppm)
Chemofacies
1
2
3

Figure 11. Cross-plots of Ca, K, Al, and Si showing the chemofacies clustering results of hierarchical clustering for three clusters. It appears that hierarchical clustering is clustering the XRF data into a higher Ca content facies, a higher Al and K content facies, and a higher Si content facies with low K.

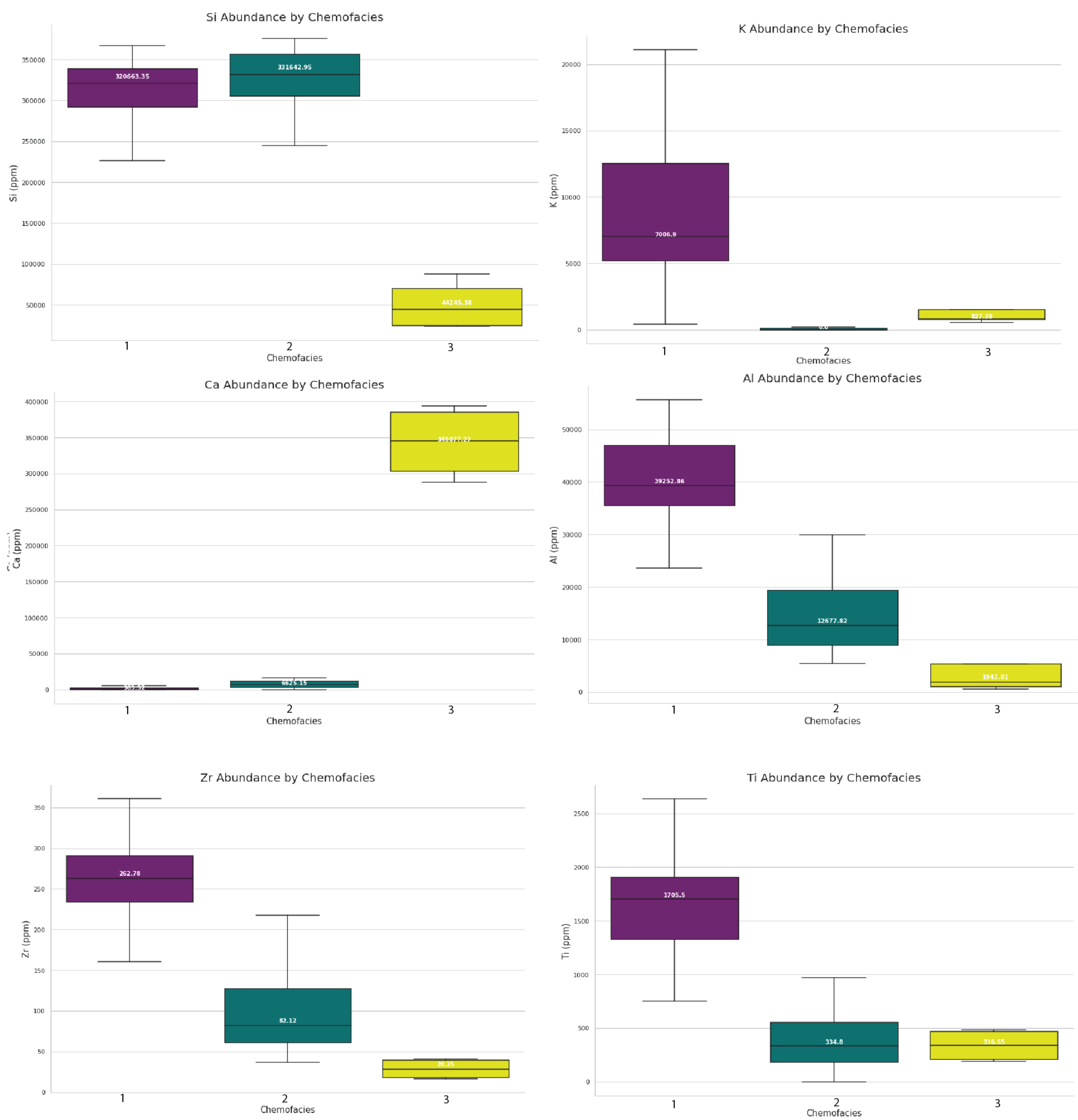

Figure 12. Box and whisker plots showing the distributions (in ppm) of the six main indicator elements Si, Ca, K, Al, Zr, and Ti color-coded by hierarchical-clustered chemofacies. Si abundance varies slightly between chemofacies cluster one and two but is significantly lower in chemofacies three. K abundance varies slightly between chemofacies two and three but is higher in chemofacies one. Ca abundance is significantly high for chemofacies cluster three. Al abundance is relatively higher in chemofacies one, moderately high in chemofacies cluster two, and low for chemofacies three. Chemofacies one contains the highest proportion of Ti and Zr and follows the same trend as Al.

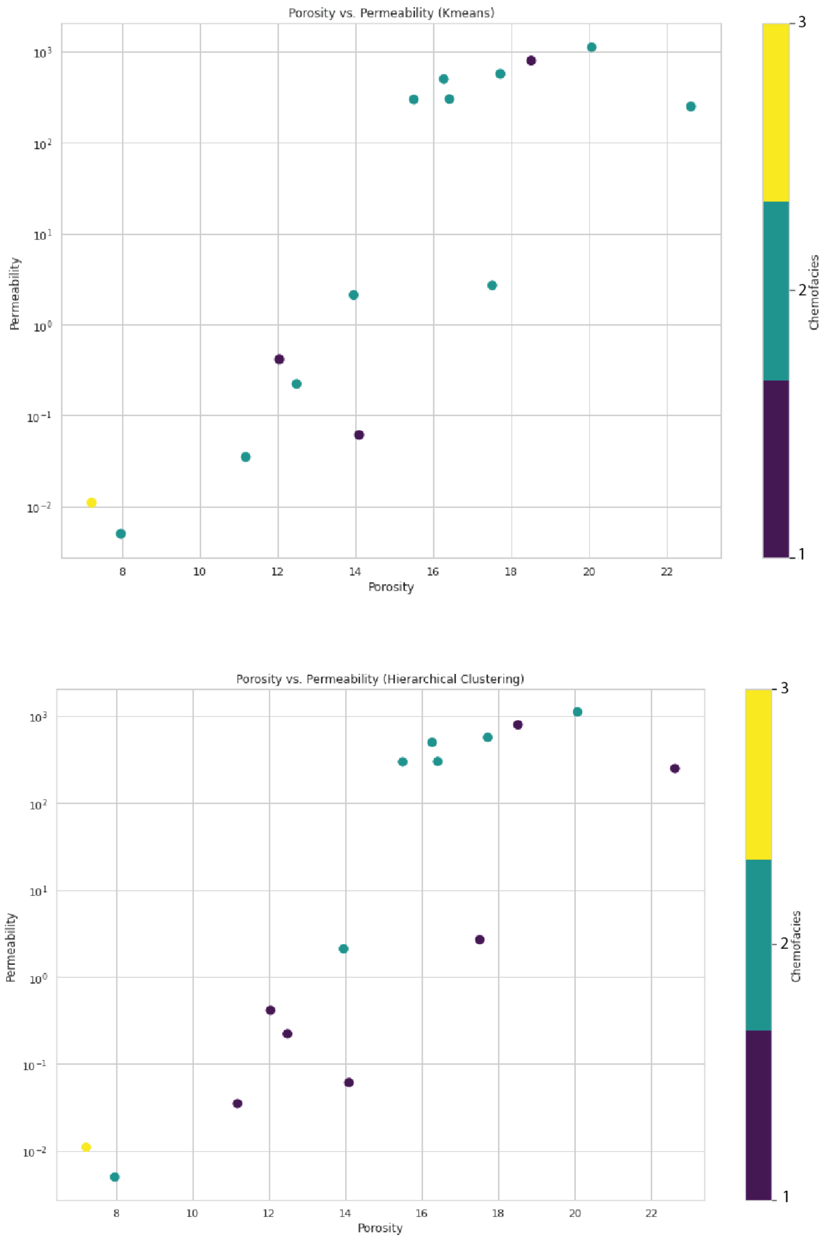

Figure 13. Cross-plots of porosity and permeability color-coded to the clustering results of both k-means (top) and hierarchical clustering (bottom) results using three clusters. Shown are the differences in clustering between the petrophysical data, primarily between chemofacies cluster one and two. A stronger relationship between the data is illuminated by the hierarchical clustering results.

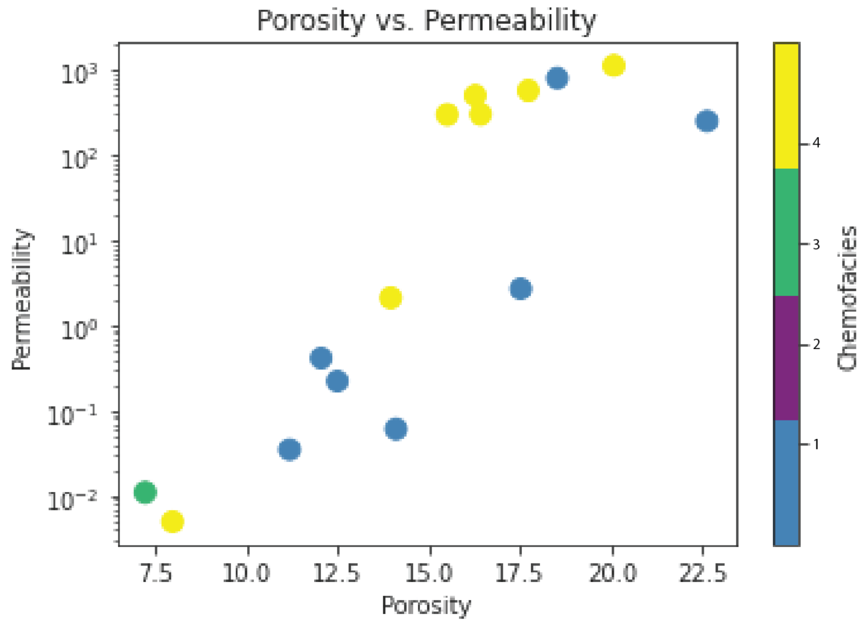

Figure 14. Cross-plot of porosity and permeability color-coded to the clustering results of k-means clustering with four clusters. Chemofacies four is mostly associated with overall higher porosities and permeabilities, whereas chemofacies one and three correlate with lower permeabilities and porosities.

Depth	Na	Mg	Al	Si	P	S	K	Ca	Ba	Ti	V	Cr	Mn	Fe	Co	Ni	Cu	Zn	As	Pb	Th	Rb	U	Sr	Y	Zr	Nb	Mo	Sn	Sb
73	7787.98	0	55577.4	226123	154.977	1825.76	23898	25379	2603.44	2954.25	0	0	1617.11	19260.7	29.8159	33.8934	27.7263	20.806	2.08274	9.6864	9.02396	110.918	11.2347	185.981	95.5632	320.742	18.722	3.2082	1.97082	6.23332
72	7320.59	2673.81	50301.3	318780	168.65	1724.07	21079.8	419.632	0	2467.65	139.671	122.912	281.467	14462.4	7.12371	22.4696	105.053	24.5912	2.21024	9.98675	9.82074	120.148	7.02645	168.048	29.1304	228.616	10.8887	13.0433	1.74229	1.75631
71	7475.56	2398.98	48793.9	321282	142.32	1739.6	20860.4	345.489	753.368	2046.17	62.6541	135.59	285.127	15508.1	7.47466	23.2975	136.17	22.834	1.59979	10.349	10.3145	127.384	16.7442	154.053	47.1918	255.655	14.6821	7.901	1.62611	1.45364
70	8068.47	32.1277	47331.4	297535	91.409	2075.28	18816	209.815	804.343	2050.53	33.4324	118.757	277.372	14379.1	3.7407	29.3785	168.143	24.7334	1.79756	10.0212	9.15593	111.557	7.50598	144.654	37.1237	249.215	11.2477	10.7692	1.89309	4.99468
69	7003.47	1211.06	85994.9	212387	178.639	9585.32	31302.4	0	1961.41	3059.1	0	107.459	248.231	25644.1	6.69621	26.1771	48.3297	60.1302	43.289	24.0493	16.8727	229.355	45.2756	1406.98	16.4304	260.483	16.8631	0	2.20401	4.58942
68	7142.85	1475.22	27683.5	328879	145.327	1720.42	86.0097	3469.84	0	687.433	254.905	13.3107	2157.11	25419.5	8.14675	8.80048	29.6837	28.5526	2.5557	8.25863	3.20414	17.0322	3.80351	88.4455	19.9265	69.9299	4.83632	31.3645	1.89592	0
67	6963.55	888.799	23258.2	319448	168.336	2171.38	2021.29	2812.79	0	969.18	247.624	30.9946	1800.76	41111.2	5.7879	5.4883	68.5366	68.8119	3.77397	10.5409	3.14552	21.5818	0	83.7665	24.5624	68.2806	3.55739	20.7865	1.99438	4.48933
66	2140.71	6523.9	2798.63	24652.1	0	2569.22	841.201	382004	0	209.932	68.093	0	744.54	0	4.0359	29.3585	26.8632	0	0.78408	8.72675	2.59107	9.89288	5.1783	353.041	36.656	16.7349	6.15624	0	2.46496	13.494
65	7148.6	1876.97	45629.9	324971	138.253	1931.02	5141.46	291.404	0	1198.49	184.563	103.015	426.879	33717.5	7.95692	18.5996	240.191	35.3711	2.05997	10.249	3.95263	32.6663	8.93005	83.871	21.9479	160.317	5.47527	16.9023	1.87549	7.93715
64	2679.89	3646.91	1085.38	87584.9	0	1390.16	813.557	287745	0	484.165	98.669	0	2912.41	0	4.10007	13.0104	23.0765	0	9.82112	17.2086	2.79495	10.5158	1.14403	202.293	26.7925	38.6653	4.32734	1.36052	2.44082	3.7604
63	7418.99	0	7849.11	201186	71.751	1875.26	1504.27	118352	0	228.69	95.9361	79.2961	479.017	967.113	2.17969	11.9911	12.2872	0	0.3984	9.98693	3.57413	25.6121	5.61442	420.17	21.4933	96.7013	4.91582	4.77701	1.96946	0
62	6403.52	4203.51	30191.8	357379	237.114	2015.38	6480.14	760.365	403.497	1563.85	131.237	80.5836	812.106	29224.2	7.51317	14.6291	91.9281	11.9664	1.39681	9.20086	4.89752	35.7466	0	115.854	28.0667	244.348	7.30136	10.4388	1.73339	1.63796
61	2256.62	5761.15	600.395	23990.2	0	1381.18	521.582	393561	0	189.635	70.7955	1.9448	295.451	4684.49	2.53682	21.2826	23.4875	0	0.87753	10.7198	2.46739	0.8544	0	160.949	25.2465	17.8282	3.84035	0	2.34254	15.3846
60	3095.32	2896.96	12774.7	63838.6	0	2450.38	3502.39	308151	0	463.168	68.3773	20.7181	273.967	6043.41	2.34274	20.799	25.1879	0	0.90145	8.59457	3.6525	23.5963	0	257.182	50.0267	40.8763	8.43802	0	2.25484	9.16508
59	9678.51	0	44663.3	219638	0	2633.54	16911.5	484.079	0	1160.23	51.3256	83.5571	226.219	15501.6	1.84436	16.4362	14.7153	0	1.37372	11.0601	9.29433	114.472	16.1805	98.4887	17.0585	199.907	9.552	19.4665	1.64047	0
58	8252.37	0	53314.9	260020	0	2792.35	16536.4	24.6585	0	1873.14	45.8864	103.195	273.982	10077.1	3.20514	60.4564	428.001	26.0981	1.3272	9.81357	7.5752	83.3917	10.5823	80.3552	24.569	614.977	9.58517	0	1.67561	5.94365
57	8274.34	0	50699.3	282304	5.30211	2482.79	17751.5	0	0	1912.75	83.8983	92.4278	253.001	13828.2	3.66521	59.2101	497.807	26.6255	1.94544	11.2521	9.09943	106.865	18.1357	151.679	18.5562	286.24	10.5329	8.83966	1.63215	2.97101
56	6569.76	2231.13	29712.1	331469	175.43	1773.83	5599.64	2795.47	0	1716.95	163.522	145.904	238.381	40047.2	9.60387	12.1779	80.6052	50.1483	3.09615	10.345	4.26686	32.6307	0	65.6322	26.3531	236.138	5.3731	6.18094	1.84673	2.54788
55	7211.87	1134.32	24230.3	328915	109.142	2036.7	2811.81	2454.08	0	851.967	173.122	94.6063	350.659	30668.6	35.2714	7.94097	13.134	24.6478	2.35203	8.55619	3.70384	29.5901	0	44.2584	24.9795	233.007	4.6017	34.9882	1.88589	8.90173
54	7353.79	2983.7	40769.3	340587	149.644	2456.07	10350.2	0	0	1425.44	119.516	144.78	314.29	7970.79	1.96088	21.9927	114.536	0	1.06613	7.87635	5.6974	61.388	12.218	38.0011	19.5369	273.735	6.77098	9.32027	1.66349	4.02945
53	7601.16	1377.73	10014.9	332812	121.916	2265	524.298	3206.56	0	525.234	234.127	53.7586	1120.94	32596.7	10.9725	26.8934	165.399	37.6983	2.37306	9.53179	3.13073	19.4983	6.42885	30.8184	24.3204	130.552	5.16337	22.6053	1.92584	2.72222
52	7916	1005.9	39400.1	323158	105.206	1797.11	7837.12	3759.69	0	1439.48	119.463	103.446	521.094	7021.45	2.61874	43.5947	392.954	6.42056	0.61516	9.12377	4.8229	39.5922	0	63.5818	26.7584	249.88	6.86138	14.9559	1.72179	0
51	7295.63	3841.83	42802.2	352789	164.576	2004.5	10485.8	0	328.14	1740.32	64.9811	112.414	334.022	6014.08	2.96235	14.0628	18.741	0	0.34634	10.3585	6.03936	61.2461	3.07798	74.209	25.683	318.917	7.5931	6.48984	1.76107	0
50	7470.53	3035.73	19673.2	348029	146.872	2037.35	1468.01	3058.89	263.106	752.308	125.567	108.6	359.764	8222.19	9.31395	37.3394	348.888	7.5937	0.93241	8.50102	3.77196	27.2643	0	79.7696	24.7308	171.344	5.07749	39.2729	1.97147	2.3513
49	8700.71	0	23305.5	281563	40.6419	5367.63	2114.81	6500.34	0	952.626	93.3866	86.2259	300.022	7933.19	4.78892	24.193	105.787	0	0.33721	10.0747	4.34998	33.2325	8.84583	177.936	22.9448	147.875	6.88181	30.5259	1.83973	1.85447
48	6920.62	4687.16	21035.4	356718	229.311	1997.34	1892.69	10776.6	0	731.186	168.223	124.987	359.019	7362.87	3.38218	18.4279	86.4914	0	0.27817	9.63459	3.55254	21.8015	2.81437	72.9878	23.4176	137.621	5.68293	25.8831	1.60138	3.18479
47	7168.12	2892.35	30320.1	342176	198.512	4072.05	6680.01	6386.88	0	1135.27	130.782	118.685	335.509	7271.42	3.68366	22.8279	68.3599	0	0.68961	9.35318	4.46726	32.1123	0	83.5908	23.8471	247.97	6.58791	13.1453	1.63023	2.86335
46	7284.29	2136.33	35136.3	329106	207.735	3157.36	6554.26	9328.96	0	926.493	136.384	120.662	352.956	10190	2.86232	25.4604	196.187	7.91016	1.03259	9.26115	4.02397	26.4787	3.1168	70.5807	24.3144	186.211	6.72559	15.0164	1.6512	1.4037
45	7329.92	4842.67	36852.2	363387	289.874	3000.8	5391.48	381.547	0	751.397	184.467	92.2142	840.062	7996.51	3.453	15.0261	12.0726	0	0.33205	12.0157	6.18454	63.9413	10.8119	440.466	25.0663	268.968	8.23004	3.65184	1.79188	2.68932
44	7880.85	143.844	39105.6	316980	65.2533	2054.02	8551.88	0	0	1682.51	94.1342	104.351	339.064	9029.51	5.84493	16.4803	25.0651	0	2.15258	11.4005	7.07208	73.2574	10.8825	268.887	23.4968	325.136	9.18148	3.21293	1.75123	1.68345
43	6110.62	5020.93	23552.9	366992	308.153	1958.95	6804.08	0	0	2253.95	105.603	121.98	373.118	10506.4	4.89279	66.5723	705.153	40.7811	6.19853	13.4716	5.81008	55.1401	12.1859	174.935	25.8141	403.162	8.34175	0	1.67733	0
42	7063.27	3525.74	45801.1	351159	177.611	1878.61	7675.16	0	0	1694.04	131.292	128.719	350.544	6490.04	3.47826	30.6639	134.45	4.81671	1.13785	10.6795	4.68124	38.9357	12.0991	93.1843	22.7445	291.965	7.32029	12.9061	1.76292	0
41	8150.32	0	39797.6	307067	97.8853	3301.06	7705.64	0	0	1795.91	80.7036	105.381	293.682	9516.57	4.00825	17.0049	29.465	0	1.06598	11.1215	5.77497	58.7657	11.6252	386.586	22.1989	199.5	7.46139	7.60587	1.71501	2.37168
40	7449.11	2685.61	41389.5	341760	164.914	1905.29	7870.28	2140.14	289.531	1428.98	109.542	116.522	336.915	14098.7	4.75162	27.2292	164.411	17.8558	1.67981	10.7898	4.85099	37.6686	0	96.8997	30.138	205.223	7.39452	18.6388	1.73206	3.32209
39	7658.3	3944.84	35525.8	355930	300.756	1955.02	7209.72	0	0	1876.46	104.198	126.424	336.448	17065.8	5.38509	26.8164	169.154	17.38	3.38048	13.4632	5.25803	48.5302	11.9088	533.486	24.8726	266.484	7.54621	2.66024	1.90035	0
38	10241.1	0	38818.8	239579	0	3255.03	5436.48	0	0	1763.61	39.6582	70.4229	267.096	7226.38	3.28982	14.2617	26.648	0	5.57602	15.2577	5.20229	45.3074	9.08103	116.698	29.5727	274.424	8.16328	16.8642	1.81603	3.28312
37	8789.7	0	47336.2	267951	0	2052.82	8057.94	595.85	0	1612.24	86.6819	91.9501	311.563	6107.25	2.13682	20.9221	33.1417	0	0.66279	9.32384	5.49398	45.3945	5.68078	281.762	30.3538	313.62	9.16287	7.93617	1.69031	0
36	8525.12	771.114	37000.9	320045	165.63	3447.48	6063.11	1363.95	0	1785.4	74.8359	124.709	309.566	5228.26	2.63905	22.9812	119.35	0	1.40855	12.0138	5.14541	43.0041	10.5589	497.968	22.8007	279.186	7.7896	8.64033	1.82198	1.48699
35	7342.48	196.707	28320	293902	197.816	2382.82	2643.38	29014.9	0	895.398	122.85	107.959	312.766	5453.86	2.75946	18.2007	79.9409	0	0.55545	8.32571	3.78284	28.0387	5.02954	269.147	24.2365	249.929	5.75848	9.96368	1.88047	8.78974
34	7715.61	2039.25	35538.8	334500	247.352	4229.96	3839.28	1238.15	0	1622.93	97.3317	107.547	327.23	6870.53	3.86028	42.8056	295.185	11.4482	4.58118	14.75	4.32513	31.3853	5.8063	496.828	26.8031	229.215	6.7732	8.98508	1.82377	1.51213
33	7957.29	1429.62	36220	330341	134.902	1807.18	4835.8	254.485	0	2180.25	84.2119	106.476	340.892	7001.14	3.31896	31.2073	217.578	1.46466	1.12529	10.8292	4.46048	32.6219	5.5517	371.622	25.1045	265.07	7.12382	12.5641	1.68183	0.24482
32	9047.83	0	27480.4	305597	27.8843	1897.74	3064.51	0	0	1765.35	67.5138	94.1431	313.354	5058.39	2.57537	19.7129	91.1052	0	0.29801	10.4899	3.79105	26.3161	11.2391	72.4122	23.4292	249.879	6.51622	18.4928	1.73323	2.78937
31	8021.25	1994.29	38412.7	334473	100.637	2962.57	4298.79	0	731.905	1295.06	38.1108	125.374	326.084	6470.85	2.5123	20.1236	74.3375	0	0.49272	10.1488	4.11392	31.8801	5.94918	117.028	22.9234	265.16	6.12667	12.3276	1.80878	0
30	8533.03	0	35510.3	281530	83.5246	4690.61	4086.79	10090.8	0	866.329	128.793	126.574	300.178	8286.68	3.02997	38.3122	416.797	9.79693	0.58407	9.51564	2.95915	9.85895	2.04727	74.0013	22.1221	140.227	5.40669	27.543	1.70502	4.8759
29	7670.66	1882.45	19218.8	330181	166.097	2140.38	410.578	15170.5	0	434.114	152.556	123.539	326.772	6602.49	7.34432	25.5855	199.824	4.40995	0.93695	8.9391	3.12212	15.3881	4.78136	80.9504	25.6286	136.887	5.89047	36.0978	1.62601	6.09738
28	9203.68	0	15976.9	307128	69.145	2154.42	0	6749.96	0	541.296	152.738	94.3857	294.899	6965.46	3.12272	130.483	1301.41	50.3286	0.80772	9.36906	2.97411	9.84177	1.24619	76.8109	24.8632	236.59	5.69106	16.165	1.44729	7.71275
27	9507.79	0	27657.1	274578	0	1775.48	416.345	5032.57	0	859.104	147.908	98.4513	306.49	8571.95	3.04033	54.5536	478.491	15.6253	0.60459	11.0596	3.01475	12.9228	3.46957	65.2247	28.3186	275.008	6.11095	17.2832	1.6631	0
26	6957.42	1383.97	40363.9	314896	232.168	1921.22	872.249	15444.1	1873.22	1685.32	11.569	88.4423	355.167	8073.69	11.3142	106.147	1333.28	53.6068	1.01449	8.88127	2.59672	7.58392	3.91631	47.2441	28.2733	497.352	5.64341	18.3137	1.79522	0
25	8472.81	0	53453.4	291606	102.542	1781.06	13200.8	565.295	0	3163.18	48.0243	94.1349	282.998	6708.46	2.75745	30.1595	130.63	0	0.78183	10.9883	4.51538	31.6206	5.95299	197.807	32.9601	160.687	8.5571	22.0131	1.54493	2.80386
24	8416.29	910.429	9205.83	330473	62.5451	2132.59	0	2970.84	0	151.622	273.414	72.2787	336.298	5826.36	3.75348	55.9473	625.117	15.0825	0.45801	9.71652	2.31512	2.13812	5.71248	82.2414	25.6846	113.326	5.46068	26.0972	1.4536	8.56286
23	8376.73	0	14983.8	284348	128.255	1942.65	0	37807.7	0	110.125	145.614	97.1253	290.764	7970.34	7.51111	178.371	2272.51	99.8139	0.96523	11.545	2.89226	11.1248	11.3418	80.6735	23.5837	58.3219	6.17181	32.4897	1.50564	13.0307
22	8646.67	0	29890.2	244930	46.3069	1998.5	0	28956.2	0	333.823	167.839	105.403	374.177	14478.3	6.01079	79.8491	1040.3	47.6002	1.46533	10.0689	2.77293	8.23344	6.85941	102.695	20.6219	55.7221	5.35999	30.3681	1.43842	9.04747
21	7123.79	5186.86	8539.09	361340	352.012	2175.94	0	11426.2	0	256.268	243.408	114.71	412.839	5261.25	4.2846	108.291	1215.38	44.4928	0.50659	10.1646	2.5025	5.6838	6.39875	241.617	22.4494	102.03	5.18576	24.1075	1.49472	5.88946
20	6884.78	4218.82	10106.8	352137	262.282	1924.11	0	13316.7	0	183.909	275.553	109.746	471.088	11531.3	7.14412	162.857	2057.24	84.0861	1.62256	11.3281	2.78768	8.53538	9.98895	370.921	18.3365	64.9118	5.27289	29.9524	1.62018	16.427
19	7574.17	3322.73	12772.2	342854	289.78	2464.51	0	15569.4	0	330.404	309.201	97.164	377.251	6827.78	4.11604	127.568	1604.13	64.9468	0.91455	9.36408	2.45812	4.22924	0.57187	202.653	21.8318	59.6835	4.51388	26.4732	1.50067	9.29305
18	8522.59	0	53500.9	292942	112.847	2208.75	15740.7	0	0	2634.4	79.8898	105.012	251.43	13084.3	4.43664	15.0643	46.5001	8.49485	33.538	21.7623	9.63042	111.103	13.6825	331.373	19.5315	360.668	10.086	0	1.8214	4.67315
17	7597.55	3429.92	37106.9	351301	200.979	2170.49	6352.17	0	0	1884.26	103.944	106.242	323.708	5801.35	2.87411	15.5059	19.0338	0	0.53	10.1385	5.45385	52.7626	11.2167	377.753	26.1852	385.107	8.00366	0	1.6926	4.43564
16	9035.24	0	12824.6	321993	238.022	1659.59	0	0	0	865.158	199.025	91.9119	338.152	4374.14	2.78604	24.5733	167.05	0	0.49462	10.6052	3.37741	14.3779	20.2735	1291.24	15.0908	217.793	6.83451	3.84931	2.07409	5.33788
15	6479.51	5330.83	8967.09	363409	1384.46	1944.63	0	9507.92	0	473.996	146.229	142.101	367.787	3730.03	2.79672	25.5849	164.197	0	0.3808	10.0666	2.75456	9.27101	27.563	1822.25	17.4026	71.3326	6.67475	0	2.00377	3.02512
14	6553.62	6500.24	6251.71	372067	499.047	2211.76	0	9346.14	0	579.806	198.69	114.799	414.475	4368.51	3.3887	29.4922	170.063	0	0.33315	9.79661	2.69471	7.07398	11.4059	767.075	21.5927	243.128	5.90444	5.29737	1.70782	1.80012
13	8622.12	435.255	13020.4	316488	157.665	1598.87	0	16187.1	0	199.923	197.808	83.5123	326.728	6019.06	2.57115	26.5675	169.915	0	0.51268	9.70229	2.50774	5.02009	0.10631	460.534	22.738	83.4846	4.56898	18.5557	1.73357	3.97626
12	9016.63	0	11174	276602	21.7077	4159.84	0	10884	0	336.249	147.869	71.4481	368.378	4587.63	1.22156	21.7788	159.615	0	1.08993	7.51271	2.43073	8.90583	6.53267	93.8783	23.2333	61.2678	4.82156	35.9003	1.54394	0.16175
11	7086.64	4932.8	6381.28	358510	329.896	5111.92	0	11931.9	0	5.30714	264.462	92.0181	379.749	4527.76	3.25326	32.3685	301.027	0.32494	1.08995	7.84347	2.40025	2.7264	0	102.52	21.096	48.0902	4.57619	32.6096	1.50898	0
10	9743.76	0	12583.5	244502	6.93812	5840.65	0	6285.27	0	355.097	103.818	99.35	301.202	3431.48	1.05008	7.3475	9.21545	0	0.94303	7.49057	2.39407	2.53911	4.51675	120.557	18.4575	36.6742	4.68549	39.1474	1.77272	0.32037
9	9062.13	0	13038.1	310989	76.748	1986.71	0	11033.6	0	0	272.191	108.306	373.595	7289.49	3.17263	72.2082	782.738	26.5999	0.76034	9.17621	2.43215	0	0	194.081	22.7024	44.166	5.18164	31.7416	1.59642	4.16333
8	7789.83	3967.8	15354.5	354316	201.149	5641.95	0	5266.3	0	335.785	158.893	129.69	325.552	4030.41	2.99017	14.8055	42.8267	0	0.00368	10.6768	2.69492	7.71524	3.12892	139.871	21.3962	110.371	4.92155	22.7351	1.61827	0
7	8156.62	3894.37	9853.2	357201	131.04	1974.1	0	1708.46	0	119.136	156.24	119.846	311.238	3789.06	3.07197	17.9088	136.598	0	0.32777	8.60887	2.42435	3.82974	0	122.351	23.0772	125.569	4.52324	25.3977	1.62327	4.42629
6	6828.23	6803.1	8723.17	374448	286.086	3386.59	0	6798.03	0	167.629	262.52	111.315	454.81	3676.22	3.20033	36.8651	337.754	2.93217	0.25883	10.3969	2.63724	0.17597	0	325.557	21.9779	72.6021	5.17805	24.0209	1.44832	6.47674
5	7277.02	5646.89	6114.38	367730	220.33	2218	0	5616.2	0	89.4536	203.375	111.875	389.958	3188.61	3.06653	14.8356	46.6835	0	0.45302	8.91227	2.49748	5.67407	8.1332	109.678	21.092	104.066	5.29675	23.1807	1.66324	0
4	7975.66	3346.94	10962.3	350106	203.469	2136.11	0	6061.96	0	203.953	174.281	124.086	378.028	4897.62	4.31193	70.7698	754.287	23.2313	0.85821	10.4555	2.63197	6.27097	3.13097	162.456	24.3852	67.0586	5.30582	30.1387	1.35258	7.08727
3	7230.48	6270.23	5830.69	375409	204.724	2356.99	0	1597.78	0	213.179	205.056	84.6925	343.465	2933.54	3.45499	71.2644	835.599	20.4971	0.77263	8.17626	2.38941	2.7986	3.15851	36.1571	21.1093	80.7652	4.79892	31.147	1.5749	1.11064
2	8784.08	0	23016.8	299535	119.85	1844.52	0	284.266	0	374.837	219.735	20.6692	1599.68	8674.99	2.17682	70.411	809.397	44.5859	3.31842	12.9775	2.70311	8.92992	10.7881	263.017	23.2008	50.8877	5.60149	32.2222	1.56172	10.8886
1	9035.02	0	21546.3	277030	123.257	1660.62	180.894	0	0	885.723	125.744	41.5285	663.767	13064.8	4.47079	89.424	916.301	50.2965	28.1058	22.3347	3.55617	15.8008	15.535	954.543	25.1959	85.6778	6.87203	12.3475	1.72491	9.66065
0	9098.55	1480.06	5485.13	338473	53.1596	2209.56	0	0	0	0	160.728	129.283	328.69	4414.86	2.33242	22.3952	179.304	3.49253	4.74573	15.4809	2.65574	6.02788	5.93768	77.46	22.1578	56.1	5.11422	34.7226	1.50325	1.75516

Figure 15. Compiled major and trace element data (in ppm) of the 30 elements measured in this study ordered stratigraphically from the base (0 ft) to the top (73 ft) of the section.

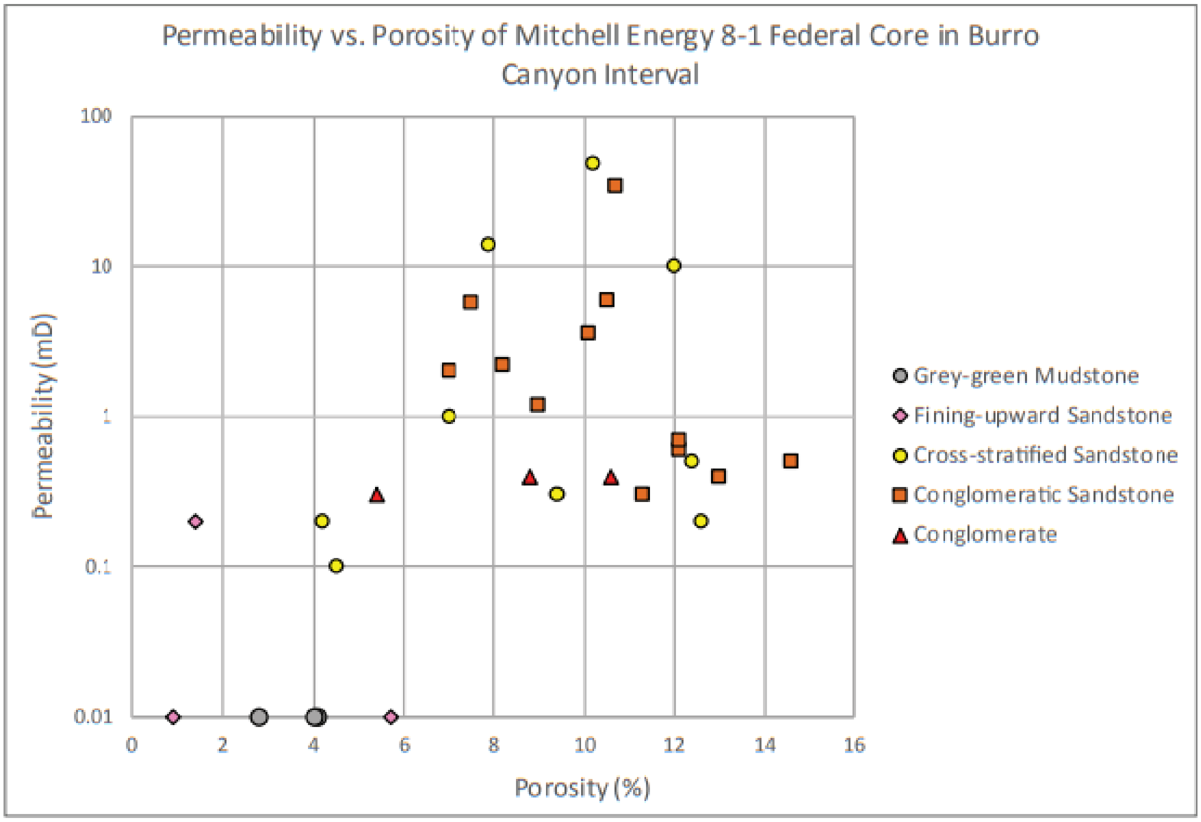

Figure 16. Permeability and porosity cross-plot of the Mitchell Energy 8-1 Federal core data for the Burro Canyon Formation colored by facies. From Clark (2018).